Modelling of Folded Graphene and Related Systems

Michael Gauci

Supervised by Prof. Joseph N. Grima

Co-supervised by Dr Daphne Attard

Metamaterials Unit

Faculty of Science

University of Malta

March, 2022

A dissertation submitted in partial fulfilment of the requirements for the degree of Master of Science in Metamaterials

Acknowledgements

I acknowledge the support of the University of Malta for making available the computational resources used in this work. Some of these resources were acquired through the project A-ROW, grant No. R&I-2017-033-T, financed by the Malta Council for Science & Technology through FUSION: The R&I Technology Development Programme 2018.

I would also like to thank the various individuals who supported me in this journey. First, I would like to thank my supervisor, Prof. Joseph N. Grima, for his continued support throughout the time spent working on this dissertation. His genuine belief in my capabilities as a research scientist and his insistence on resuming my studies after having taken a one-year suspension greatly contributed towards the completion of this work. In my view (which I believe is also shared by many of his past and present students), Prof. Grima is more than just a supervisor; he is a caring and honest friend in whom you can seek advice, even if at times the uncomfortable truth may be unpleasant to hear. His general tendency to push people out of their comfort zone has inadvertently led me to discover and delve deeper into the world of Linux and free and open-source (FOSS) software, to the extent that I now write and publish code in my spare time. For this, I will be forever grateful.

I also wish to express my gratitude towards members of the Metamaterials Unit, in particular my co-supervisor, Dr Daphne Attard, and Prof. Ruben Gatt. Dr Attard assisted me in reviewing the manuscript for any syntactic and semantic errors, whereas Prof. Ruben Gatt was kind enough to provide me with some recommendations on how I could enhance the quality of the literature review.

Finally, I would like to thank my family for their moral support during these past few years, but especially in recent months. I consider myself to be fortunate enough to have them by my side and willing to support me in whatever venture

I decide to embark on. Although at times it felt arduous to write this dissertation, particularly in the midst of a worldwide pandemic, the recurring thought of them seeing me graduate kept me going forward. Thank you once again for always being there for me.

Abstract

Graphene, a quasi-planar monolayer of sp^2-bonded carbon atoms known for its exceptional physical properties, is highly amenable to out-of-plane deformation. Recent studies have revealed that the creation of folded, pleated-like domains imparts novel characteristics to this material whilst permitting some of its existing properties to be effectively controlled through straining action via regulation of the emergent folding parameters. Despite the considerable influence that strain can have on the material properties of folded graphene, the literature pertaining to the nano-mechanical unfolding of folded, graphene-type systems remains scarce. In this work, molecular dynamics simulations were performed on three novel forms of folded graphene using an *ad hoc* protocol executable within LAMMPS to study their mechanical response to uniaxial tensile deformation. Patterned line defects were shown to constrain multiply folded graphene to a quasi-periodic, highly ordered morphology that gave rise to instances of pronounced negative tangent modulus – coincidentally with each fold opening – upon the application of uniaxial stress. The severe lack of periodicity observed in the corresponding profiles of the pristine folded systems was attributed to the absence of defect lines which permitted folds to be more mobile and at times merge, effectively reducing the frequency of fold openings. These structural differences were explained, for the first time, via a macroscale model based on the mechanics of paper folding. Overall, this study attests to the potential for defect-type fold lines to guide the unfolding process of folded graphene, and provides valuable insight into the different mechanisms involved in the unfolding of specific forms of folded graphene.

Contents

List of Figures

List of Tables

1

Introduction

Graphene[1] is a two-dimensional, sheet-like nanocarbon that rose to prominence in 2004 when researchers at the University of Manchester successfully isolated it from bulk graphite (Novoselov *et al.*, 2004), confirming prior theoretical work[2] which had alluded to its existence (Van Lier *et al.*, 2000). Later studies reported the remarkable physical characteristics of this material in its pristine form: a Young's modulus of *c.* 1 TPa for the suspended monolayer (Lee *et al.*, 2008), a measurably high thermal conductivity in the range $4400\,\mathrm{WmK^{-1}}$ to $5800\,\mathrm{WmK^{-1}}$ at room temperature (Balandin *et al.*, 2008), a carrier mobility that could reach $200{,}000\,\mathrm{cm^2\,V^{-1}\,s^{-1}}$ under ambient conditions (Morozov *et al.*, 2008), and the ability to absorb light over a broad spectral range (Zhao *et al.*, 2013). Such a unique and extraordinary combination of properties makes graphene a very promising next-generation material for a host of application fields which include energy storage (Olabi *et al.*, 2021), composite reinforcement (Zhao *et al.*, 2020), filtration technology (Anand *et al.*, 2018) and optoelectronics (Bonaccorso *et al.*, 2010).

Conceptually, the stratification of graphenic layers may be regarded as a spectrum, with graphene and graphite at opposite ends of it. According to this paradigm, the modality with which electrostatic interactions are formed in these layered structures is the governing factor in the gradual transformation of the properties intrinsic to graphene into those commonly associated with

[1] The term "graphene" was formally introduced to the scientific community in 1986 through a *Carbon* editorial which argued that 'it [was] not correct ... to speak of "graphite layers" when meaning single two-dimensional carbon sheets. Even the terms "carbon layer" or "carbon sheet" are not unambiguous' (Boehm *et al.*, 1986).

[2] The first theoretical investigation of what we now refer to as "graphene" is attributed to the post-WWII work by P.R. Wallace from the National Research Council of Canada who examined the 'zone structure of a single hexagonal layer' (Wallace, 1947).

graphite. Complimentary to it is the notion of graphene as being a template for the creation of more complex carbon nanobodies whose material properties are defined by those same electrostatic interactions between the (non-)contiguous graphene portions (Figure 1.1). Materials within this spectrum, such as bilayer graphene, few-layer graphene, and folded graphene, have been gaining more attention recently due to their fascinating characteristics which in some aspects even exceed those of graphene.

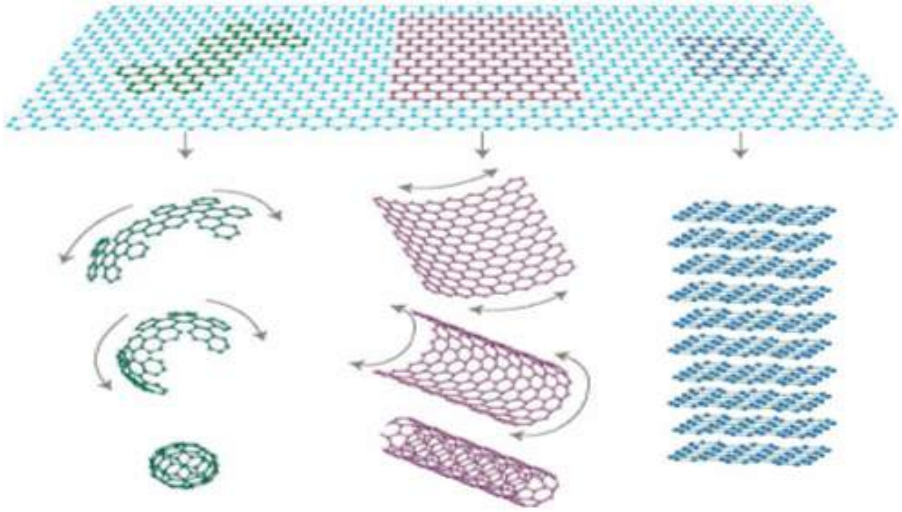

Figure 1.1: Carbon nanobodies may be regarded as assemblies of (non-)contiguous graphene domains. For instance, the warping of a graphene fragment about a common geometric centre produces a 0-D buckyball, a rolled-up graphene monolayer becomes a 1-D nanotube, and stacked sheets are akin to graphite. Reproduced from Geim and Novoselov (2010).

The spectrum paradigm leads to an important realisation – that certain characteristics in graphene can be effectively modulated by careful adjustments to the interlayer interactions. For instance, it is known that small variations to the relative orientation of graphenic layers have a profound effect on the electronic properties of graphene-type systems. In 2011, Bistritzer and MacDonald (2011) posited that rotational misalignment in bilayer graphene creates an angle-dependent Moiré pattern (Figure 1.2) which could facilitate inter-sheet tunnelling between the two graphenic layers. According to their calculations, the tunnelling energy barrier would disappear altogether at 1.1° and with

progressively wider twist angles, the sheet electrons would slow down while becoming strongly correlated with each other. These predictions were later verified experimentally by Cao and co-workers, confirming the low-temperature superconductivity (Cao *et al.*, 2018b) and the formation of Mott-like insulator states in twisted bilayer graphene (Cao *et al.*, 2018a) (Figure 1.3).

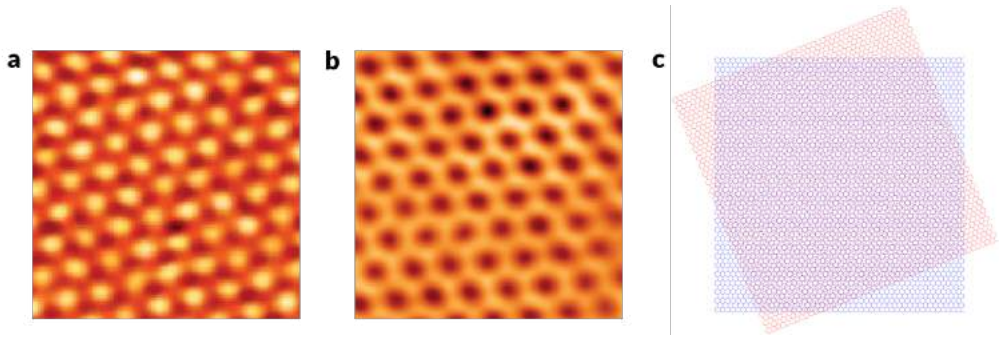

Figure 1.2: Atomically resolved STM images of **(a)** bilayer graphene and **(b)** a twisted bilayer region, as reported by Xu *et al.* (2016). **(c)** A digital rendering of bilayer graphene with a Moiré pattern that corresponds to a twist angle of 22°.

The appearance of ripples in suspended graphene (Bangert *et al.*, 2009) reflects the receptivity of the monolayer towards out-of-plane deformation (Figure 1.4). This critical aspect of graphene that, unfortunately, is not given enough attention in mainstream scientific textbooks, presents an opportunity for researchers to introduce layering within an uninterrupted graphene sheet along with the possibility, as described in Chapter 2, to modify or extend its features by regulating the emergent folding parameters through straining action.

Before proceeding any further, it must be emphasised that, at present, there is no standard naming convention to classify folded graphenes, despite the fact that several characteristics displayed by this diverse class of conformations folded graphenes are inherently different from standard graphene. Unfortunately, this raises the possibility for important findings made in relation to folded graphenes to be practically lost to improper indexing in the voluminous literature that is published on graphene. It is envisioned that such a formal classification system would differentiate between the many possible forms of folded graphenes

primarily on the basis of the number of folds present, but also according to distinctive structural features such as the folding angle, fold spacing, and the folding amplitudes. However, for the purposes of this dissertation, the term *'folded graphenes' shall be limited to a group of graphene morphologies containing one or more folding domains*, i.e. one or more folding lines extending across both sides of the monolayer.

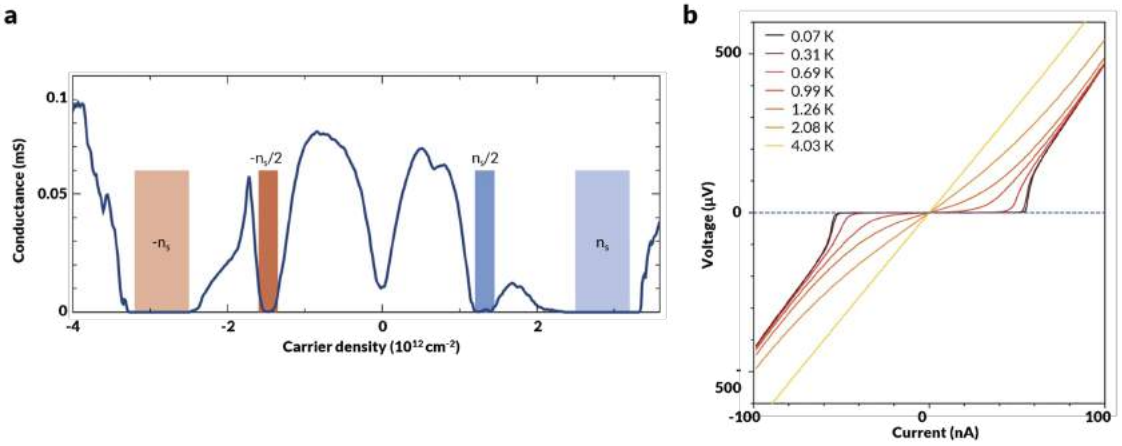

Figure 1.3: Anomalous behaviour in bilayer graphene with rotational mismatch. **(a)** Conductance as a function of carrier density for bilayer graphene with a twist angle of 1.08° and at an operating temperature of 0.3 K, as reported by Cao *et al.* (2018a). Insulating states were observed at *(i)* hybridization-induced bandgaps above and below the lowest-energy superlattice bands when the carrier density was $\pm 2.7 \times 10^{12}$ cm^{-2} (lighter regions) and *(ii)* half-filling states, as a result of Moiré-induced electron localisation (darker regions). **(b)** Current-voltage curves for bilayer graphene with a twist angle of 1.05° at different temperatures, as reported by Cao *et al.* (2018b). Most notably, at the lowest studied temperature of 70 mK, the critical current was measured to be approximately 50 nA.

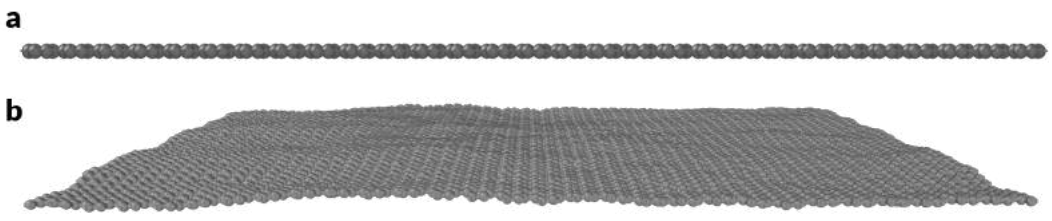

Figure 1.4: **(a)** A side view of 'flat' (incorrect) graphene as sometimes perceived and depicted in mainstream scientific textbooks. **(b)** A more realistic representation of graphene showing the spontaneous ripple formation which is responsible for significant shrinkage in both dimensions of the sheet (relative to the idealised planar conformation).

Despite the intriguing aspects of folded graphenes, one of them being the strain-sensitive nature of some of its properties, there are very few published reports that examine the unfolding behaviour of such systems. In an attempt to address this sparsely studied aspect, the present dissertation investigates, through the use of molecular dynamic simulations, the structural and mechanical response of some folded graphenic conformations during uniaxial deformation, along with a qualitative description of the deformation mechanisms involved. In particular, **Chapter 2** presents important literature pertaining to graphene, with a focus on certain feature enhancements that are observed in folded graphenes relative to the planar form of the allotrope, and selected strategies towards fold creation.

Chapter 3 describes the LAMMPS protocol that was developed specifically for simulating the uniaxial stretching of graphene-type systems, and the validation of this protocol against pristine, unfolded graphene.

Chapter 4 provides an account of the process that was undertaken to construct a series of novel folded graphenes and the slight changes that were made to the protocol developed in Chapter 3 to simulate their structural and mechanical properties during uniaxial loading. The main findings of this work are presented along with a discussion of its significance, strengths and limitations.

Finally, **Chapter 5** presents a summary of the conclusions reached and discusses briefly how this work can be further extended in future studies.

2

Literature Review

Chapter Highlights

This chapter reviews important literature pertaining to the subject matter of this dissertation i.e. folded graphene, through a discussion of:

- Carbon, more specifically how it manages to exist in a wide variety of allotropes, and the journey that led to the discovery and characterisation of graphene;
- The emergence of folded graphene, from the observation of unintentional wrinkling during the synthesis of graphene to a distinct form of the nanomaterial with its own set of characteristics;
- Techniques which are designed to introduce folds within a graphene sheet;
- The properties and characteristics of folded graphene and its added versatility when compared to standard graphene;
- Currently available literature on the unfolding process of folded graphene.

2.1 | Introduction

Carbon, being a key element associated with life on Earth, possesses a rather unique ability which helps explain its ubiquitous presence in the natural world: catenation. The ability of carbon to form covalent bonds with other elements extends to forming similar bonds with itself, giving rise to a plethora of compounds that are commonly referred to as "organic" compounds due to their traditional natural provenance.

A corollary to catenation is the diverse family of carbon allotropes which exists in the nanoscale (Khalaj *et al.*, 2017) along with the potential for novel ones to be created (Zhang and Jiang, 2019). The extensive allotropy of carbon largely derives from the favourable energetics of C–C bond formation and its propensity to assume various hybridisations which result in very distinct geometries and properties. Orbital hybridisation, or the mathematical mixing of atomic orbitals, conceptualises the types of covalent bonds that are accessible to carbon, namely single (sp^3), double (sp^2), and triple (sp) bonds. Until recently, the only known allotropes of carbon were diamond (sp^3-hybridised) and graphite (sp^2-hybridised). The surprising discovery of fullerenes in 1985 (Kroto *et al.*, 1985), and carbon nanotubes six years later (Iijima, 1991), galvanised research into other possible forms of carbon.

Allotropes of carbon, while sharing some common features, possess characteristics that make them distinct from one other and better suited to specific applications. For instance, graphite, known for its good conductivity, has demonstrated optimal performance as an anode material in Li-ion batteries due to its exceptional Li intercalation (Goodenough, 2013), whilst the robustness of diamond makes it the preferred material of choice for the tip of atomic force microscopy (AFM) cantilevers (Fang *et al.*, 2008; Fujisawa *et al.*, 2009; Ruffell *et al.*, 2011). In recent years, focus has shifted specifically onto 2D carbon-based materials and their derivatives, which led to the discovery and characterisation of a whole new array of nanostructures (Figure 2.1). As a result, the need arose for this growing family of two-dimensional carbon systems to be described by its own nomenclature (Bianco *et al.*, 2013).

Although the term “graphene” was first proposed by Boehm and co-workers in 1986 to describe a 2D system of sp^2-hybridised carbon atoms arranged in a honeycomb lattice (Boehm *et al.*, 1986), theoretical work on the potential properties exhibited by graphene can be traced back as early as 1947 (Slonczewski and Weiss, 1958; Wallace, 1947). In the 1970s and 80s, it was posited that the intercalation of graphite crystals with suitable chemical species

could lead to the decoupling of the graphite layers (Dresselhaus and Dresselhaus, 1981). At that time, however, it was still widely assumed that the low dimensionality of the material would prevent it from achieving the required stability to exist in the free state. Landau and Peierls had argued that any thermal fluctuations in the crystal lattice of flat, 2D systems would result in atom displacements comparable to interatomic distances, thereby causing their rupture (Landau, 1936; Peierls, 1935). The Merwin-Wegner theorem extended this argument by postulating that in order for crystalline systems like graphene to exist, they must adopt a rippled structure (Mermin, 1968). Consequently, research on this topic was perceived to be of minimal practical value and relegated to a mere academic endeavour.

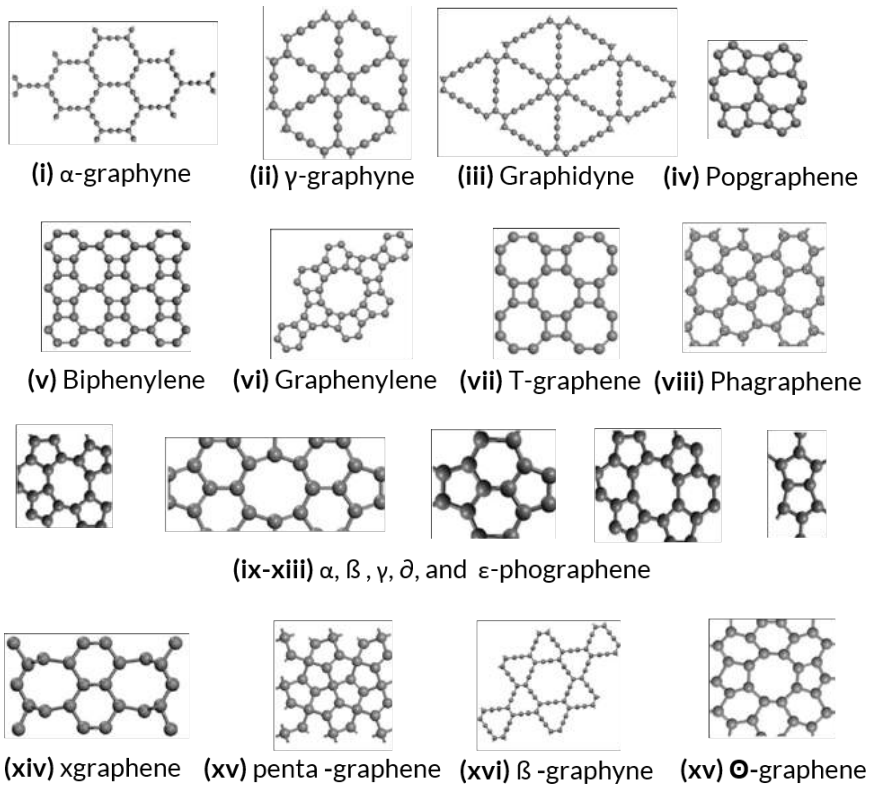

Figure 2.1: A selection of theoretical 2D carbon allotropes of which, currently, only **(i-iii)** are known to have been synthesised. Adapted from Rajkamal and Thapa (2019).

The chemical exfoliation route envisioned by Dresselhaus and Dresselhaus (1981) was later revisited by Shioyama (2001) whose work constituted one of the

initial attempts at isolating graphene from bulk graphite. Even though this approach failed to produce planar graphene when the intercalating species was removed, which instead ended up scrolled (Viculis *et al.*, 2003) or restacked (Horiuchi *et al.*, 2004), it is worth mentioning that the chemical exfoliation route has the potential to create novel materials composed of isolated graphene layers embedded within a three-dimensional matrix. Conclusive isolation of the monolayer came in 2004 by the mechanical exfoliation of graphite flakes using adhesive tape (a technique popularly known as the "Scotch tape method") and the transfer of the micrometer-sized graphene fragments so formed onto an oxidised silicon substrate for characterisation of its electronic properties (Novoselov *et al.*, 2004). Geim and Novoselov were later conferred the Nobel Prize in Physics for this breakthrough, as well as for reporting about the unusual quantum Hall effect that manifests itself in graphene (Novoselov *et al.*, 2005).

The existence of a freely suspended graphene sheet under normal temperature and pressure conditions does not diminish the theoretical arguments made against the stability of strictly flat systems of which, at times, graphene is mistakenly presented to be a member. In fact, as correctly predicted by the Merwin-Wegner theorem, graphene adopts a rippled configuration to achieve thermodynamic stability. Mechanistically, it is theorised that the interaction between acoustic phonons and the C–C bonding electrons, combined with the uneven density of the delocalised electrons, produces an asymmetric distribution of bond lengths which forces the lattice into a non-planar conformation to limit its total free energy (Fasolino *et al.*, 2007). Experimental observations of lattice fluctuations in suspended graphene using scanning tunnelling microscopy (STM) have shown that the ripple pattern is dynamic in nature, albeit with a periodic component (Bangert *et al.*, 2009; Xu *et al.*, 2014a). Moreover, observations of similar out-of-plane distortions have been reported in mechanically exfoliated graphene (Choi *et al.*, 2012), epitaxial graphene grown on SiC (Varchon *et al.*, 2008), and chemical vapour deposition (CVD) graphene

grown on Ru (Borca *et al.*, 2009) and Cu (Paronyan *et al.*, 2011) – a clear indication that such behaviour is independent of the synthetic pathway used.

The rapid increase in the number of graphene-related research over the previous decade (Ren *et al.*, 2018) may suggest that the commercial availability of graphene is imminent. However, a major obstacle to this achievement is the current unavailability of a cost-effective process by which large quantities of industrial-grade graphene can be produced. To this end, several methodologies have been proposed or tested in an effort to overcome the scalability issues associated with producing graphene via the mechanical exfoliation of graphite. One of the more promising synthetic pathways that could efficiently fabricate metre-sized films of this nanomaterial is CVD (Bae *et al.*, 2010). Researchers have been using this technique since the earliest days of graphene synthesis, albeit with some modifications to mitigate against the formation of wrinkles (Park *et al.*, 2018). These typically appear during the post-growth cooling stage of the CVD process when the newly formed graphene contracts less than its metal substrate, forcing areas within the sheet to detach from the substrate (Zhang *et al.*, 2011).

2.2 | The rise of folded graphene

It is not uncommon for the scientific community to ignore a published finding, or underestimate its impact within a field of research, only to cause a paradigm shift in that field some years later as more corroborating evidence emerges, or becomes an important milestone towards resolving a pressing issue in the most unexpected way. A prime example of this was the discovery by Sir Alexander Fleming of penicillin in 1928 and reported in the following year (Fleming, 1929). Prior to 1940 – when Chain *et al.* (1940) conducted the first animal testing of penicillin – producing such a drug in sufficient quantities to reliably assess its medical efficacy and limitations proved elusive, and so its therapeutic potential over the preceding decade went largely unnoticed. However, by 1943, through the work of Howard Florey, Ernst Chain and their colleagues at the Sir William

Dunn School of Pathology at Oxford University, the medical benefits of penicillin became widely acknowledged, thus heralding the era of modern antibiotics which contributed to a substantial reduction in the case fatality rate for patients with symptoms of bacterial infection.

Likewise, the beneficial aspects of graphene corrugation were, for the most part, overlooked by researchers in the early days of graphene synthesis. At the time, due attention was given to the phenomenon of wrinkling in CVD-grown graphene which consists in the formation of arbitrary shaped, folded structures that are randomly distributed along the monolayer sheet (Figure 2.2). The pertinent research revealed that both wrinkling and rippling interfered with the transport properties of graphene (Barnard and Snook, 2012; Katsnelson and Geim, 2008), which strengthened the notion of corrugation as a form of topological lattice defect that had to be mitigated against (Dean *et al.*, 2010; Lanza *et al.*, 2013; Lui *et al.*, 2009). This view, however, began to be challenged by the work of Guinea *et al.* (2008) who showed that corrugation in the form of periodic folds can induce novel electro-magnetic properties in graphene. Later work by Pereira and Neto (2009) corroborated these findings by demonstrating that, through folding, graphene can exhibit an effective, strain-induced gauge field. These studies in particular highlight a shift in perception towards corrugation within graphene as material scientists learned to distinguish between the often undesirable 'uncontrolled' wrinkling and 'controlled' folding that allows for the creation of various graphenic conformations (Figure 2.3), possibly with their own unique characteristics.

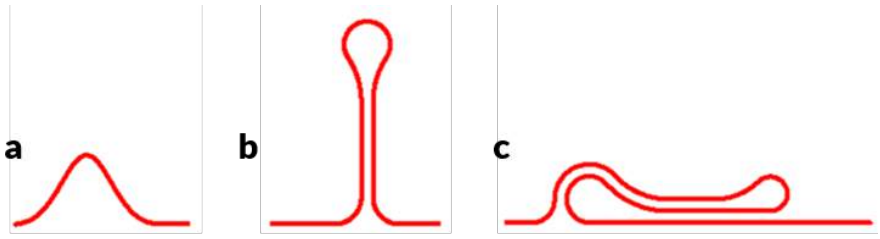

Figure 2.2: An illustration of folded graphene morphologies which commonly occur as artefacts in CVD graphene: **(a)** ripple; **(b)** standing wrinkle; **(c)** collapsed wrinkle. Reproduced from Zhu *et al.* (2012).

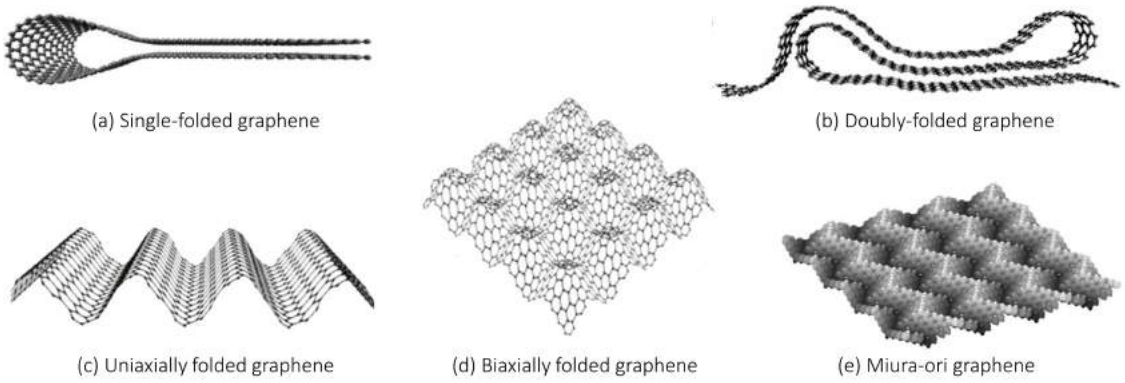

Figure 2.3: Folded graphene illustrated through a selection of representative examples. Adapted from (Ho *et al.*, 2020; Kang *et al.*, 2018; Kim *et al.*, 2011; Ning *et al.*, 2020).

Indeed, further research into folded graphenes revealed a number of exciting properties which cannot be exhibited by standard planar graphene. These range from purely mechanical characteristics, such as the manifestation of anomalous auxetic behaviour (Grima *et al.*, 2018; Lin *et al.*, 2021)), to ones which involve the electronic structure of the material, such as semiconducting character (Lee *et al.*, 2013). Furthermore, folding also enhances several of the reported characteristics in pristine unfolded graphene which augments its existing properties and range of potential applications. Some of these enhanced characteristics are discussed at length in Section 2.4.

2.3 | Selected methods for the production of folded graphene

Apart from the aforementioned theoretical developments made as a result of computational and mathematical models (Guinea *et al.*, 2009, 2008), there are also important reports in the literature detailing the advancements made by scientists to purposefully produce graphene in a manner where the nano-rippling was magnified and thus, *de facto*, result in the production of what is being referred to as folded graphene. These production methods include:

(a) **Bilayer annealing**

This approach exploits the inherent chemical reactivity of the boundary sheet atoms in graphene[1] to produce a folded edge between two stacked monolayers (Figure 2.4). The reactivity at the edge boundary varies according to the termination pattern, with the zigzag type being more reactive than armchair because of its ability to localise π electrons at the edge sites (Jiang *et al.*, 2007; Nakada *et al.*, 1996). Interestingly, in the absence of thermal activation – a prerequisite for bilayer annealing – suspended graphene was observed to self-fold at the boundary region to form a structure which, similar to an annealed fold, closely resembles one-half of a single-walled carbon nanotube (SWCNT) (Gass *et al.*, 2008; Meyer *et al.*, 2007).

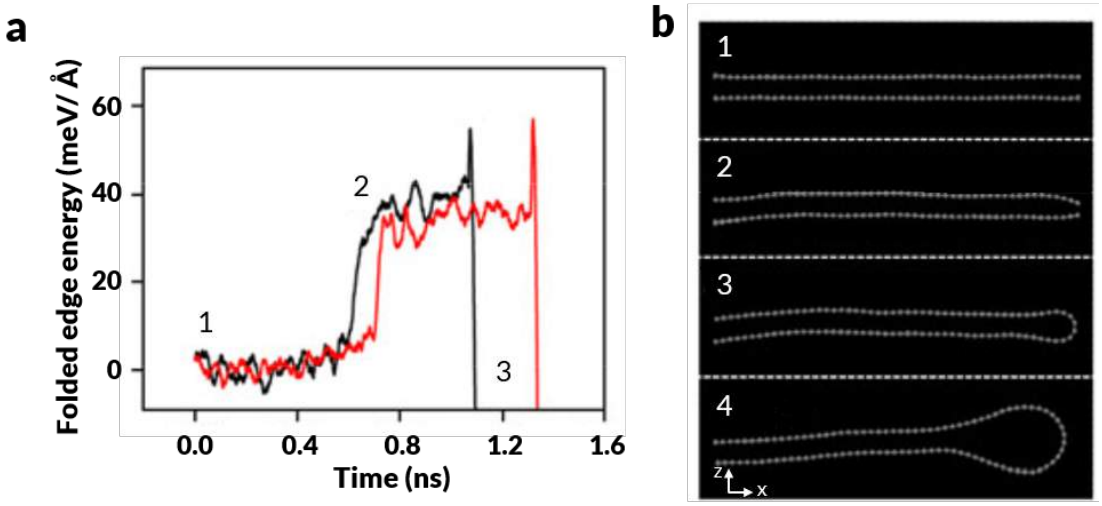

Figure 2.4: The thermal annealing process of bilayer graphene to form a folded edge, according to molecular dynamics simulations performed by Su *et al.* (2011). **(a)** The predicted energy diagram for the formation of a jointed edge between two graphene sheets with a noticeable drop in energy that corresponded to the exact moment when the sheets formed a closed edge. **(b)** Representative structures for the double-layered graphene at various stages during the edge formation process.

[1]Whilst the basal plane of graphene is relatively inert, the edge boundary regions contain atoms with dangling σ bonds.

(b) **Substrate effects**

As mentioned earlier, CVD graphene is characterised by unintentional folded structures which occur as a result of a discrepancy between the thermal expansion coefficient of the growth substrate and that of graphene itself. The substrate, however, is also capable of guiding graphene into pre-determined folded conformations by means of patterned etching on its surface, as illustrated in Figure 2.5.

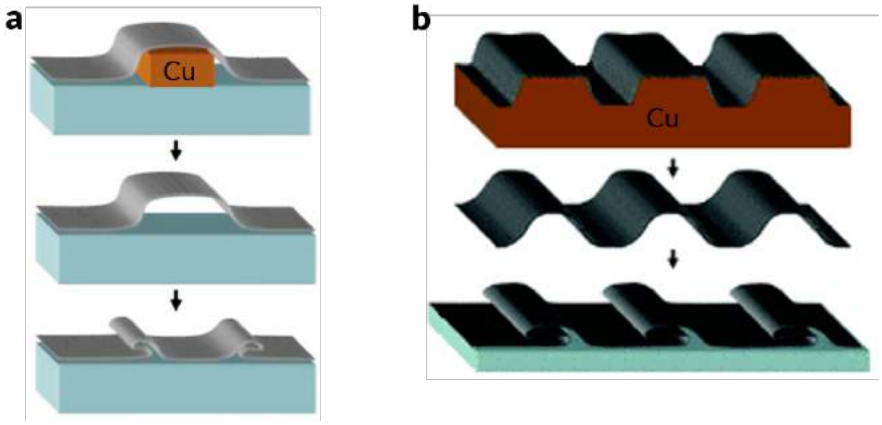

Figure 2.5: Schematic representations of two approaches developed by Kim *et al.* (2011) which lead to controlled fold formation in graphene. The patterned surface of the substrate shown in **(a)** may be imprinted as follows: A thin coat of poly-methyl methacrylate (PPMA) resist is deposited onto a copper substrate, then parallel lines are written on it using electron beam lithography. Afterwards, the metal substrate is partially etched using $Na_2S_2O_8$, followed by the removal of the remaining resist which reveals the etched line pattern. In **(b)**, controlled fold formation occurs after the growth process, when graphene is transferred onto a metal substrate having a patterned surface. The underetching of the metal removes support for selected parts of the graphene sheet, causing them to collapse into folded structures.

(c) **Mechanical perturbation**

This approach involves the application of ultra-sonication to activate fold formation in graphene suspended in solution (Figure 2.6). It should be noted that this technique is stochastic, in the sense that, although it produces folded graphene, other structures are created as well due to the randomness of the process involved.

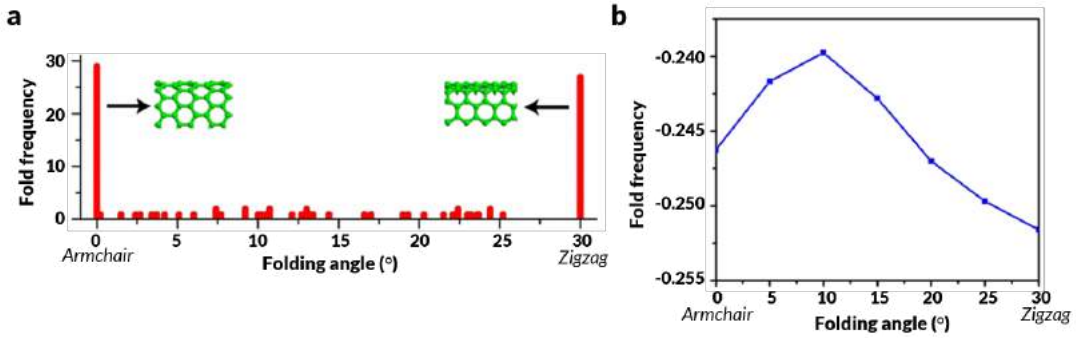

Figure 2.6: The directionality of fold formation in pristine graphene in relation to the thermodynamic stability of the folded structure. **(a)** The folding angle distribution of 100 graphene samples after being subjected to mechanical stimulation in a liquid environment. **(b)** The energy difference between folded and flat graphene at different folding angles. Reproduced from Zhang *et al.* (2010).

(d) **Single-sided hydrogenation**

This technique was successfully implemented by Zhu and Li (2014) to fold graphene into a three-dimensional nanocage, and it is based on the accumulated structural distortions induced at each hydrogenated site (Figure 2.7) which effectively constrain the monolayer to fold along the hydrogenation lines.

(e) **Nano-indentation**

This technique relies on the use of pressure to induce a localised sp^2- to sp^3-hybridized carbon transformation within graphene and form what could be considered as a 'crease line' which facilitates fold formation (Figure 2.8).

(f) **Topological defect patterning**

It has been shown that structural defects in graphene alter the spatial geometry of the atoms in their immediate vicinity (Figure 2.9). This approach entails the creation of site-specific topological defects in graphene to produce the paper-equivalent of 'folding lines' which would, in turn, activate and guide the folding process of the nanosheet into a pre-determined conformation (Zhang *et al.*, 2014b).

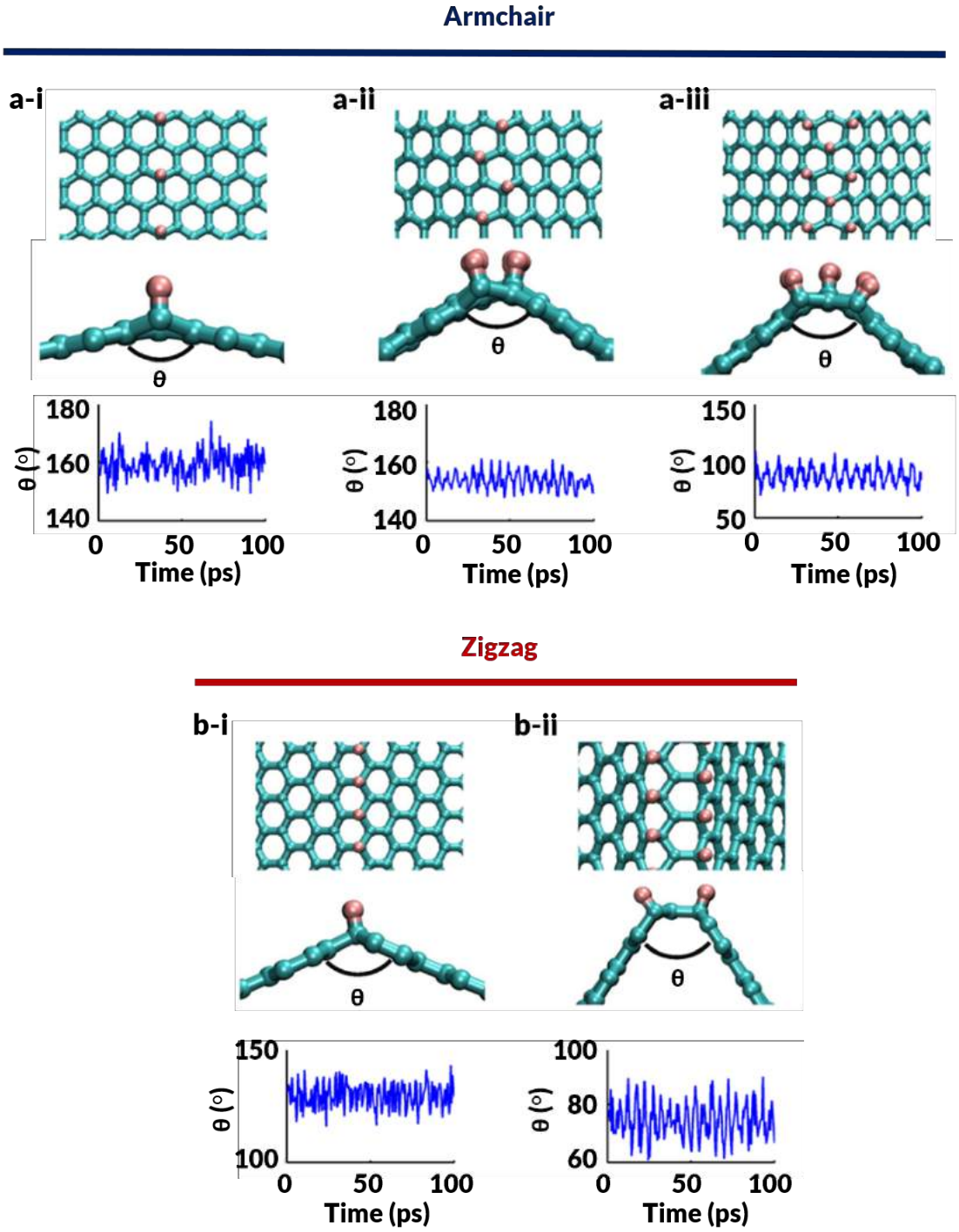

Figure 2.7: Top view, side view, and fold stability plots recorded at 300K for graphene with different single-sided hydrogenation line patterns. **(a)** *(i)* One-line, *(ii)* two-line, and *(iii)* three-line hydrogenation along the armchair direction of graphene. **(b)** *(i)* One-line and *(ii)* two-line hydrogenation along the zigzag direction of graphene. Reproduced from Zhu and Li (2014).

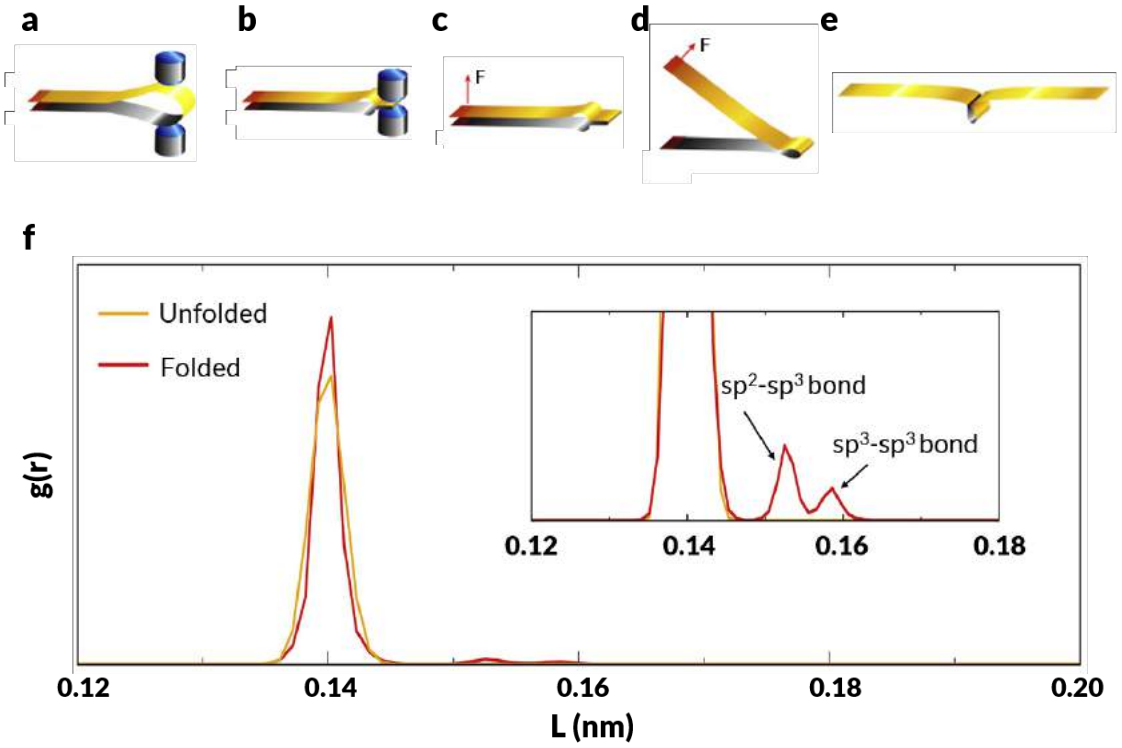

Figure 2.8: (a-e) Schematic representation of the nano-indentation process to introduce a crease line in a graphene nanoribbon. **(f)** The radial distribution curve of the carbon atoms present at the folding site in creased graphene compared with those from an unfolded, pristine section. Reproduced from Wei *et al.* (2020).

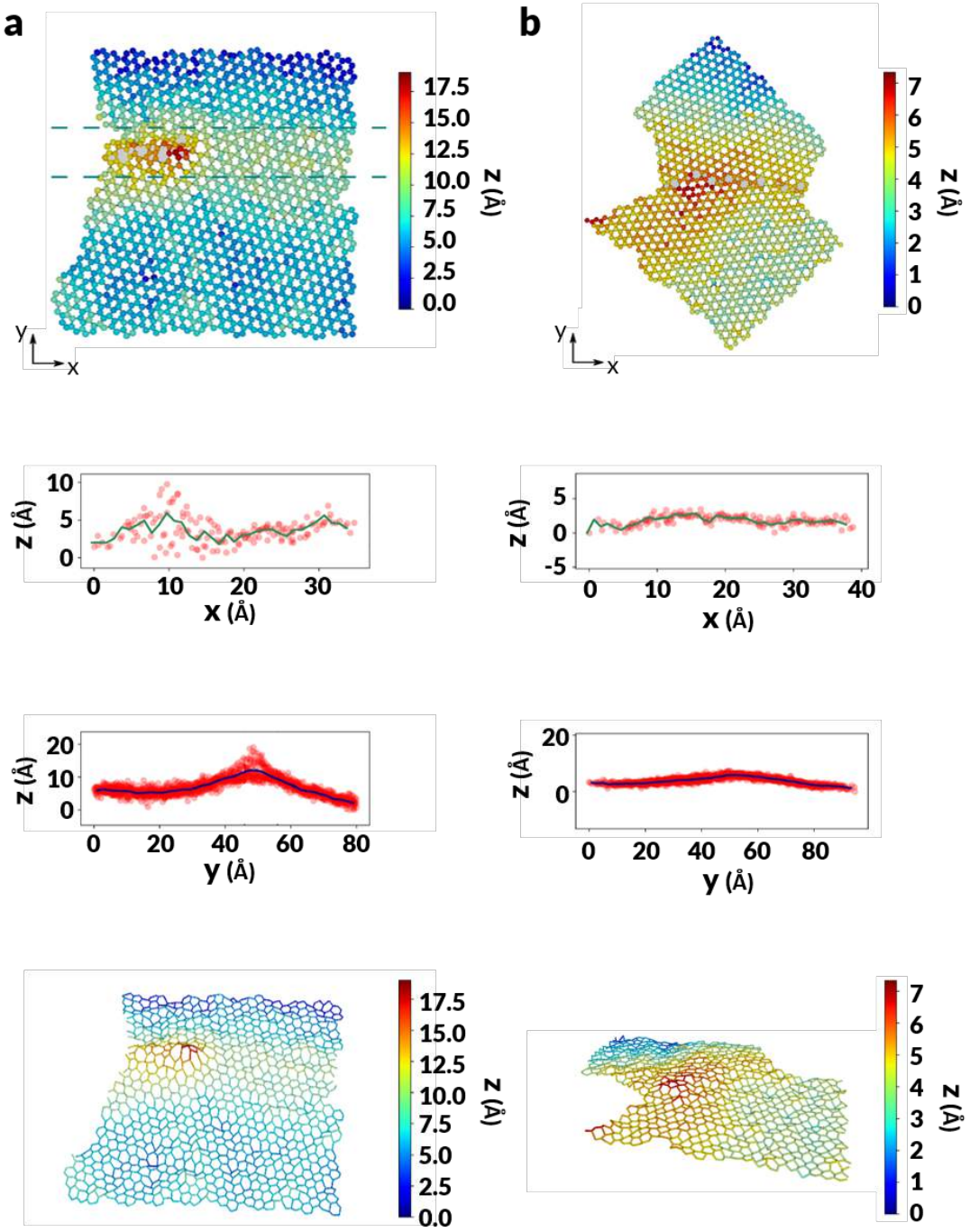

Figure 2.9: Atomic structures of two representative grain boundaries in graphene with a misorientation angle θ of **(a)** *c.* 2.6°and **(b)** *c.* 23.6°. Reproduced from Hofer *et al.* (2018).

2.4 | Fold-mediated control of existing properties in graphene

In recent years, numerous studies have been published in relation to the enhanced properties manifested by graphene in its various forms. It is beyond the scope of this work to discuss in detail all such developments. Instead, this section only focuses on a small selection of such studies which are meant to illustrate the outstanding properties and practical applications of folded graphenes.

2.4.1 | Electrical conductivity

2.4.1.1 | Folded graphene and semiconductivity

Compared to previous decades, current year-on-year performance and power improvements for microprocessors are showing signs of stagnation, largely due in part to the physical limitations associated with silicon transistors. This has led to speculation about the future role of carbon-based electronics within the semiconductor industry and the likelihood of replacing silicon in the long term (Friedman *et al.*, 2017; Guisinger and Arnold, 2010). Graphene, in particular, displays some exceptional electronic properties which makes it a strong candidate in this regard. For instance, the carrier mobility of graphene is much greater relative to silicon – by a factor of 200 (Lin *et al.*, 2011). Such an extraordinarily high value has been attributed to a lower incidence of carrier scattering from fewer electron–phonon interactions within the monolayer (Radamson, 2017).

However, there is a severe limitation for graphene to be integrated within conventional transistors: the absence of an energy band gap. As a result, pristine graphene is precluded from the ability to switch back and forth between an insulating and conducting state with the use of control voltages. This issue can be resolved to a certain extent, according to Oostinga *et al.* (2008), by the application of an electric field orthogonal to the plane of two stacked graphene

sheets, a system which is not dissimilar to folded graphene, which causes a band gap to open. The authors of this study posited that the induced band gap derives from a breakdown of the inversion symmetry in the band structure of the bilayer system (Figure 2.10). In a later study by Zhang *et al.* (2009), it was reported that this gate-tunable band gap can extend into the mid-infrared range and reach a maximum of 250 meV, which is considerably lower than its silicon counterpart. Nonetheless, some potential uses of dual-gate bilayer graphene field-effect transistors (FETs) include the development of novel nanophotonic devices for IR generation, amplification, and detection (Qin *et al.*, 2017).

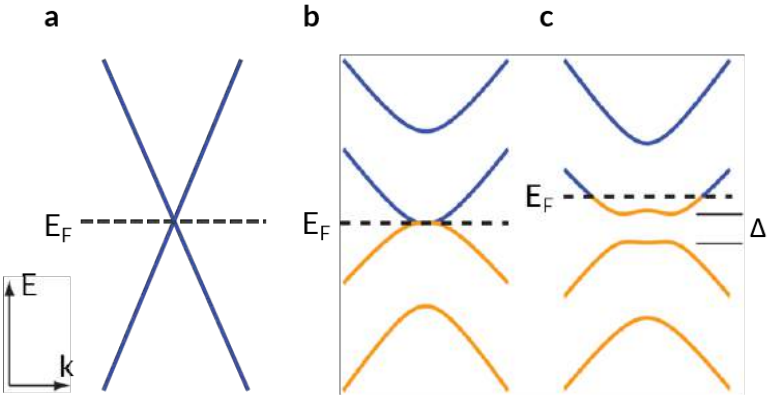

Figure 2.10: The electronic band structure of **(a)** monolayer graphene, **(b)** bilayer graphene, and **(c)** bilayer graphene with an applied electric field (perpendicular to the bilayer plane) whose presence shifts the Fermi energy E_F to produce a non-zero band gap Δ. Adapted from (Zhang *et al.*, 2009).

A different strategy which seems to achieve wider band gap openings in graphene is strain engineering. Initial measurements made by Lee *et al.* (2013) put the allowed tunable range of folded graphene systems between 0.14 eV and 0.19 eV. However, an observation made by Bai *et al.* (2014) of two minima in the local density of states of folded graphene, each measuring *c.* $V_{bias}\pm0.9$ eV (i.e. a four-fold increase), indicates the possibility of achieving wider band gaps with magnified nanoripple action. These minigaps are attributed to Bragg scattering at principal superlattice harmonics (Song *et al.*, 2013).

2.4.1.2 | Folded graphene and resistivity

Resistivity and folded graphene have long been associated with each other since one of the prime features of graphene is its electrical conductivity, and, as explained earlier, folds used to be treated solely as an undesirable feature which degraded this exceptional property. Research suggests that the resistivity profile along a graphene fold is noticeably lower compared to its planar counterpart, with the largest discrepancy being observed close to the charge neutrality point (Figure 2.11) when the gate voltage is able to shift the Fermi energy from the valence band to the conduction band (Zhu *et al.*, 2012). This phenomenon is attributed to interlayer tunnelling (Uryu and Ando, 2005), as indicated by the unusually weak dependence of resistance on the fold length (Figure 2.12). Another aspect that is relevant to the discussion on the resistivity of graphene in the presence of folded domains concerns the orientation of the fold with respect to the applied current. Transport across a graphene wrinkle, including (but not limited to) charge carrier ability, was shown to be weaker than that along the wrinkles (Deng *et al.*, 2016; Hallam *et al.*, 2015; Ni *et al.*, 2012; Zhang *et al.*, 2014a; Zhu *et al.*, 2012). Similar observations of anisotropic conductive behaviour were also made by Gannett (2012) whose measurements of current across and along a graphene fold demonstrated that the presence of the fold could alter the minimum conductivity of the material.

The transport properties of folded graphene nanoribbons (GNRs)were also found to vary according to the stacking arrangement of the layers, the folding angle, and the sheet edge type (Xie *et al.*, 2012). In particular, the tuning of the folding angle for the AA-stacked type[2] was shown to indirectly influence the conductivity of the material by modifying its stacking arrangement which, in turn, has an effect on the interlayer coupling. With a folding angle of 60°, the stacking arrangement close to the fold was found to be different from the rest of the bilayer

[2]AA stacking in graphite refers to systems where in two adjacent layers, two identical atoms stack on atop each other, as opposed to AB stacking where the second layer is shifted.

region. This decoupling breaks the conductance symmetry and produces a region highly reflective to electrons. On the other hand, a 120°folding angle produces consistent stacking of the AB type, which leads to reflectionless transmission in the junction, and hence a higher conductance (Figure 2.13). Confirmation that the anisotropic conductivity is due to the behaviour of the charge carriers in the presence of folds can be found in the ultrafast terahertz (THz) spectroscopic analysis of folded graphene (Hallam *et al.*, 2015) (Figure 2.14).

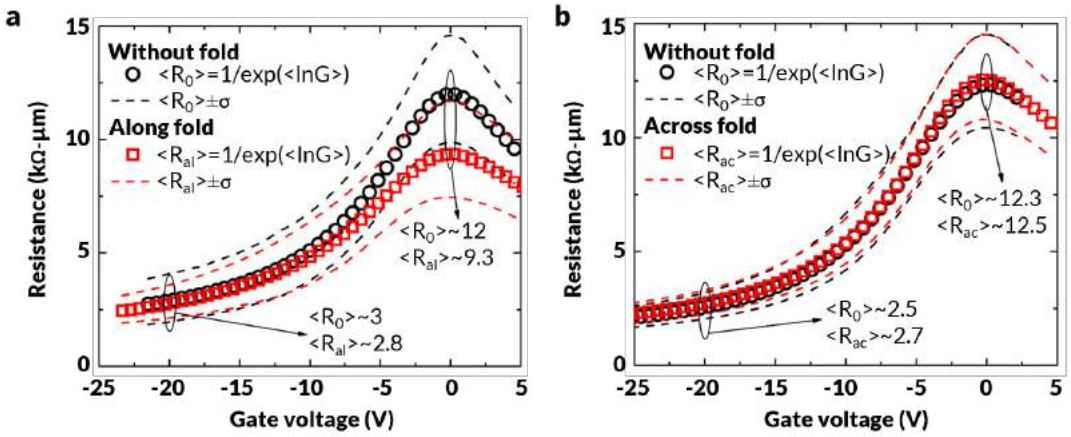

Figure 2.11: Distinct anisotropy in the electrical resistivity of wrinkled graphene **(a)** along the fold $<R_{al}>$ and **(b)** across the fold $<R_{ac}>$ as a function of gate voltage (V), alongside a comparison between them and the averaged resistance at regions where graphene is considered to be relatively flat $<R_0>$. Reproduced from Zhu *et al.* (2012).

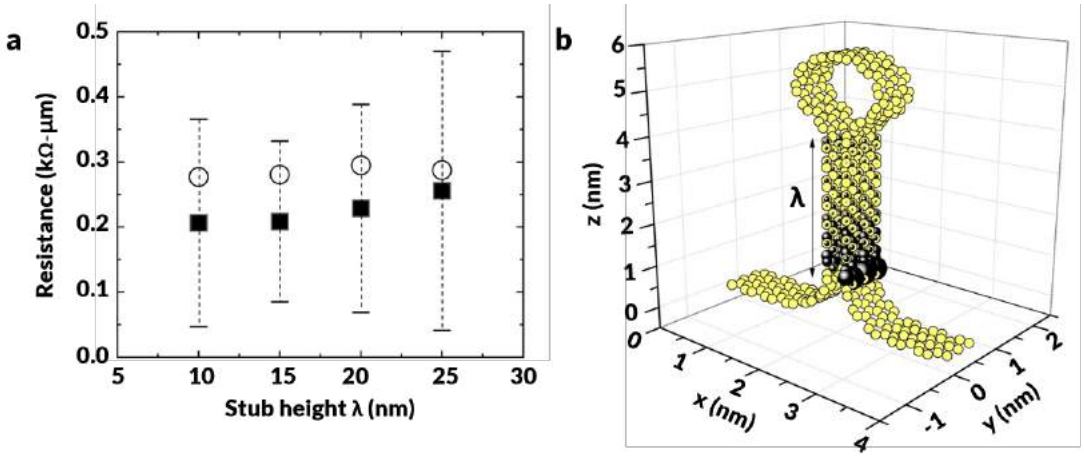

Figure 2.12: (a) Quantum transport modelling for the room-temperature resistance of a standing graphene wrinkle like the one shown in **(b)** at different lengths of the bilayer region λ (filled squares), as reported by Zhu *et al.* (2012). Calculations were also repeated with the top of the wrinkle cut off to suppress purely intralayer current (open circles).

In a later study, Willke *et al.* (2016) probed CVD-grown graphene using Kelvin probe force microscopy (KPFM) to measure localised changes in resistance by the voltage difference at the folded locations. Their findings appear to suggest that previous studies tended to overestimate the influence of wrinkling on the total resistance within the nanosheet since they showed that each wrinkle, on average, was responsible for an increase in resistance of *c.* 80 Ω µm. This is significantly lower than the 200 Ω µm value reported by Clark *et al.* (2013) that derived from experimental measurements, and well outside the 200 Ω µm to 300 Ω µm range postulated by Zhu *et al.* (2012)in a theoretical study which was based on the non-equilibrium Green's function (NEGF) method. An interesting study which was done recently reported that monolayer graphene may experience as much as a 36-fold change in electrical conductivity upon the introduction of wrinkles within its structure (Ma *et al.*, 2020) (Figure 2.15).

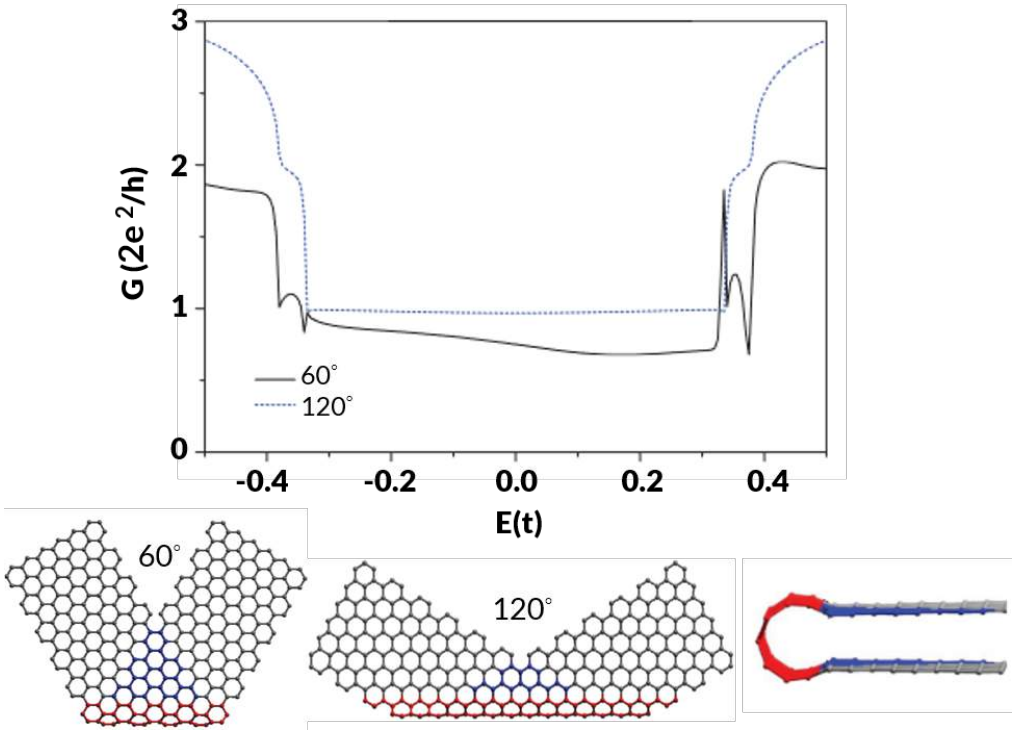

Figure 2.13: *Top*: The conductance profile of folded AA-stacked graphene at a folding angle of 60°and 120°. *Bottom*: A graphical rendering of folded bilayer GNR; the folding regions and bilayer portions are marked in red and blue, respectively. Adapted from Xie *et al.* (2012).

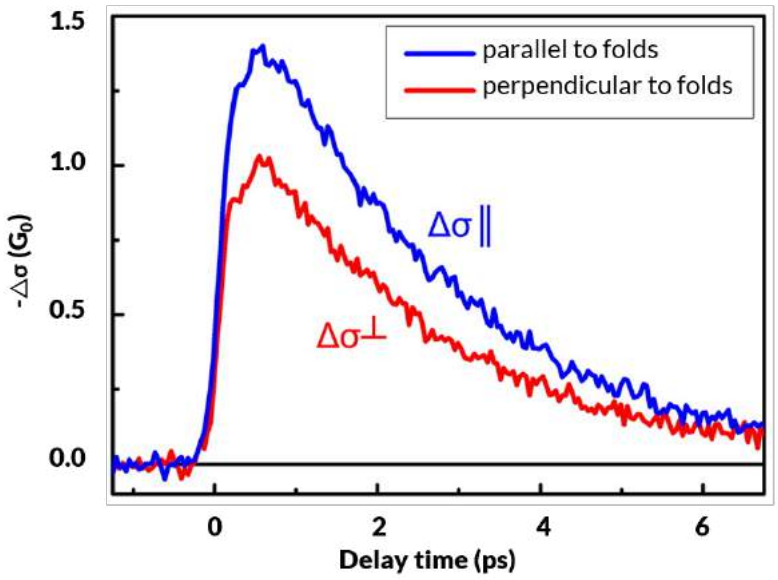

Figure 2.14: Anisotropic electron mobility along and perpendicular to graphene folds as measured by Hallam *et al.* (2015) using ultrafast teraHertz spectroscopy.

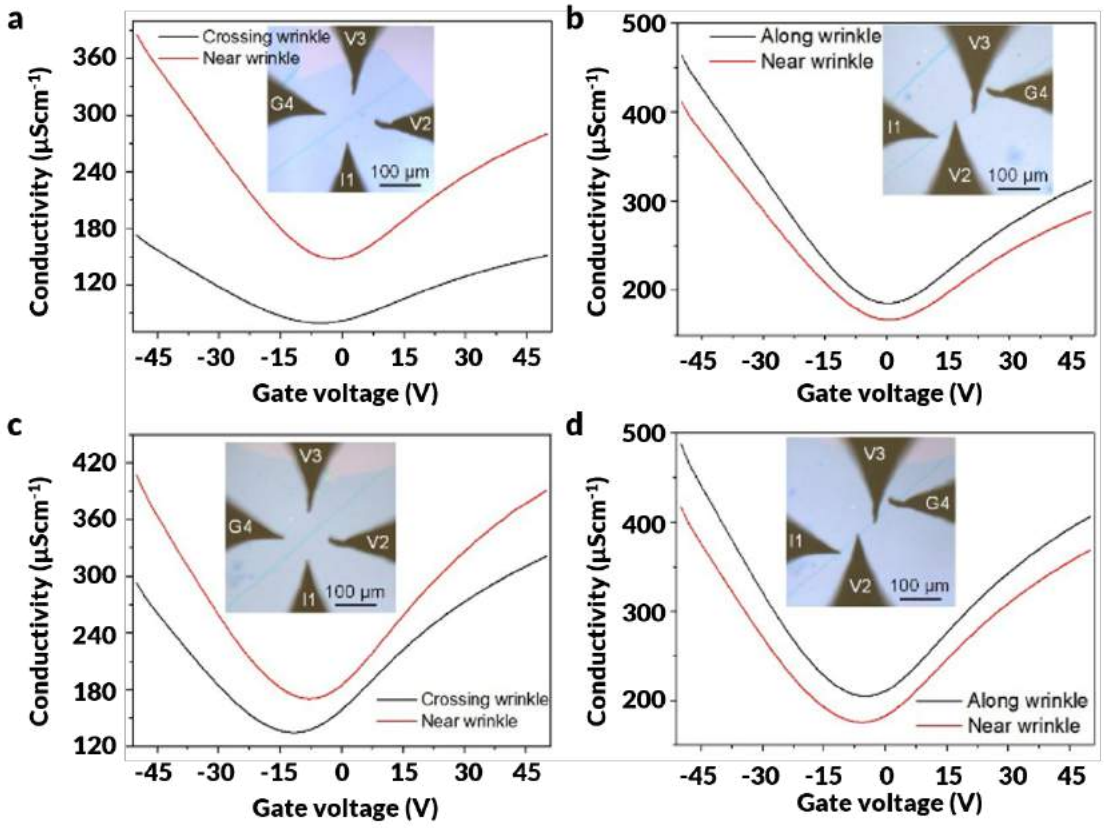

Figure 2.15: Gate-tunable conductivities of two graphene wrinkles **(a)** crossing the wrinkle and **(b)** along the wrinkle, from four-point-probe microscopy measurements performed by Ma *et al.* (2020).

2.4.2 | Thermal transport

Heat transfer in macroscopic, homogeneous systems is governed by Fourier's Law which treats thermal conductivity as an intensive property i.e. independent of the geometry and size of the material. However, in the case of (quasi) two-dimensional systems, thermal conductivity behaves in the opposite manner. In fact, graphene was found to be in violation of Fourier's Law because the thermal conduction was observed to be logarithmically divergent with sample length, even when the length exceeded the average phonon mean free path (Xu *et al.*, 2014b). This anomalous behaviour was attributed to the 2D nature of phonon activity within the nanosheet (Nika and Balandin, 2012; Xu *et al.*, 2014b), and it demonstrates that a proper discussion on heat conduction in graphene cannot exclude the dominant aspect of phonon scattering.

The superb thermal conductivity of graphene, which for a suspended sheet is reported to be in the neighbourhood of 5000 WmK^{-1} (Balandin *et al.*, 2008), raises its prospects of becoming the material of choice for thermal management devices (Huang *et al.*, 2020). Ouyang *et al.* (2011) applied the NEGF formalism to calculate the thermal conductance of folded GNRs at different folding angles and layer distances (Figure 2.16) and showed that thermal conductance in monolayer graphene can be reversibly tuned down by up to 40% by the action of folding.

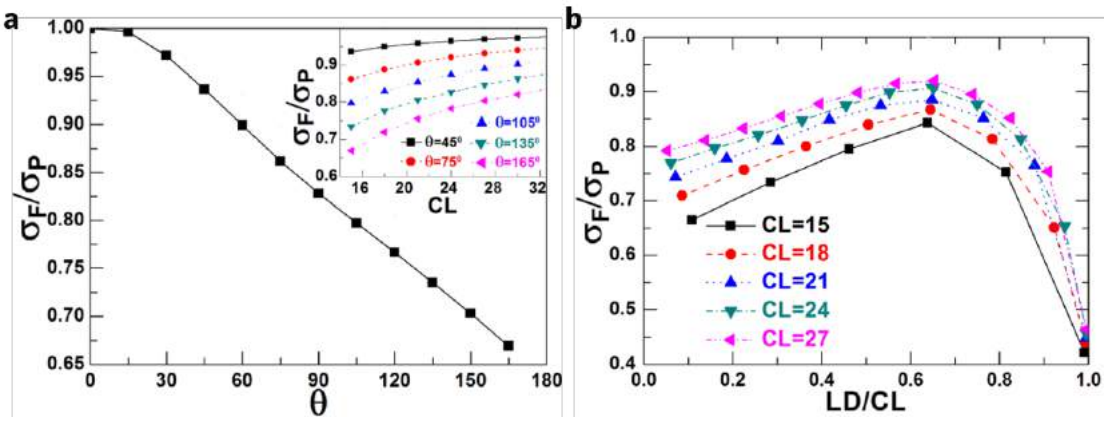

Figure 2.16: The effect of **(a)** the folding angle θ and **(b)** the layer distance-to-centre region length ratio on the thermal conductivity of armchair GNR of width $N_A = 9$ dimer lines, expressed in terms of the ratio between the corresponding flat (σ_F) and folded (σ_P) values. Adapted from Ouyang *et al.* (2011).

Yang *et al.* (2012) dynamically simulated the effect of folding on the thermal conductivity of GNRs. Their findings suggest that as the folds are pushed against each other (causing a reduction in the interlamellar space) and the number of folds is increased, the thermal conductivity tends to decrease (Figure 2.17) by as much as 70% in compressed, hexuply-folded GNR. Such behaviour was attributed to the increase in van der Waals interactions which induced more phonon scatterings besides those already present due to the strain at the folding sites. These are likely to be out-of-plane phonons, or ZA modes, which have been theorised to be the dominant contributor to thermal conductivity in graphene at room temperature (Lindsay *et al.*, 2011). Indeed, the phonon transmission spectra calculated using the NEGF method show a decline in thermal conductivity from strong scattering of low frequency modes at the folds (Figure 2.18), which is much different from other high frequency phonon scattering by impurities, dislocation, and boundaries. Such a reduction in thermal conduction that is achieved through folding could be useful in thermoelectric devices where an adjustable heat flow is necessary, provided that the high electronic conductivity of graphene is also preserved (Sevinçli and Cuniberti, 2010).

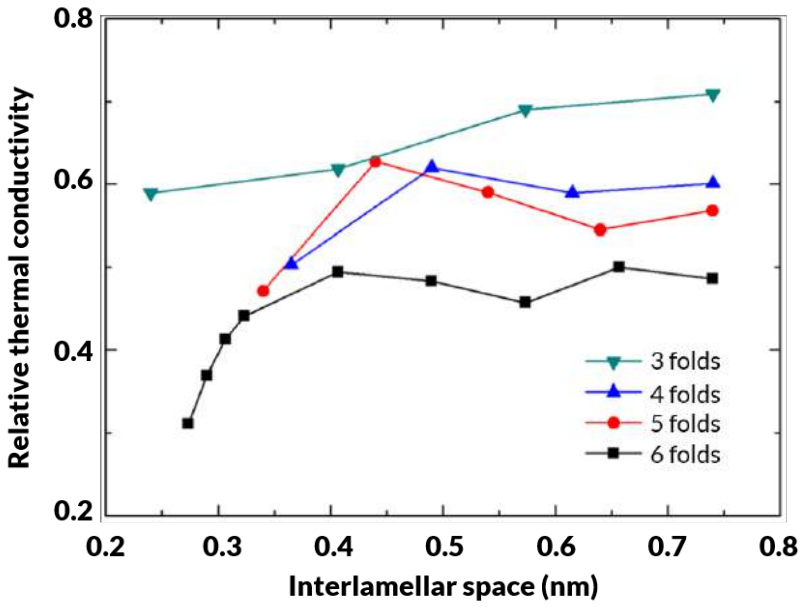

Figure 2.17: The thermal conductivity of folded GNR as a function of interlamellar space and fold frequency, relative to planar zigzag GNR. Reproduced from (Yang *et al.*, 2012).

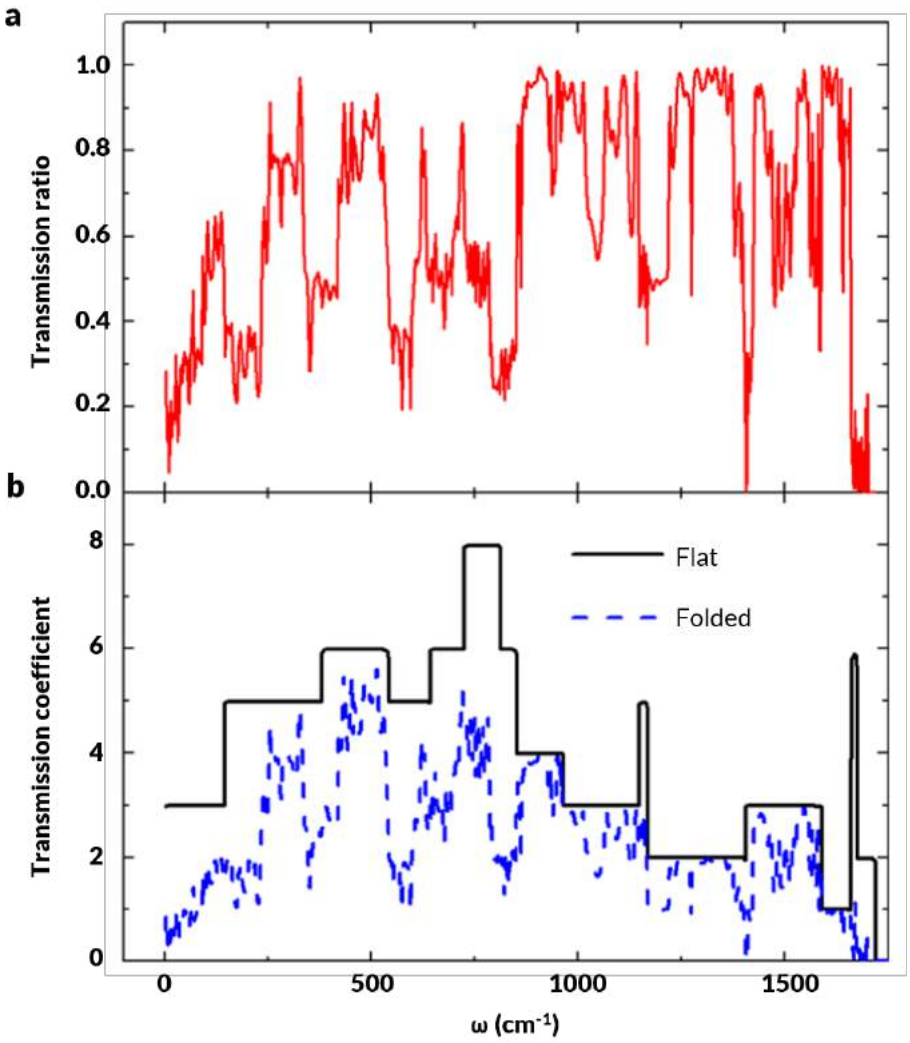

Figure 2.18: (a) The transmission spectra for flat and folded graphene, modelled via the NEGF method. **(b)** The variation in the ratio of the transmission coefficient of the folded GNR to the transmission coefficient of the flat GNR, across a phonon frequency range of $0\,\mathrm{cm}^{-1}$ to $1750\,\mathrm{cm}^{-1}$. Reproduced from (Yang *et al.*, 2012).

2.4.3 | Mechanical characteristics

Graphene, since its discovery, has been hailed as a material with some exceptional mechanical characteristics, which include its high stiffness, massive flexibility, as well as some interesting negative properties such as negative Poisson's ratio and negative stiffness characteristics.

As a quasi two-dimensional material, graphene possesses high flexibility (Lu *et al.*, 2009), which can be very useful in a number of applications. For instance,

it was reported that concrete composites that were treated with graphene flakes displayed a 146% enhancement in their compressive strength relative to standard concrete (Dimov *et al.*, 2018). It should however be mentioned that the flexibility comes at the expense of a relatively weak compressive strength, which has been theorised to be around 2 GPa for a suspended sheet (Lu *et al.*, 2009). Such a limitation can be overcome by embedding graphene into a matrix substrate which should provide the necessary support to limit the buckling behaviour upon applying compressive loads (Tsoukleri *et al.*, 2009). In another study, Frank *et al.* (2010) employed a cantilever beam for the measurement of buckling strain in graphene flakes. Their work demonstrated that by embedding graphene in plastic beams, its buckling strain is enhanced.

More relevant to the present work is a strategy for enhancing the out-of-plane rigidity of the monolayer through the formation of van der Waals interactions between sections of the sheet as a result of folding. Zheng *et al.* (2011) evaluated the mechanical performance of a triply folded GNR termed "grafold" using molecular dynamics simulations. In this particular conformation, graphene increased its maximum compressive strength by more than an order of magnitude (Figure 2.19) and, unlike the tensile case, compressive deformation was elastic within the studied range of -0.001 to -0.137. The same study also found that the folded structure retained the high tensile strength characteristic of planar graphene. In view of these findings, a likely avenue for the use of grafold and other folded graphene analogues is in damping devices.

With regards to anomalous properties, crumpled graphene was found to display **non-Hookean mechanics** when compressed hydrostatically and uniaxially (Baimova *et al.*, 2015) (Figure 2.20). In the latter case, the elasticity limit was attained at a comparatively high density (1.5 $\mathrm{g\,cm^{-3}}$), something which the authors attributed to the more prominent lattice distortions in graphene under hydrostatic pressure that lead to a more densely packed structure with increased van der Waals interactions.

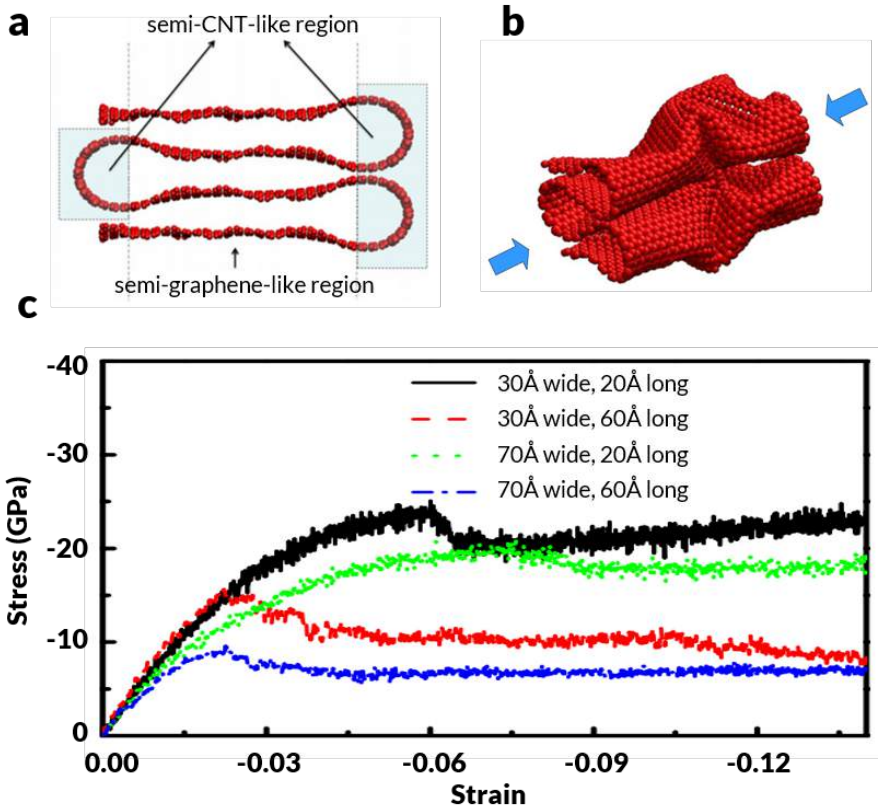

Figure 2.19: The compression characteristics of grafold: a triply folded GNR. **(a)** Side-view of grafold with its CNT-like portions highlighted for emphasis. **(b)** The appearance of grafold under uniaxial compression. **(c)** Stress-strain curves for differently sized grafolds. Reproduced from Zheng *et al.* (2011).

Another anomalous mechanical property is that of **negative stiffness**, a phenomenon whereby a material "pushes back" when it is stretched. This highly anomalous characteristic started to gain prominence through the work by Lakes (2001) and Nicolaou and Motter (2012) who reported this property in what could be described as 'mechanical metameterials'. However, the notion of negative stiffness was pioneered by the work of Molyneux (1957) who proposed a device made from springs which can demonstrate this effect at a macroscopic level.

One of the initial reports that brought attention to the aspect of negative tangent modulus in folded graphene was Gauci (2018). More recent work by Lin *et al.* (2021) presented similar findings in the more complexly folded 'Miura-ori' graphene, thus adding credence to the hypothesis being put forward by the candidate that folded graphene can exhibit this anomalous property. However,

the manner in which Lin *et al.* (2021) chose to investigate negative tangent modulus in folded graphene differed from the approach taken by the candidate, primarily based on the fact that their modelled system was more complex in form, as illustrated in Figure 2.21. More importantly, due to the manner in which the system was folded, the form of graphene studied by Lin *et al.* (2021) can sustain much lower strains compared to the systems studied by the candidate, including the ones studied in the initial preliminary study (Gauci, 2018). Besides the negative tangent modulus, work by Lin *et al.* (2021) also highlighted the ability of their 'Miura-ori' folded graphenes to exhibit a negative Poisson's ratio, which complements earlier work by Grima *et al.* on other forms of graphene, namely crumpled/wrinkled graphenes (Grima *et al.*, 2015) and corrugated graphene (Grima *et al.*, 2015).

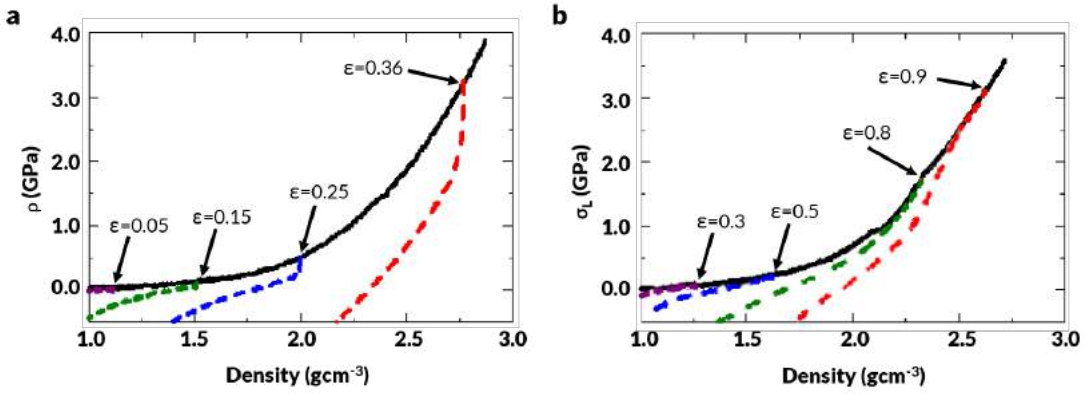

Figure 2.20: The loading and unloading curves of crumpled graphene (shown in solid and dashed lines, respectively) at specific strain levels, expressed in terms of the relationship between density and **(a)** hydrostatic pressure ρ and **(b)** uniaxial stress σ_L. Reproduced from (Baimova *et al.*, 2015).

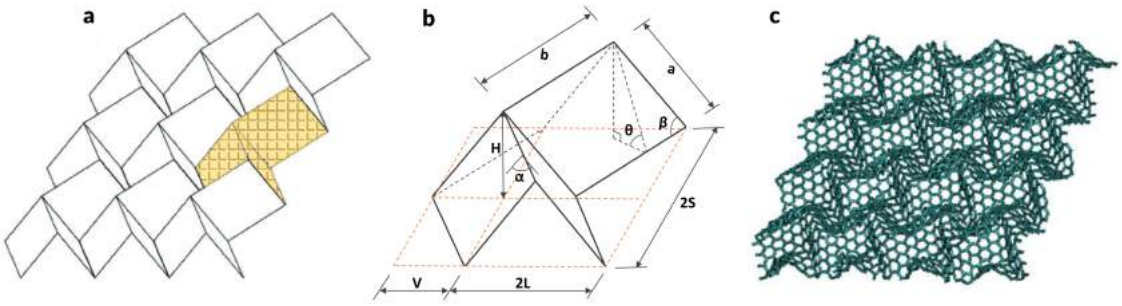

Figure 2.21: Miura-ori graphene. Adapted from Lin *et al.* (2021).

2.5 | The unfolding process of folded graphene

Apart from the studies reviewed so far regarding methodologies that could produce folds in graphene, there have also been isolated studies which focused on the unfolding process. These include work from Yi *et al.* (2014) that examined the effect of temperature on the stability of folded graphene by means of MD simulation. Another particularly important study was that from Yi *et al.* (2019) which investigated the "mechanical unfolding of self-folded graphene on flat substrates" experimentally via AFM manipulations and also computationally through the use of MD simulations. This study revealed that *(i)* it is possible to control and manipulate the folding conformation of graphene via AFM, and *(ii)* the folding/unfolding process is reversible, something which has major implications for the use of graphene in nanoscale origami devices.

Work performed by the candidate in an initial preliminary study examined a corrugated graphene system through a combination of static force-field-based simulations using the PCFF force-field and NPT-based, MD simulations using the AIREBO force-field (Gauci, 2018). This system was realised by the intentional placement of 5-8-5 vacancy-type in the form of parallel defects lines which served to activate and guide the system to fold in a pre-determined way. Results indicated that this folded system may exhibit negative tangential stiffness, as well as zero Poisson's ratio. The same study also showed that low-density corrugated forms of graphene are more likely to densify in order to attain additional stability from increased van der Waals interactions.

2.6 | Conclusion

This chapter has provided a representative, albeit not exhaustive, overview of the literature pertaining to folded graphene, with special focus being afforded to its production methods and exceptional properties. Moreover, it also managed to highlight the capability of folds to significantly alter some of the properties

that are present in the planar form of graphene. This dissertation will examine one such characteristic of this form of carbon, namely the anomalous stiffness characteristics of folded graphene as it is being stretched.

Aims of this Work

The previous chapters have outlined how the distinctive ability of graphene to fold onto itself presents an opportunity for the material to adopt complex conformations whose properties – particularly those that are sensitive to strain-induced structural modifications – are actively being researched.

Despite the considerable literature which has accumulated over the previous decade on the subject of folded graphenes, at the time of writing, **few reports exist regarding their mechanical properties**. One such report investigated, through a combination of computational chemical modelling and atomic force microscopy, the unfolding process of a z-shaped, multi-folded graphene segment into a planar configuration (Yi *et al.*, 2019). Unfortunately, since this study limited itself to assessing the influence that the stacking mode had on the unfolding process, **the stress-strain response of the folded graphenic system remained unexamined**.

A far less researched aspect of folded graphenic systems relates to the possibility that **the presence of folding domains may give rise to anomalous negative mechanical properties**. For instance, by means of molecular dynamics (MD) simulations, it was shown that the Poisson's ratio for copper-reinforced, folded graphene composites of the Miura-ori tessellation can achieve a negative value in the in-plane direction (Lin *et al.*, 2021). Despite this, the study failed to report on the possible manifestation of **negative tangent modulus** within such forms of folded graphene, even though it would have been predictively weak on account of the small folding amplitudes which characterised the systems under consideration. An earlier study by the candidate (Gauci, 2018) had managed to identify a set of stable, folded graphene conformations, and although they possessed an adequately large amplitude for a pronounced manifestation of negative tangent modulus, the methodology that was chosen for examining such systems ignored ambient conditions and focused exclusively on minimising the systems' energy content.

In view of these *lacunae*, the present work **proposes and examines a number of novel folded forms of graphene** where the folds are artificially inserted. The systems are **specifically designed with a large folding amplitude to sustain large strains**, thus overcoming the principal limitation in the study by Lin *et al.* (2021).

Cognisant of the fact that folded graphenes display strong structure-property relationships whereby their structure dictates the properties being manifested, an important part of this work involves **an assessment of the morphology of the proposed folded systems** with an emphasis on understanding the mechanisms that impart stability to these folded systems and prevent them from unfolding. This is followed by a study of their mechanical properties, focusing on the behaviour of these folded graphemic systems as they are stretched open by an applied uniaxial tension load. Its scope is to **obtain the stress-strain profile for these novel folded graphene systems and to provide more conclusive evidence as to whether such folded conformations exhibit negative properties such as negative tangent modulus or 'push-back' behaviour**.

In contrast to earlier work presented by the candidate, **the folded systems are studied via MD simulations** rather than simple energy minimisations. MD simulations provide a dynamic and more realistic representation of the systems under consideration, although they necessitate substantially more computational resources and must be performed with sufficiently large systems in order to ensure a proper equipartitioning of energy.

Finally, in an effort to **ascertain the validity of the MD protocol thus developed for simulating the uniaxial deformation of the folded graphene systems**, an extended self-validation study is initially performed using regular (non-folded) graphene systems to ensure that the reported mechanical properties are in good agreement with empirical data.

3

Methodology Development: Modelling of Unfolded Pristine Graphene and Reproduction of Its Properties

Chapter Highlights

- This chapter describes and validates a procedure for simulating the uniaxial deformation of suspended graphene-type systems in vacuum at 300 K.
- Samples of graphene are constructed for use within the LAMPPS environment.
- An energy expression is set up using the AIREBO potential.
- Simulations are performed which produce results that replicate well the stiffness characteristics of graphene as reported in the literature.

3.1 | Introduction

Despite the remarkable progress made recently towards devising strategies capable of effecting atomic-level morphological changes to graphene (Chen *et al.*, 2019; Wakafuji *et al.*, 2020), the current state-of-the-art techniques in this field still need to be improved further to be able to physically produce complex nanoscale systems like those which are considered in this dissertation. Consequently, due to limited experimental data regarding multi-folded graphenes, it was not feasible to adequately validate a modelling-based methodology – designed to predict the mechanical properties of folded graphenes – based entirely on empirical data that originated from such conformations.

Unfortunately, the reports published thus far regarding modelling studies on folded graphenes were, for the most part, not intended to simulate their

unfolding characteristics from a mechanical perspective. The few available ones on this topic, like the study by Lin *et al.* (2021), did not meet the requirements of the present work, namely to simulate suspended folded graphenes. This meant that there was no 'off-the-shelf' modelling protocol which had been developed, tested and validated with the specific intent to simulate the mechanical properties as required by the present work.

Thus, bearing in mind these limitations, an 'in-house' protocol first had to be developed and validated. The methodology development, and more importantly its validation, were guided by the need to reproduce specific mechanical properties of pristine graphene as reported in the literature, namely its **stress-strain profile** and **Young's modulus** (see Table 3.1). Both properties can be directly measured from uniaxially stretching a material.

Table 3.1: Selected literature reporting on theoretical predictions and experimental measurements for the Young's modulus of pristine graphene.

Reference	**E (TPa)**	**Method**
Hernandez *et al.* (1998)	1.20	Tight-binding
Kudin *et al.* (2001)	1.03	Density functional theory
Liu *et al.* (2007)	1.05	Density functional theory
Lee *et al.* (2008)	1.00	Experimental
Zhao *et al.* (2009)	1.01	Molecular dynamics
Zhao *et al.* (2009)	0.91	Tight-binding
Sakhaee-Pour (2009)	1.04	Structural mechanics
Zakharchenko *et al.* (2009)	1.04	Monte Carlo
Tsai and Tu (2010)	0.91	Molecular dynamics
Frank *et al.* (2011)	1.00	Experimental
Wei *et al.* (2011)	0.95	Molecular mechanics
Wagner *et al.* (2011)	1.08	Density functional theory

Standard graphene was the material of choice for this validation study because *(i)* it is the closest material to folded graphene, and *(ii)* its structural and mechanical characteristics are well documented in the literature, the latter having been measured by several research groups using different techniques that include atomic force microscopy (Lee *et al.*, 2008) and Raman spectroscopy (Frank *et al.*, 2011). This ensured that the simulated results were easily verifiable, thus providing a means for assessing the validity of the simulation protocol that was developed.

3.2 | Simulations

Briefly, the simulation protocol consisted of the following main components:

1. The construction of models representing armchair and zigzag graphene;
2. The setting up of an appropriate energy expression which computed the potential energy of the system as a function of the atomic coordinates and cell parameters;
3. The simulation of the constructed graphene models as though they were suspended in vacuum at 300K while being held from both ends in an unstretched state;
4. The simulation of uniaxial stretching.

A simplified overview of the process flow executed by this protocol, highlighting the relationships between the different programmatic steps involved, is presented in Figure 3.1.

Unless otherwise stated, simulations were performed on desktop workstations running Ubuntu Linux version 20.04 LTS, equipped with a 12-core Intel Xeon W-2235 processor and 64 GB of DDR4 RAM.

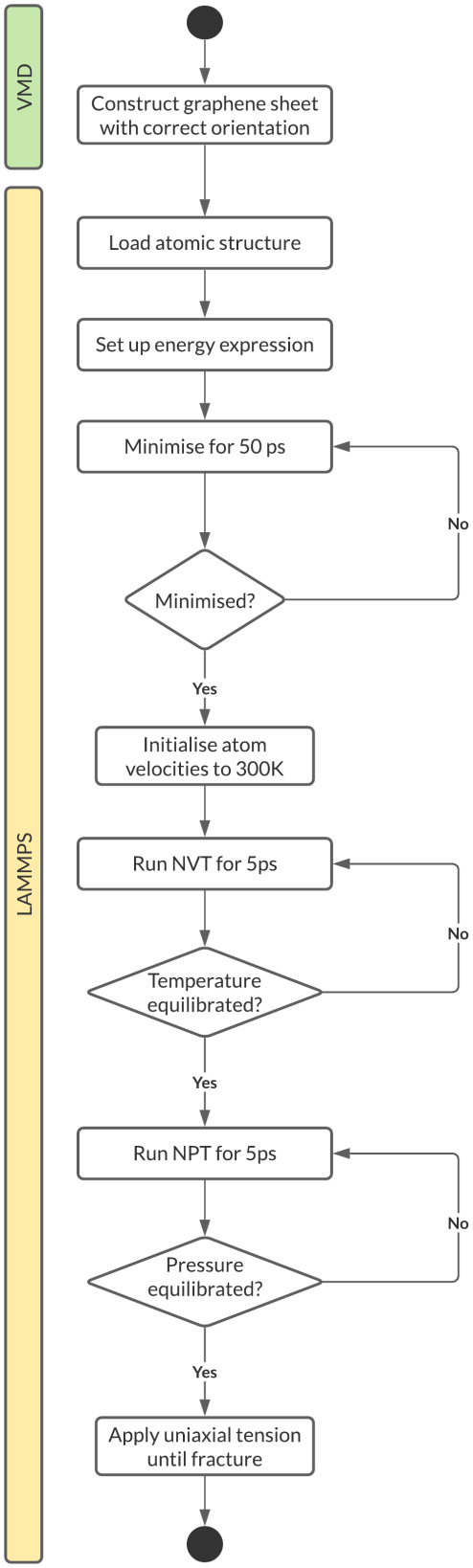

Figure 3.1: A flowchart outlining the principal components of a LAMMPS protocol that was specifically designed for modelling the uniaxial tensile stress behaviour in folded graphene systems.

3.2.1 | Construction of the models

This section describes the process involved in constructing pristine graphene systems for the purpose of simulating their tensile behaviour.

Since the hexagonal symmetry of graphene at low strain values may be considered to be valid, corresponding values for the Young's modulus are usually reported as though the property is isotropic (see Table 3.1). However, the same assumption does not hold at high strains, resulting into the manifestation of anisotropic mechanical properties (including the Young's modulus) along different loading directions (Ni *et al.*, 2010).

Therefore, in order to simulate the anisotropic character of the stress-strain relationship in graphene, two possibilities were available:

(i) write multiple LAMMPS input scripts, each for stretching a common graphene sample along a different direction, or

(ii) write a single LAMMPS input script whereby stretching was to be applied along the same direction, but multiple graphene samples needed to be generated and set to a particular orientation in order to be stretched along a different direction.

There are obvious advantages in writing a single LAMMPS script to simulate uniaxial stretching along the same direction and validating this property, if need be, with samples oriented in different directions. Hence, for the purpose of this validation study, two differently oriented samples of graphene were constructed in the xz-plane (see Figure 3.2), whereas the subsequent uniaxial tensile simulations were conducted via the same set of LAMMPS input commands, producing two independent sets of measurements. Construction of these two differently oriented systems was such that loading in the x-direction i.e. the designated stretching direction, corresponded to an applied tensile stress which was orthogonal to the armchair pattern in one instance and orthogonal to the zigzag pattern in the other. The nomenclature that shall henceforth be adopted to

refer to these systems is 'zigzag' and 'armchair'; the zigzag conformation has its so-called zigzag direction aligned with the x-axis, as shown in Figure 3.2(a)), whereas the armchair conformation has its armchair direction aligned with the x-axis, as shown in Figure 3.2(b).

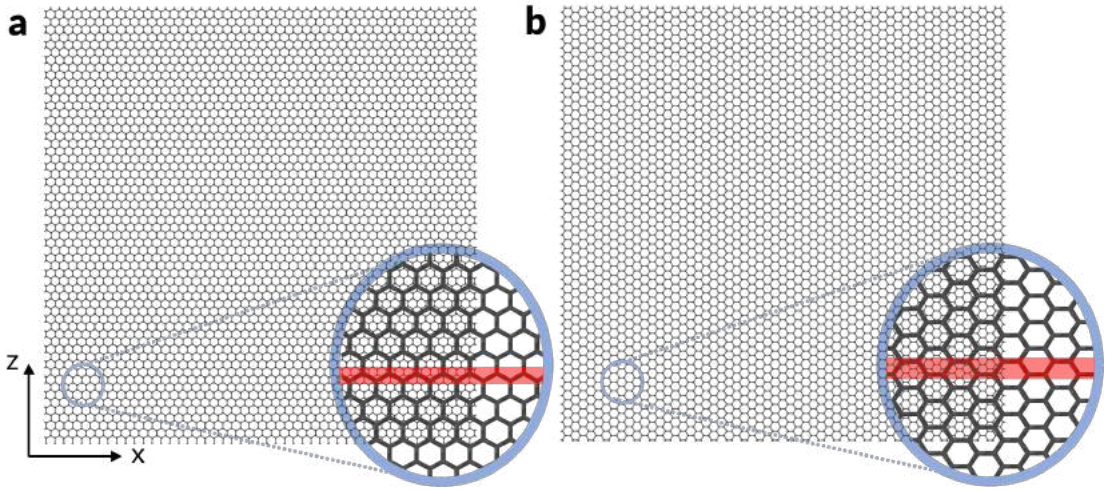

Figure 3.2: A visual representation of the pristine graphene sheets that were constructed using the VMD software as part of the validation process. Depending on the sheet orientation, the atomic pattern along the x-direction (highlighted in red) can either be **(a)** zigzag or **(b)** armchair.

The creation process of these pristine, unfolded graphene systems was facilitated by the TopoTools plugin (Kohlmeyer, 2016), a middleware script layer which came pre-packaged with VMD software version 1.9 (Humphrey *et al.*, 1996). In the end, two data files were generated, each representing a graphene sheet having 5684 atoms oriented in the (010) plane with either the zigzag or armchair pattern being parallel to the x-direction. For additional information about these files, refer to Appendix B.

The input code for generating the zigzag conformation was:

```
graphene -lx 12.000 -ly 12.000 -type armchair -cc 0.1418 -ma C-C
set sheet [atomselect 0 all]
$sheet move [transaxis x -90]
topo writelammpsdata FILENAME atomic
```

Line 1 generated the required atomic coordinates for a 12 nm$\times$ 12 nm crystalline hexagonal structure positioned in the xy-plane and comprised of carbon atoms with a C–C bond length of 1.418 Å. The edge termination pattern along the y-axis was specified as `armchair`, which meant that the corresponding atomic pattern along the x-axis was of the zigzag type. A 90° axis rotation about the x-axis (handled by Lines 2 and 3) repositioned the sheet to the desired xz-plane. Finally, Line 4 instructed VMD to create a file named `FILENAME` with information about the system in a format that could be later read into LAMMPS using the `read data` command. The inclusion of the `atomic` parameter ensured that the generated data file only contained the atomic coordinates of the constructed system.[1] A visual representation of the generated structure is shown in Figure 3.2(a).

An analogous procedure to the one described above was followed in order to generate the data file for the armchair graphene conformation (see Figure 3.2(b)). The only changes effected to the input code concerned Line 1 whereby the `-type` parameter was specified as `zigzag`.

It is important to mention that any data file generated by VMD (and subsequently inputted into LAMMPS) only contained a finite portion of a given structure without any indication as to whether LAMMPS should treat it as a two-dimensional periodic image. Therefore, information regarding the boundary conditions and dimensionality of the simulation box had to be defined directly within the LAMMPS script as indicated below:

```
5   dimension    3
6   boundary     p   m   p
```

Line 5 configured the simulation to run in three dimensions whereas Line 6 applied periodic boundary conditions in the x- and z-directions and a

[1] When using the AIREBO potential, bonds are generated implicitly according to preset atomic distances and hence, it is advisable to exclude such information from the data file as otherwise this may lead to missing atom pairs from the force-field computations. (Plimpton *et al.*, 2021)

non-periodic, 'shrink wrapped' boundary in the out-of-plane y-direction. 'Shrink-wrapping' means that rather than applying periodic boundary conditions of a fixed boundary in the out-of-plane y-direction, adaptive boundaries were used which in practice mean that the system was placed in a non-periodic-in-y box having a dimension in the y-direction which adapts to the size of the system. This ensured that the boundaries of the simulation box in the y-axis could adapt according to the atom positions during the course of each simulation, albeit with some restrictions which had to be manually included in the structure files. These restrictions consisted in an upper bound value of -0.5 Å for the lower face of the box and a lower bound value of 0.5 Å for the upper one. Overall, these specifications, which have been used successfully by others to represent graphene-type systems (Cai *et al.*, 2021; Hui and Chang, 2019), permitted an adequate representation of the monolayer suspended in space (vacuum) without any constraints in the out-of-plane direction. It is important to note that, at this stage, the constructed systems as defined by the respective data files were perfectly planar i.e. not exhibiting the usual rippled behaviour that is known to characterise suspended graphene sheets.

3.2.2 | Setting up of the energy expression

An important aspect of a molecular modelling simulation is the generation of a mathematical function which adequately describes the potential energy of the system being modelled in a manner that is detailed enough to correctly predict some of its desired properties and to do so in the most computationally efficient way possible.

Over the years, there have been different such formulations to study graphene, ranging from complex ones based on quantum mechanics (QM) to simpler representations which make use of the classical balls-and-springs (force-field) approach. QM-based methods, being the most representative formulations for materials to date, allow, contrary to force-field-based methods,

the study of those properties in graphene which relate to its electronic configuration, such as its adsorption capabilities (Nakada and Ishii, 2011) and electric conductivity (Radchenko *et al.*, 2014). However, due to the computational intensity that is required to perform these type of simulations, having limiting hardware resources inevitably leads to restrictions on the size of QM-modelled systems in order for such simulations to be completed within a reasonable timeframe. Thus, when a large system containing thousands of atoms needs to be modelled, QM-based simulations are impractical, if not undoable.

For the purpose of this work, since the properties that were going to be measured would not have included ones which would have been primarily dependent on the electronic state of the system, simulations were performed using the less computationally intensive force-field approach. More specifically, it made use of the Adaptive Intermolecular Reactive Empirical Bond Order (AIREBO) potential (Stuart *et al.*, 2000) which, in the LAMMPS simulation package (Plimpton, 1995), is invoked through the `airebo` pair style command: [2]

```
7  pair_style  airebo 3.0  1  1
8  pair_coeff  * * CH.airebo-rcmin C
```

Apart from proving its effectiveness in simulating the deformation behaviour of various kinds of graphenic systems (Becton and Wang, 2016; Becton *et al.*, 2014, 2015; Chang *et al.*, 2013), the AIREBO potential has also been successfully implemented in modelling studies which have examined the mechanical properties of graphene.[3] Such studies include work by Grima *et al.* (2015) on the modelling of defective graphene to assess its auxetic characteristics and an investigation by Peng and Sun (2020) on the mechanical strength of multilayer Cu/graphene composites.

[2] Line 7 defined the empirical potential of choice, a cut-off distance of 3 Å and the inclusion of the torsion and LJ terms in the energy expression.

[3] A Google Scholar search using the terms 'AIREBO' and 'graphene' returns over 3000 papers, of which more than 500 were published since 2020.

The publication of the AIREBO potential (Stuart *et al.*, 2000) offered a compelling alternative to the Tersoff (Tersoff, 1988) and Brenner potentials (Brenner, 1990) which, until that time, were the typical force-fields used for modelling hydrocarbon systems and thin films. This is because, unlike these two potentials, AIREBO can adaptively model the long-range van-der-Waals and Coulombic interactions and the single bond dihedral-angle interactions by having its energy expression constructed as a summation of three pairwise energy terms representing the bonding, non-bonding, and torsional interactions:

$$E = \frac{1}{2}\sum_{i}\sum_{j\neq i}\left[E_{ij}^{\mathrm{REBO}} + E_{ij}^{\mathrm{LJ}} + \sum_{k\neq i,j}\sum_{l\neq i,j,k} E_{kijl}^{\mathrm{tors}}\right] \tag{3.1}$$

Bonding interactions are modelled according to a Tersoff-type potential (Tersoff, 1988):

$$E_{ij}^{\mathrm{REBO}} = V_{ij}^{\mathrm{R}} + b_{ij}V_{ij}^{\mathrm{A}} \tag{3.2}$$

The repulsive term V^R is similar to the one present in the REBO potential proposed by Brenner (1990):

$$V_{ij}^{\mathrm{R}} = w_{ij}\left(r_{ij}\right)\left[1 + \frac{Q_{ij}}{r_{ij}}\right]A_{ij}e^{-\alpha_{ij}r_{ij}} \tag{3.3}$$

where Q_{ij}, A_{ij} and α_{ij} for C–C bonds are parameterised as 0.313 Å, 4.747 Å^{-1} and 10,954 eV. r_{ij} is the separation between atoms i and j. w_{ij} is a bond-weighting factor,

$$w_{ij}\left(r_{ij}\right) = S'\left(t_c\left(r_{ij}\right)\right) \tag{3.4}$$

which is responsible for disabling the bonding interactions whenever the typical bonding distances associated with the atom pairs is exceeded, signalling the unlikelihood for bond formation to occur. It is composed of a switching function $S(t)$ having the form:

$$S'(t) = H(-t) + H(t)H(1-t)\frac{1}{2}[1+\cos(\pi t)] \tag{3.5}$$

where $H(t)$ represents the Heaviside step function. The possible outcomes of $H(t)$ are:

$$H(t) = \begin{cases} 0 & t > 1 \\ 1 & t < 0 \end{cases} \tag{3.6}$$

switching smoothly within this range at intermediate t with a cubic spline. The other component of w_{ij} from Equation 3.4 is a scaling function $t_c\left(r_{ij}\right)$ which takes into account the distance between the atom pairs:

$$t_c\left(r_{ij}\right) = \frac{r_{ij} - r_{ij}^{\min}}{r_{ij}^{\max} - r_{ij}^{\min}} \tag{3.7}$$

The attractive term V^A is given by a triple exponential:

$$V_{ij}^{\mathrm{A}} = -w_{ij}\left(r_{ij}\right) \sum_{n=1}^{3} b_{ij}^{(n)} e^{-\beta_{ij}^{(n)} r_{ij}} \tag{3.8}$$

which also includes a bond-weighing factor so that it can be smoothly switched off for long-range interactions. Therefore, having switching function cutoffs, b^{min} of 0.77 and b^{max} of 0.81, ensures that the contribution of interatomic interactions is solely between non-reactive species. As per Equation 3.2, the bonding strength of V_{ij}^{A} is also modulated via the bonding term b_{ij} – a "quasi" bond order which accounts for an array of chemical effects that affect the covalent-type interactions of a system modelled via the AIREBO potential.

Non-bonding interactions are represented by the pairwise Lennard-Jones (LJ) 12-6 potential: [4]

$$V_{ij}^{\mathrm{LJ}}\left(r_{ij}\right) = 4\epsilon_{ij}\left[\left(\frac{\sigma_{ij}}{r_{ij}}\right)^{12} - \left(\frac{\sigma_{ij}}{r_{ij}}\right)^{6}\right] \tag{3.9}$$

For carbon-only systems like the ones examined in this work, the sole parameters of interest to the LJ term (and their corresponding values according to Stuart *et al.* (2000)) are σ_{CC} which should be 3.40 Å to match the interlayer separation of graphite, and the ϵ_{CCCC} which should be 0.3079 eV based upon the c_{33} elastic

[4] AIREBO-M is a variant of the AIREBO potential that replaces the LJ term with the Morse potential for obtaining better outcomes when simulating high-pressure systems.

constant of graphite. The reader is referred to Nosé (1984) for the parameterisation of the LJ potential. V^{LJ} is incorporated into the non-bonding term as:

$$\begin{aligned} E_{ij}^{\mathrm{LJ}} =& S\left(t_r\left(r_{ij}\right)\right) S\left(t_b\left(b_{ij}^*\right)\right) C_{ij} V_{ij}^{\mathrm{LJ}}\left(r_{ij}\right) \\ &+\left[1-S\left(t_r\left(r_{ij}\right)\right)\right] C_{ij} V_{ij}^{\mathrm{LJ}}\left(r_{ij}\right) \end{aligned} \tag{3.10}$$

having a different switching function compared to the one in 3.2.2:

$$S(t)=H(-t)+H(t)H(1-t)\left[1-t^2(3-2t)\right] \tag{3.11}$$

The gradual exclusion of the LJ term is modulated by the scaling function:

$$t_r\left(r_{ij}\right)=\frac{r_{ij}-r_{ij}^{\mathrm{LJ\,min}}}{r_{ij}^{\mathrm{LJ\,max}}-r_{ij}^{\mathrm{LJmin}}} \tag{3.12}$$

At intramolecular distances, the LJ interaction is included only if no significant bonding exists between the atom pair and if the atoms are not connected by two or fewer intermediate atoms, as specified by the t_b switch,

$$t_b\left(b_{ij}\right)=\frac{b_{ij}-b_{ij}^{\min}}{b_{ij}^{\max}-b_{ij}^{\min}} \tag{3.13}$$

The switch in Equation 3.13 is controlled by bond weights,

$$\begin{aligned} C_{ij}=1-\max\{& w_{ij}\left(r_{ij}\right), w_{ik}\left(r_{ik}\right) w_{kj}\left(r_{kj}\right), \quad \forall k \\ & w_{ik}\left(r_{ik}\right) w_{kl}\left(r_{kl}\right) w_{lj}\left(r_{lj}\right), \forall k, l\} \end{aligned} \tag{3.14}$$

If graphene was strictly a planar structure with C–C bond angles of 120° and equal bond lengths, then the torsional bond term would have been redundant. Such a degree of regularity in geomerty is not achieved in practice, given the rippled nature of the nanomaterial, so the bond term may play a more pronounced role. However, based on the work by Gayk *et al.* (2018), the exclusion of the torsional bond term would not have changed the outcome obtained. Therefore, in view of its reported small contribution to the overall potential and the added compuational effort associated with the inclusion of this term, it would have been justifiable to exclude the torsional bond term from the AIREBO function.

Throughout these simulations, the cut-off for the non-bond (Lennard-Jones) interactions was set to 3σ, where σ corresponded to a C–C bond length of 3.4Å. The longer-ranged interactions (which use a form similar to the standard Lennard Jones potential) were smoothly switched off between 2.16σ and 3.0σ, in line with the parameterisation of the AIREBO potential (Stuart *et al.*, 2000).

In general, this work kept the default parameters and settings as coded in the `CH.airebo` potential file that was made available in the October 2020 release of LAMMPS. The only exception concerned the adaptive cutoff parameter `rcmin_CC` which was set to 2.0 Å (from the default value of 1.7 Å) to avoid the unrealistically high bond forces in the near-fracture regime which manifest themselves by a non-physical, hardening effect (Shenderova *et al.*, 2000). This modification has been applied in analogous studies involving graphene (Peng and Sun, 2020; Zhang *et al.*, 2012; Zhao *et al.*, 2009).

3.2.3 | Simulation of the models in an unstretched state

This section validates the energy minimisation and equilibration procedures of the custom-designed simulation protocol through a rigorous assessment of the outcomes obtained when using armchair- and zigzag-directed graphene as reference systems.

3.2.3.1 | Minimisation protocol

The principal reason for performing an energy minimisation was to ensure that the bond length and bond angle data from the systems that were being modelled was consistent with the empirical findings. In practice, this was achieved by the removal of any artificial atom overlap which would have caused the simulation to cease prematurely. The section within the LAMMPS input script which codified the minimisation code was:

```
9   min_style cg
10  min_modify dmax 0.1 line forcezero
```

```
11  minimize 1.0e-10 1.0e-10 100000 1000000
```

The chosen minimisation algorithm (specified by the `min_style` keyword) was the conjugate gradient algorithm which is described by the LAMMPS documentation as follows: "At each iteration, the force gradient is combined with the previous iteration information to compute a new search direction perpendicular (conjugate) to the previous search direction." Compared with the steepest descent method, conjugate gradient is usually more robust and generally faster at reaching convergence (Plimpton, 1995).[5] Two parameters were explicitly specified for the standard implementation of the conjugate gradient algorithm in LAMMPS, namely the maximum allowed per-atom displacement in each iteration (`dmax`), and the line search algorithm (`line`). For the former, a distance of 0.1 Å was set and for the latter, the forcezero line search algorithm was chosen which operates initially using the backtracking method but once the system approaches a local minimum (and consequently the line search steps get smaller), it switches to a more robust quadratic line search (Shewchuk *et al.*, 1994).

The convergence criteria for this short minimisation process concerned *(i)* the energy change and *(ii)* the net force change on the system which had to be equal to or lower than 1.0×10^{-10} eV and 1.0×10^{-10} eV/A respectively between successive minimisation steps, *(iii)* the duration of the minimisation which was limited to 100,000 iterations, and *(iv)* the number of force/energy evaluations which was set to a maximum of 1,000,000. These criteria were specified in this order using the `minimize` keyword.

In both graphene systems, minimisation was completed before reaching the maximum number of iterations with the stopping criterion always being the energy tolerance. This meant that each respective minimisation process was quick to converge to a local potential energy minimum. The per-atom energy for

[5] This choice of algorithm was deemed to be a reasonable one since it is sometimes argued that a full, rather than short, minimisation would have been unnecessary and likely to slow down the subsequent equilibration step.

both systems at the end of the minimisation was -7.43 eV and -7.42 eV, respectively. It is important to highlight that, although the minimisations managed to successfully replicate the C–C bond lengths in graphene as measured experimentally, the intrinsic ripples characteristic of the graphene lattice were absent and instead, the structures appeared completely flat. This outcome was to be expected since minimisations were performed at the equivalent of 0 K i.e. they ignored energy contributions from temperature which are known to be the cause of ripples (Fasolino *et al.*, 2007).

3.2.3.2 | Equilibration protocol

The minimised structures were each initialised to a temperature of 300 K, followed by the application of a Langevin thermostat as proposed by Schneider and Stoll (1978) in an NVT MD simulation, and an NPT MD simulation.[6] Some important definitions:

(i) **Initialisation** refers to an assignment of random velocities to each atom in the system such that the assigned velocities are commensurate to a Gaussian distribution at a given temperature, which in this validation study was 300 K.

(ii) During simulation with an **NVT ensemble**, the composition (N, representing the number of atoms), volume (V) and temperature (T) remain constant, which is ideal for achieving temperature equilibration.

(iii) During simulation with an **NPT ensemble**, the composition (N, representing the number of atoms), pressure (P) and temperature (T) remain constant, which is ideal for achieving simultaneous pressure and temperature equilibration.

[6] In contrast to an energy minimisation step, equilibration via MD simulation involves sampling the equilibrium ensemble. In statistical thermodynamics, the 'equilibrium' is defined by an ensemble of states, and although the low-energy states are more likely to be represented in the ensemble, high-energy states still have a non-zero probability of being sampled.

NVT was performed to mitigate against wide fluctuations in temperature prior to barostatting and to accelerate the attainment of thermal equilibrium. While it was possible to simply initialise the system at 300 K and proceed immediately to NPT barostatting with a Nosé-Hoover, skipping the prior NVT stage is not recommended since large swings in temperature (and pressure as the two are related) may cause the structure to tear itself apart. In the NVT MD simulations (and subsequent NPT simulations), the equations of motion were integrated using the velocity Verlet algorithm with a timestep of 0.5 fs. Similar settings were implemented by Grima *et al.* (2015) for modelling graphene-like systems. While simulations with timesteps longer than 0.5 fs benefit from a shorter running time, preliminary tests conducted on the pristine graphene systems indicated that implementing a timestep of 1 fs would have produced erroneous results. Once again, periodic boundary conditions were applied in the in-plane directions such that the structures resembled an "infinite" graphene sheet positioned in the xz-plane. Conversely, a non-periodic "shrink wrapped" boundary was applied in the out-of-plane y-direction which permitted an adequate representation of a single graphene sheet suspended in space (vacuum) without any restrictions or constraints in the out-of-plane direction. The default neighbour cutoff of 0.1Å was used. Neighbour lists were allowed to be built at each timestep, although an actual build only occurred whenever some atom moved more than half the skin distance i.e. 0.05Å, since the previous build.

During the equilibration stage, time integration was performed on Nosé-Hoover type, non-Hamiltonian equations of motion which derive from the work of Shinoda *et al.* (2004) who combined the hydrostatic equations of Martyna *et al.* (1994) with the strain energy as formulated by Parrinello and Rahman (1981). This essentially permitted computations of the atomic positions and velocities sampled from the NVT ensembles to be effected. Thermodynamic information about the modelled systems was stored as 100-timestep averages, such that each monitored parameter was represented by a single value over a period of 0.05 ps. Temperature was regulated by applying the default

Nosé-Hoover thermostat as implemented in the LAMMPS program to the translational degrees of freedom of the modelled systems with a time constant of 0.05 ps.

For the NPT simulation, the `fix npt` command was invoked which set up a Nosé-Hoover thermostat and barostat according to the specified preferences, including: *(i)* a target temperature of 300 K; *(ii)* a target pressure of 0 GPa for the pressure components in the x- and z- dimension; *(iii)* a time constant of 0.5 ps for the barostat. The temperature control settings were the same as those previously described for the NVT simulation. The box dimension along the y-direction was allowed to fluctuate freely in response to the barostatting action.

The NVT simulation was performed for a maximum of 500 ps i.e. 1,000,000 timesteps, or until each of the following criteria were met:

(i) A change in the total energy of the system which is less than 1×10^{-4} eV between two successive 5 ps-sampled averages,

(ii) A change in the system temperature which is less than 1×10^{-3} K between two successive 5 ps-sampled averages, and

(iii) The system temperature was within ± 2 K of the 300 K target temperature.

In these particular NVT simulations, the above criteria were always achieved prior to the 500 ps-mark, as indicated in Figure 3.3.

Apart from having the same termination criteria of NVT simulations, the NPT simulations also had an additional pressure-related criteria: a change in the system pressure in each of the x- and z-component which needed to be less than 0.01 GPa between two successive 5 ps-sampled averages.

As summarised graphically in Figure 3.4, the NPT simulations were successful in equilibrating the systems under consideration. From a visual representation of the systems themselves (see Appendix D for related video content), it is evident that the modelled structures were sufficiently large as to exhibit the characteristic rippling effect of monolayer graphene. It is important to note that in order for

the rippled form to be observed, the LAMMPS' `fix momentum` command need not be enforced in the y-direction since this would hinder the displacement of the atoms in this dimension.

It may thus be concluded that this protocol was suitable for proceeding to the final step in the designed simulation protocol which was the uniaxial stretching.

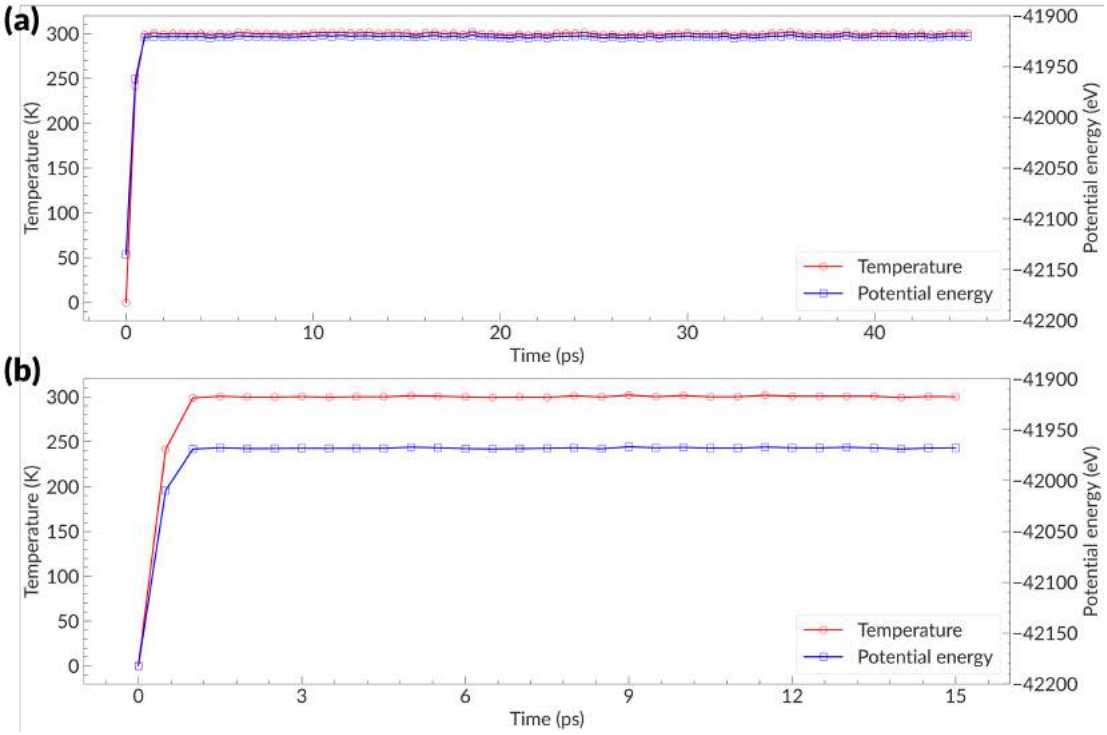

Figure 3.3: Variation in temperature during the NVT equilibration stage of **(a)** pristine zigzag graphene and **(b)** pristine armchair graphene.

3.2.4 | Uniaxial stretching protocol

The final part of the protocol involved simulations of uniaxial stretching along the x-direction with an engineering strain rate, `erate` of 0.005 ps^{-1}. The simulation box dimension L changed linearly with time t based on the equation:

$$L(t) = L_0(1 + \texttt{erate} * t) \tag{3.15}$$

where L_0 corresponded to the initial box dimension value. The LAMMPS command that configured this constant strain rate deformation was:

```
12    fix 2 all deform 1 x erate {erate} units box remap x
```

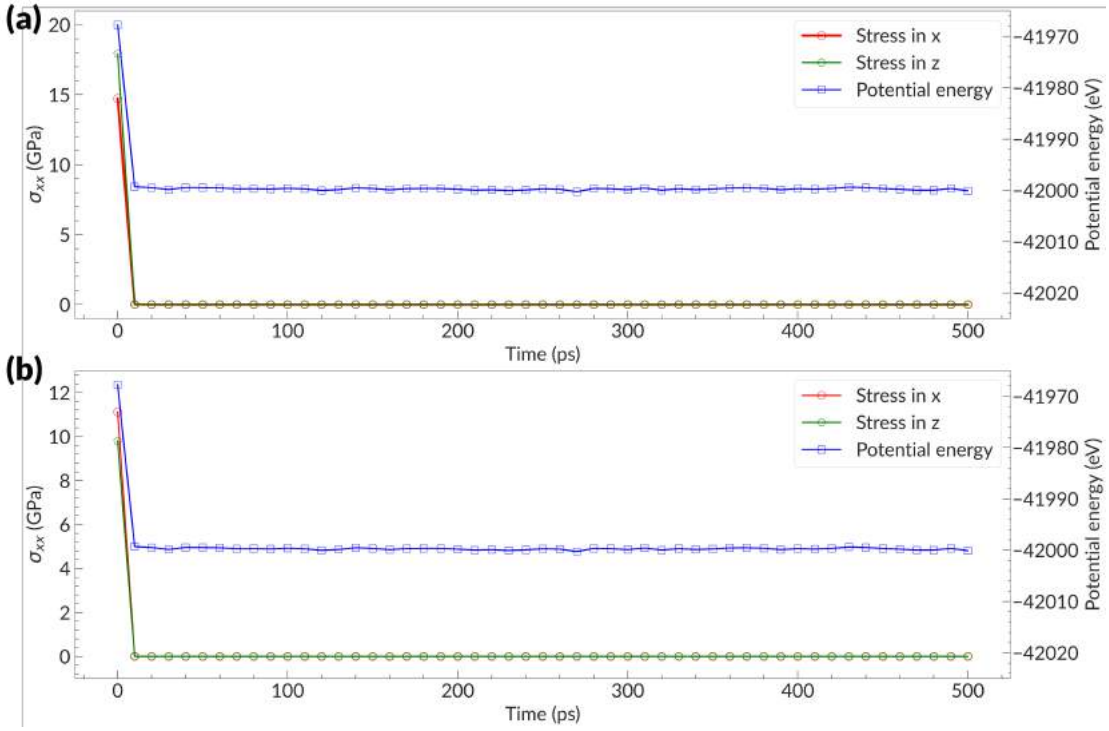

Figure 3.4: Variation in stress along the x- and z-direction and temperature during the NPT equilibration stage of **(a)** pristine zigzag graphene and **(b)** pristine armchair graphene.

A strain rate of 0.005 ps^{-1} meant that at each simulation step, the x-dimension increased by $(0.5\%\ ps^{-1} \times 0.0005ps) = 0.00025\%$.

Periodic boundary conditions were maintained in the x- and z-direction. Likewise, "shrink-wrapping" was retained for the y-direction. NPT conditions were enforced on the the z dimension at a target pressure of 0 Pa so that it could dynamically respond to the orthogonal tensile strain. A similar implementation for the y dimesion was unnecessary since it was "shrink-wrapped". Note that, had the deformation simulations been performed using NVT, this would have resulted in the physically undesirable outcome of holding the two box lengths constant as one dimension of the box was expanded – in other words, this would have forced an unrealistic zero Poisson's ratio.

The stress calculations that were periodically made by LAMMPS during the stretching action, as instructed by the input script (see Appendix B), permitted a

characterisation of the mechanical response of the pristine graphene systems to uniaxial tension.

The post-processing stage involved the collection of pertinent data from the dump files that were generated by LAMMPS during the MD simulations. This necessitated the use of custom written Python scripts which, combined with the API from Ovito Pro software version 3.4.4, automated much of the data treatment processes that were involved in this stage (see Appendix B).

3.3 | Results and discussion

Plots showing the effects of the stretching action on various mechanical properties of pristine graphene are presented in Figures 3.5, 3.6, 3.7, and 3.8. Several comparisons are drawn mainly between these results and those derived from similar published theoretical work (Grima *et al.*, 2015; Zhao *et al.*, 2009) to show that the simulations were truly successful.

The first comparison is drawn betwenn the stress-strain curve for the armchair- and zigzag-directed tensile loading of pristine graphene (Figure 3.5) and a similar plot reproduced from (Zhao *et al.*, 2009) which also modelled pristine graphene at 300 K using with AIREBO potential (Figure 3.9). Values for the Young's modulus in the zigzag and armchair graphene were obtained from the gradient of the respective stress-strain curve in the linear elastic regime within the limit of zero strain[7] and corresponded to 858 GPa for the former and 941 GPa for the latter. A pertinent observation is that the measured Young's modulus along the armchair direction matches the published data quite well, as noted in Table 3.1.

The behaviour of the Young's modulus at very low strains i.e. below 1%, reflected the crumpled nature of the suspended graphene sheet. Since the resting structure of graphene is rippled, the material initially does not resist

[7]For the purpose of reporting the Young's modulus in the zigzag and armchair direction, only data points below the strain value of 0.025 were considered.

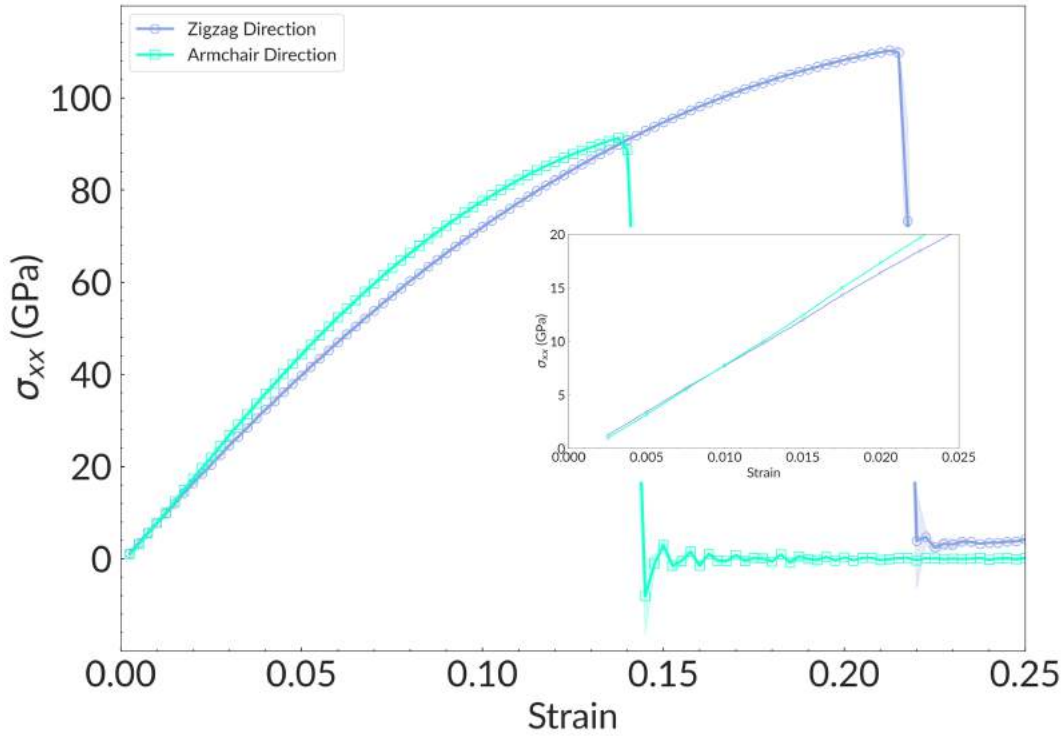

Figure 3.5: Stress as a function of strain, recorded for armchair and zigzag graphene until fracture. The lighter shaded areas show the standard deviation of the plotted data with the widest bounds being registered at the fracture point of the modelled systems. The inset figure depicts the stress-strain relationship in the limit of zero strain.

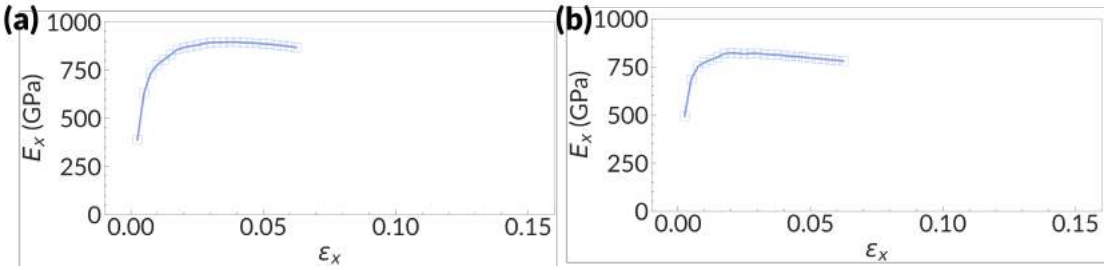

Figure 3.6: The effect of strain on the Young's modulus of **(a)** armchair graphene and **(b)** zigzag graphene in the x-direction. Each datapoint represents a 0.05 ps time weighted average over ten samples.

deformation. This explains why as stretching commenced, the Young's modulus was at a relatively low value and gradually increased as the ripples in graphene flattened out (Figure 3.6). In fact, it was found to increase from a theoretical value of 0 GPa up to a maximum of 822 GPa for the pristine zigzag graphene and GPa for the pristine armchair graphene. At the maximum recorded Young's modulus, the sheet was observed to be completely flat. Following this peak

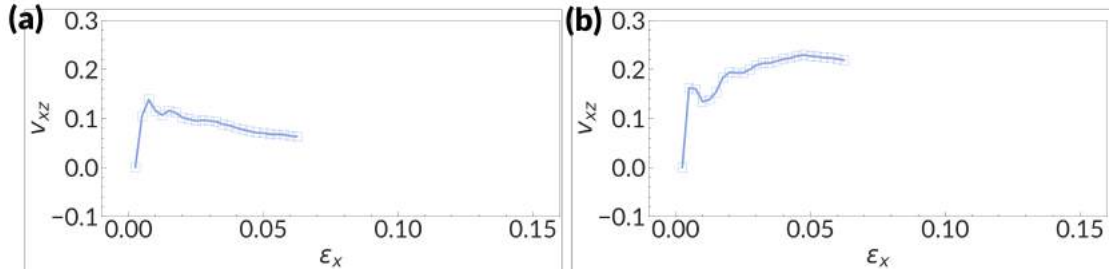

Figure 3.7: The effect of strain on the Poisson's ratio of **(a)** armchair graphene and **(b)** zigzag graphene in the x-direction. Each datapoint represents a 0.05 ps time weighted average over ten samples.

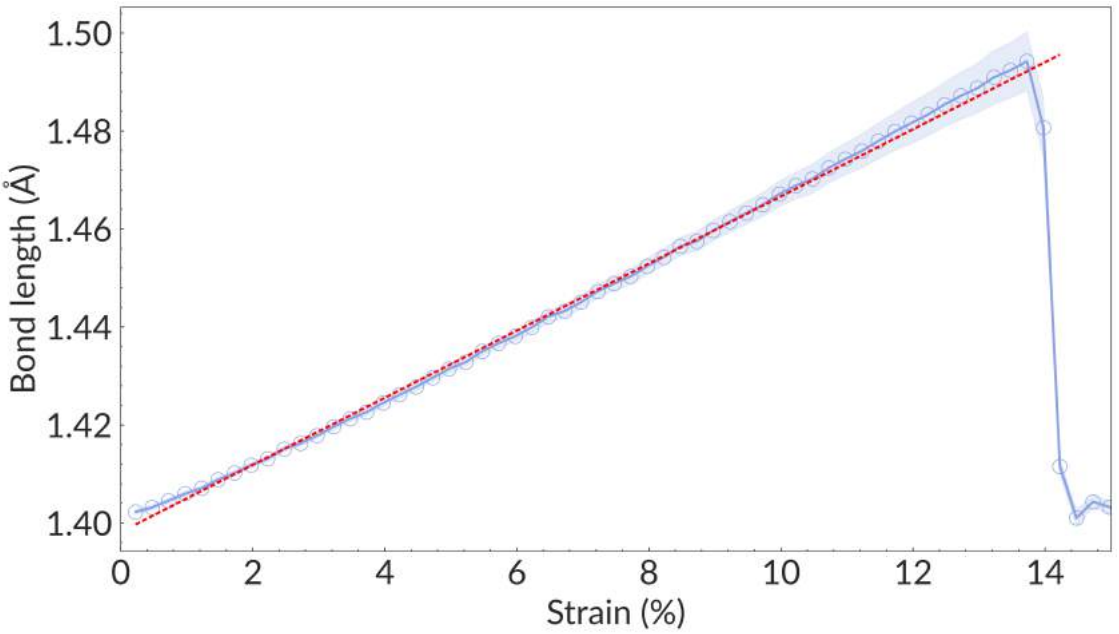

Figure 3.8: Variation in the average C–C bond length of armchair graphene. The linear portion of the plot i.e. the pre-fracture region, was fitted with a line (marked in red) having the equation $y = 0.0069x + 1.40$.

which corresponded to a flattened graphene stucture, a re-lowering of the Young's modulus ensued. Similar observations were also made by Grima *et al.* (2015) for the response of the Young's modulus in graphene to increasing strain, although their maximum attained value for this property was higher, at *c.* 950 GPa (see Figure 3.10). A likely explanation for this apparent discrepancy it that the choice of sampling interval used was different. At such low values of strain, choosing a relatively low sampling interval tends to introduce more

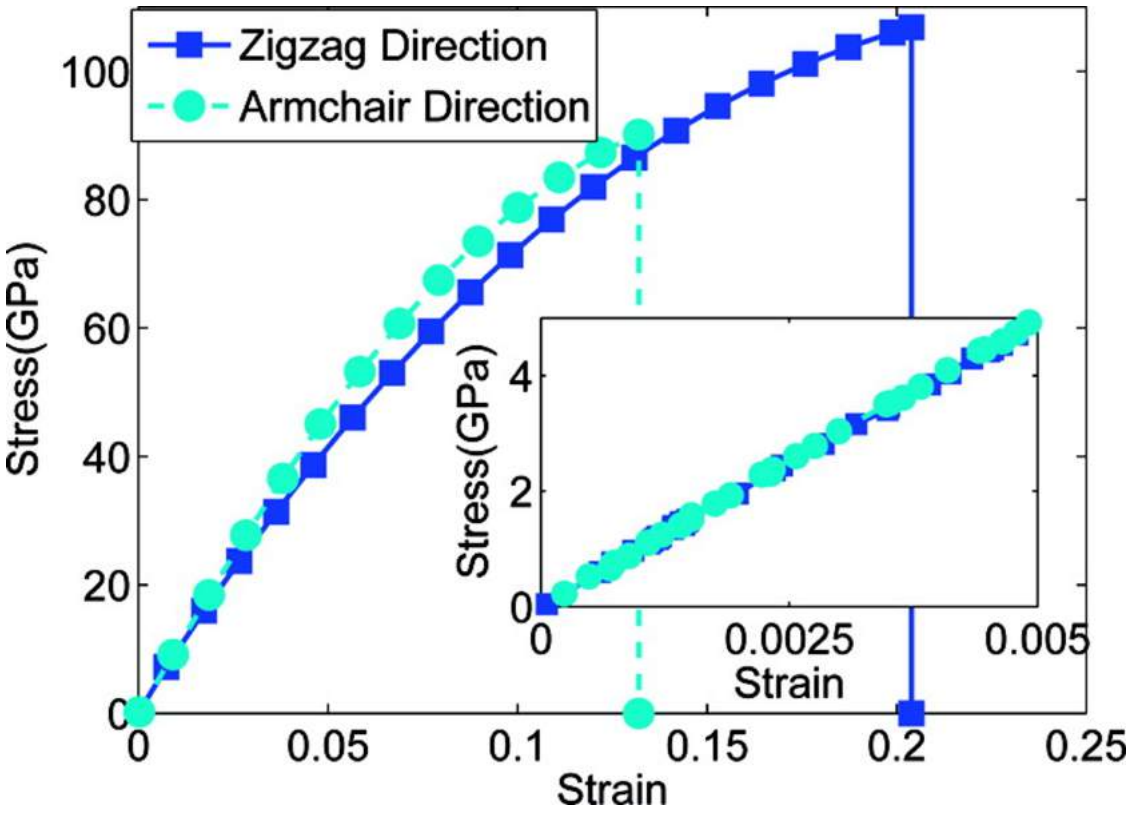

Figure 3.9: The variation of stress in graphene subjected to uniaxial stretching along the armchair and zigzag direction at 300 K, as reported by Zhao *et al.* (2009). The inset figure depicts the linear elastic behaviour in the limit of zero strain.

fluctuations in the obtained result, which concurrently raises the maximum possible value and lowers the minimum possible value.

Figure 3.7 depicts the effect of strain on the Poisson's ratio of graphene in the armchair and zigzag directions, respectively. Although these plots do not reproduce the same exact outcome as the one reported by Grima *et al.* (2015) (see Figure 3.11), the general trend of the plot specific to armchair graphene is comparable to the published one. As before, the choice of a lower sampling interval may be the likely cause for this discrepancy.

The analysis of the C–C bond length, which was performed solely for armchair graphene and summarised in Figure 3.8, was also as expected, in the sense that the initial C–C bond length prior to the stretching action averaged 1.40Å, which agrees well with the commonly established value of 1.42Å (Kalosakas *et al.*, 2013). It is worth highlighting that the mean bond length fails to distinguish between

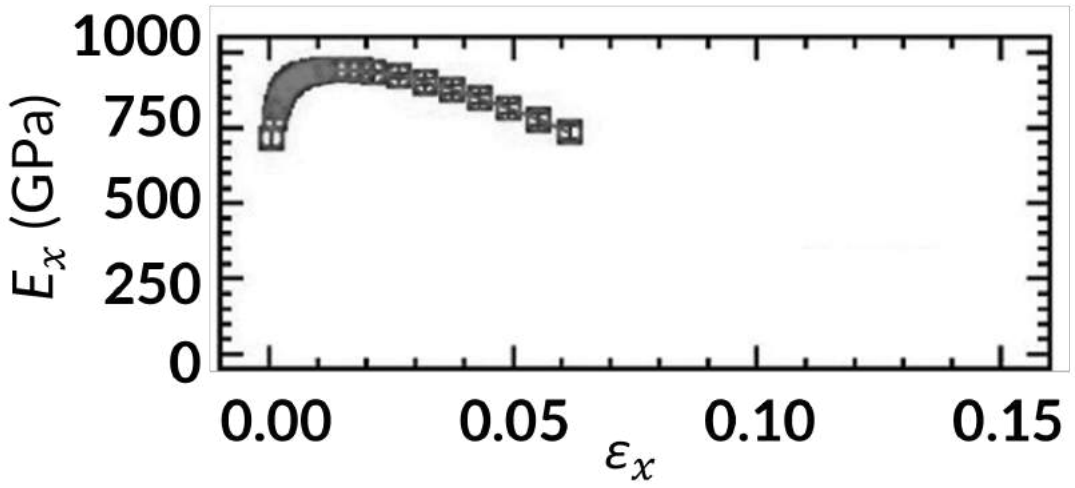

Figure 3.10: The averaged in-plane Young's modulus against the engineering strain for stretching in the x-direction, as reported by Grima *et al.* (2015)

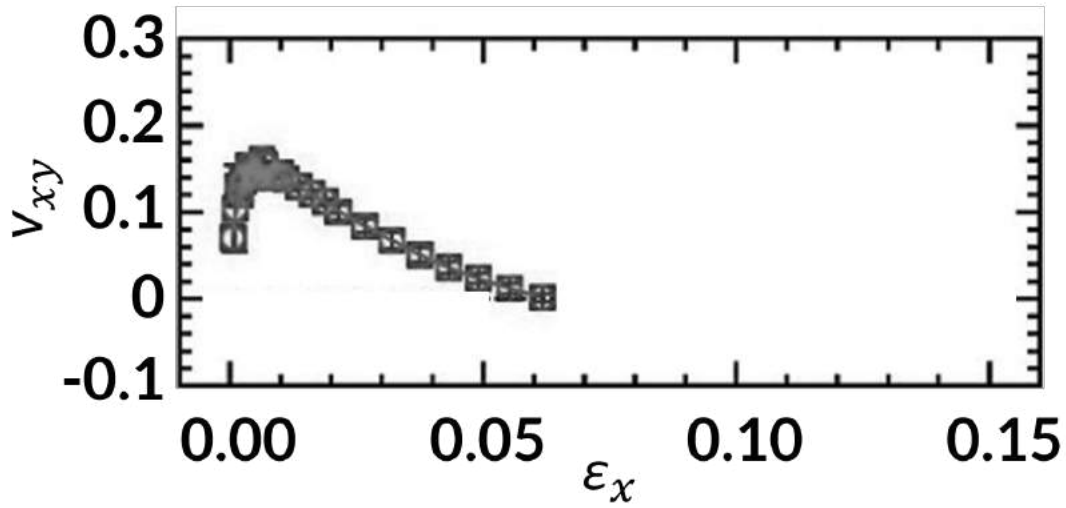

Figure 3.11: The averaged in-plane Poissons's ratio against the engineering strain for stretching in the x-direction, as reported by Grima *et al.* (2015).

the two types of bonds that are present in pristine graphene that are oriented differently within the system and relative to the direction of stretching (Zhao *et al.*, 2009). However, it was beyond the scope of the present work, which is a mere methodology development and validation study, to perform such a detailed analysis which would have required the development of an additional section of the methodology to distinguish between different bonds within the system. Nevertheless, as noted by Figure 3.8, the average bond length of the armchair

graphene system as a function of strain is in close agreement with the average value reported by Kalosakas *et al.* (2013). This adds further confidence to the simulation protocol being adopted here.

3.4 | Conclusion

The aforementioned results clearly show that the protocol as devised was successful in reproducing the reported properties of pristine graphene in vacuum at 300 K. As shall be seen in the next chapter, the use of this validated protocol was also effective towards simulating the uniaxial stretching of a series of folded graphene systems.

4

Modelling the Tension-induced Unfolding of Graphene-type Systems

Chapter Highlights

- A detailed account of the methodology that was followed in order to construct three separate folded graphene models, based on the combined use of VMD and Materials Studio, is presented.
- An outline of the LAMMPS-based procedure (previously validated in Chapter 3) is provided for equilibrating the aforementioned folded systems to 300 K and 0 Pa and for simulating their mechanical properties under uniaxial tension.
- It is shown that folded graphene systems seem to be energetically stable under the studied test conditions and fold in a manner that is somewhat analogous to folding a regular sheet of paper. The same analogy is also used to explain why defective systems fold more densely.
- The uniaxial tensile simulations performed on folded graphenes reveal a number of anomalous properties that are manifested by these systems, including a zero Poisson's ratio and a negative tangent modulus – properties which are adequately explained by analysing the deformation profile.
- General remarks about the strengths and limitations of this study are presented.

4.1 | Introduction

The purpose of this chapter is to report on the undertaking of a simulation-based study regarding the tensile behaviour of previously unstudied

folded graphene conformations, together with a thorough discussion of its outcomes.

Cognisant of the fact that (*i*) graphene can adopt several distinct folded conformations, (*ii*) the mechanical properties of graphene (and folded graphenes by association) display significant anisotropic character (Ni *et al.*, 2010), and (*iii*) line defects are capable of inducing fold formation (Gauci, 2018), a total of three **folded** graphene models, shown in Figure 4.1, were constructed *in silico*, namely:

(a) Folded pristine graphene with the armchair direction oriented along the x-direction;

(b) Folded pristine graphene with the zigzag direction oriented along the x-direction;

(c) Folded graphene with V_1(5-9) mono-vacancies arranged in the form of periodic, parallel lines along the armchair direction and orthogonal to the x-direction.

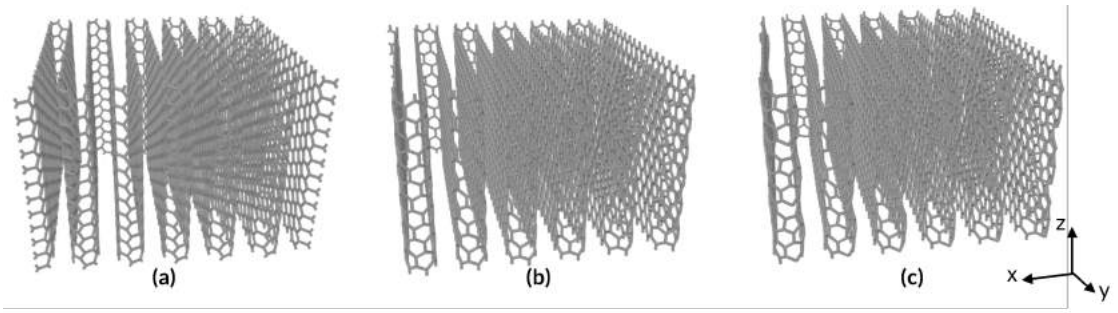

Figure 4.1: A digital rendering of the three folded graphenic systems, namely **(a)** pristine, folded armchair, **(b)** pristine, folded zigzag, and **(c)** defective, folded zigzag graphene (shown here in their unoptimised state) which served as the initial structures for the subsequent MD simulations.

Chapter 3 established that the custom-designed LAMMPS protocol was adequate for simulating the tensile behaviour of pristine graphene (at 300 K and 0 Pa) to a satisfying degree, by producing mechanical results that were congruent with the experimental and simulation-based findings reported elsewhere in the literature. However, in order to apply this protocol *talis qualis* for use with the folded graphenic systems, some important assumptions need to be made.

4.2 | Simulation protocol

Briefly, the methodology used to simulate the tensile behaviour of the folded graphene-type systems in LAMMPS involved the construction of molecular models with manually inserted folded regions through the combined use of VMD and Materials Studio, their optimisation via a conjugate gradient energy minimisation, followed by their equilibration to 300 K and 0 Pa via NVT and NPT simulations, and, finally, NPT dynamics which simulated uniaxial stretching along the x-direction.

4.2.1 | Construction of the folded systems

The pristine folded graphene systems modelled in this chapter, shown in Figure 4.1(a, b), may be described as flat sheets of graphene, aligned in a quasi-parallel manner to each other, that are connected together via folded regions which are not dissimilar to a half CNT configuration. With this in mind, the procedure that was followed for creating each of them entailed the use of VMD to generate portions of nanotubes and graphene sheets which were oriented into an optimal configuration and later combined into a single crystalline system, referred to as the $1 \times 1 \times 1$ system, using Materials Studio. A short geometry optimisation with the Dreiding force-field (available within Materials Studio), was performed on each of these initial structures.

These few-atom systems, containing 144 atoms each, failed to meet the size requirement for the proper execution of MD simulation, considering that the latter necessitates a sufficiently large system to ensure that the Boltzmann-Maxwell speed distribution appropriately represented the temperature of the modelled system. Thus, each system was enlarged to 5184 atoms (a thirty-six-fold increase in system size) by converting a $6 \times 1 \times 6$ unit cell of the base structure into a supercell, as illustrated in Figure 4.2 for the pristine folded armchair graphene. The preferred system size represented the best compromise between the limited

availability of hardware resources to run these simulations and the requirement of having a large enough system.

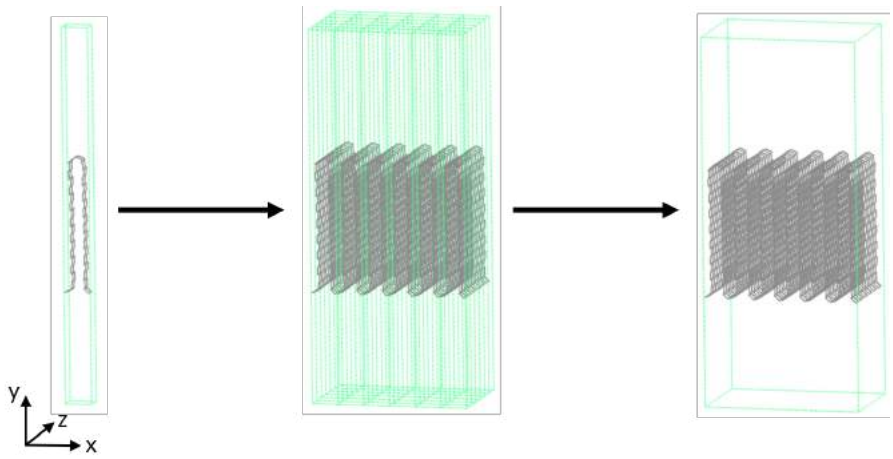

Figure 4.2: A schematic diagram showing the steps involved in the creation of a $6 \times 1 \times 6$ pristine folded armchair graphene supercell. The system on the left shows a $1 \times 1 \times 6$ system while the system on the right shows the $6 \times 1 \times 6$ system, obtained by converting 36 repeat units (shown in the middle) to a single supercell.

A slightly modified procedure to the one described above was adopted for constructing the defective folded graphene system, depicted in Figure 4.1(c). In this case, its unit cell structure i.e. the defective $1 \times 1 \times 1$ system, was formed by the stepwise conversion of a copy of the pristine $1 \times 1 \times 1$ folded zigzag system into a $1 \times 1 \times 2$ superlattice and the manual removal of two single-vacancy defects of the (5-9) type from the rounded nanotube segment of the structure, which produced a system containing $2 \times 144 - 2 = 286$ atoms. The remainder of the construction process for the defective folded zigzag system, which has been summarised schematically in Figure 4.3, was analogous to the one that was followed for creating the pristine systems: the $1 \times 1 \times 1$ system was "cleaned" using a short geometry optimisation with the Dreiding force-field within Materials Studio, and then, it was enlarged $\times 6$ in a and $\times 3$ in c to produce a $6 \times 1 \times 3$ system with 5148 atoms in total.

It must be emphasised that the lattice defects of the defective system were placed in an orderly manner such that the enlarged system displayed, according to the nomenclature proposed by Grima *et al.* (2018), a $(m, n) = (1, 6)$ defect

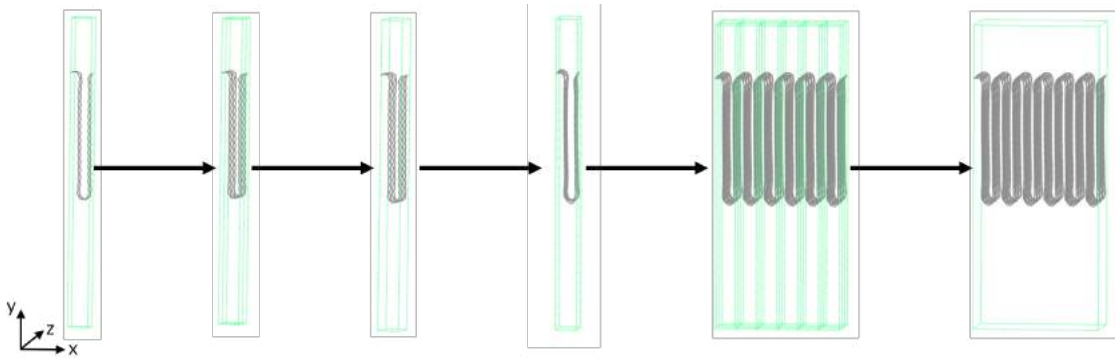

Figure 4.3: A schematic diagram of the creation process for the $6 \times 1 \times 3$ defective folded zigzag graphene supercell. From left to right: $1 \times 1 \times 1$ pristine folded zigzag graphene, a $1 \times 1 \times 1$ pristine folded zigzag graphene with two repeat units in the z-direction, a $1 \times 1 \times 2$ folded zigzag graphene supercell, a $1 \times 1 \times 1$ defective folded zigzag graphene, a $1 \times 1 \times 1$ defective folded zigzag graphene with six repeat units in the x-direction and three in the z-direction, $6 \times 1 \times 3$ defective folded zigzag graphene supercell.

pattern wherein the separation between each successive defect was $3(n-1) = 15$ hexagonal carbon rings along the x-direction $(n = 6)$ and the minimum allowable separation along the z-direction $(m = 1)$, as illustrated in Figure 4.4.

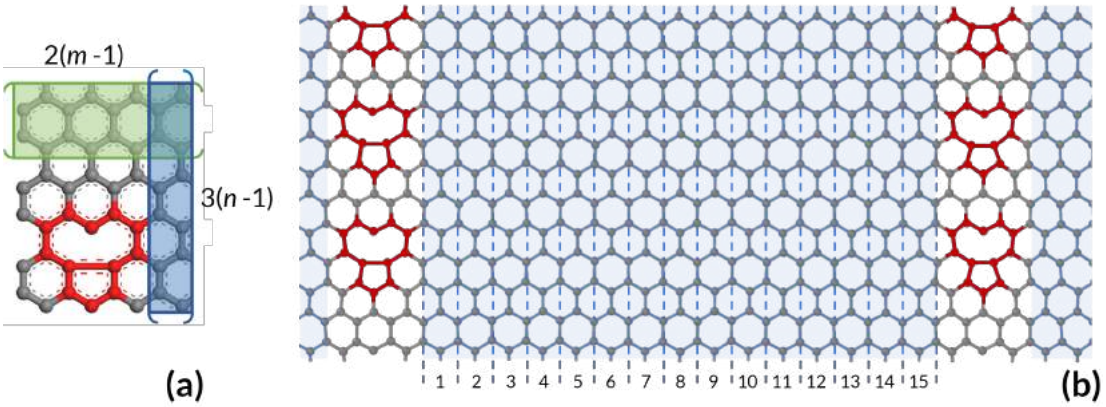

Figure 4.4: The spatial arrangement of V_1(5-9) mono-vacancies (highlighted in red) within defective folded zigzag graphene. **(a)** The unit cell of defective folded graphene having a single vacancy defect located at $[3x(n-1), 2x(m-1)]$ where m,n = (1,6) and x corresponded to the separation from the origin i.e. the bottom-left corner of the sheet, in terms of the unit cell count **(b)** A flat section of the same system with several repeated units.

A common feature to all three folded systems was their general pleated structure, having graphite-like portions that always lied in the yz-plane such that the "ripple effect" propagated in the x-direction. Therefore, if at this stage

the systems had been fully stretched open, the so-called "armchair system" would have had its armchair direction aligned with the x-direction (and the zigzag direction along the z-direction), whereas in both the pristine and defective "zigzag systems", the zigzag direction would have corresponded to the x-direction (and the armchair direction to the z-direction), as illustrated in Figure 4.5.

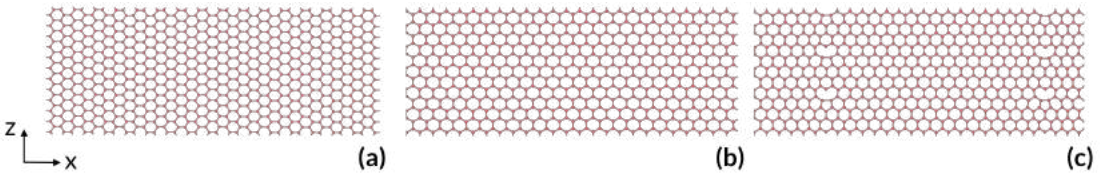

Figure 4.5: A visual representation of the distinct characteristics present in the folded graphenic systems that are described in this chapter, namely **(a)** the armchair and **(b)** zigzag pattern of the folded pristine systems, and **(c)** the defect line pattern displayed by the folded defective zigzag system.

Structure files of the folded graphene systems described herein were generated through VMD in accordance with the data file formatting guidelines contained within the LAMMPS documentation (Plimpton *et al.*, 2021). For additional information about these files, refer to Appendix B.

4.2.2 | Assumptions made

A number of assumptions had to be made in relation to the uniaxial tensile simulations of the folded graphenic systems and their subsequent analysis:

1. The termination criteria as defined by the equilibration protocol were assumed to be stringent enough to ensure that, by the end of the equilibration stage, the structural instability (and associated energy fluctuations) caused by the artificially inserted folded regions in the modelled systems had completely subsided.

2. The deformation rate was sufficiently low for the modelled systems not require a re-equilibration step prior to each incremental strain, as reported by Grima *et al.* (2015).

3. The thickness of the folded graphenic systems for the purposes of stress calculation was assumed to be the same used for pristine graphene i.e. 3.354 Å, which value corresponds to the interlayer separation of graphite (Greenwood and Earnshaw, 2012). The rationale behind this decision was based on the fact that, if the same set of simulations had been replicated experimentally, stress would have been applied equally to the transverse edges of the folded graphenes which would have had a monoatomic thickness.

4.2.3 | Minimisation and equilibration of the folded systems

The systems constructed as described in the previous section, as realistic as they may seem, cannot be considered truly representative of what one would expect to observe had the systems been studied at 300 K under near-ambient pressure conditions. Such realistic representations were obtained by employing the validated protocol for the energy minimisation and equilibration procedures with one minor adaptation: a preliminary system optimisation in Materials Studio using the Forcite module with parameters from the PCFF force-field. This step was necessary to remove any spatial overlap between atoms in the modelled systems which, if left unmitigated, would have resulted in the failure of the simulations. In view of the fact that the PCFF potential has been used successfully in related work on graphene (Grima *et al.*, 2015), no additional re-validation was required. Following this preliminary optimisation, a conjugate gradient minimisation was performed for a maximum of 100,000 outer iterations and a maximum allowed per-atom displacement of 0.1 Å between each successive

iteration. This was followed by a set of NVT and NPT simulations[1] which were programmed to run for a combined simulation time of 1 ns. By the end, an optimised version for each of the three folded graphenic systems in their unstretched state was obtained (see Appendix D).

4.2.4 | Uniaxial stretching of the folded systems

Briefly, the protocol implemented for the uniaxial stretching of the folded graphenic conformations entailed the application of a constant strain rate in the x-direction i.e. the orthogonal direction of the folding lines, until the system was fully extended at *circa* 900% strain. More specifically, the rate at which strain was applied was 0.5% ps^{-1} i.e. (0.5% ps^{-1} $\times$ 0.0005 ps) = 0.00025% per 0.0005 ps simulation step. Periodic boundary conditions were retained in the x- and z-direction and, likewise, the y-direction remained "shrink-wrapped". Systems were simulated under NPT to ensure that they responded to the applied strain in a physically realistic manner, as discussed in detail in the previous chapter.

4.3 | Results and discussion

4.3.1 | Analysis of the equilibrated folded systems

Animations[2] (see Appendix D) and representative images from these animations illustrating the unstretched conformations of the three systems modelled are depicted in Figure 4.6. These images, produced from well-equilibrated MD simulations, can therefore be treated as valid exemplars of energetically stable structures for the systems at the simulation temperature and

[1] Refer to Chapter 3 for an in-depth account of exactly how this step was implemented.

[2] The output of MD simulations is a dynamic representation, rather than a static one, where the atomic positions are presented as a function of time. Such output is best presented as an animation.

pressure.[3] These images present the structures from different viewpoints to facilitate the three-dimensional interpretation of the systems.

From these images and animations, it may be deduced that the high-density folded conformations as modelled in this work seem to be energetically stable. This added stability may be explained by the fact that the folded systems benefit from extended stabilising $\pi - \pi$ interactions (Hunter, 1993). This underscores the propensity of such systems to form multi-layered graphenic regions as a way to gain energetic stability. It is evident from Table 4.1 that, while the studied systems are of similar energy content, the density is significantly different, with a 25% gap between the least dense (folded pristine zigzag graphene) and the most dense (folded defective zigzag graphene) system.

Here it must be mentioned that for this stability due to graphite-like interaction to be imparted, it is imperative that folds with a small radius of curvature form, so as to permit the systems curves/folds on itself where the adjacent layers mimic graphitic systems (i.e. separations in the region of 3-4 Å). Obviously, curvature comes at a cost: its existence permits regions of multi-layer graphene, which are stable, but the fold itself puts the system under local strain.

More importantly, the simulations suggest that the presence or otherwise of the defects has an effect on the manner of curvature at the folding regions. Indeed, it is evident from Figure 4.6 that the average radius of curvature in the folds contained within the folded pristine graphenes is larger than that for the sharper folds that are present within the defective graphene system. A tentative explanation for this behaviour may be found in the relative ease with which the defective graphenic system could fold as opposed to its pristine counterparts. As noted elsewhere (Grima *et al.*, 2018), the presence of adjacent pentagons and

[3]It must be emphasised that at non-zero Kelvin conditions, molecular systems should not be considered as static structures and thus no single image can capture the dynamic behaviour of the systems. This also applies for the polymeric systems studies here and any image presented in this dissertation should be considered as a representative snapshot of a dynamic system. Such dynamic information is better representable through the animations which are presented in the Supplementary Information.

		Folded pristine armchair graphene	Folded pristine zigzag graphene	Folded defective zigzag graphene
Unit cell parameters (Å)	*a*	43.94	44.19	47.76
	b	43.70	55.56	40.63
	c	29.08	25.13	25.14
Unit cell density (gcm^{-3})		1.85	1.68	2.10
Per-atom potential energy ($kJmol^{-1}$) following...	Conjugate gradient minimisation	-716	-717	-714
	NVT equilibration at 300K	-713	-713	-710
	NPT equilibration at 300K and 0Pa	-713	-713	-710

Table 4.1: The unit cell parameters of the three folded systems modelled in this work and their potential energies at key stages prior to the uniaxial stretching simulations.

hexagons which characterise the V_1(5-9) defects tend to force the graphene to adopt a locally curved conformation to permit the co-existence of side-sharing pentagons and hexagons. This favours out-of-plane bending at the lines where the defects are present, with the net result being that the graphene sheet attained very prominent and distinctive fold lines which were not dissimilar to what one observes at the macroscale when folding a sheet of paper. As evident in Figure 4.7(a), a pre-folded, accordian-like sheet of paper can be compressed rather easily to a flat form with the crease lines acting like hinges. In contrast, when such fold lines are absent, the paper seems to prefer retaining a substantial radius of curvature as evident in Figure 4.7(b). This suggests that what is being observed here is more of a mechanical phenomenon, which is independent of scale, to the extent that it is manifested both at the nanoscale by the graphene systems modelled here and at the macroscale.

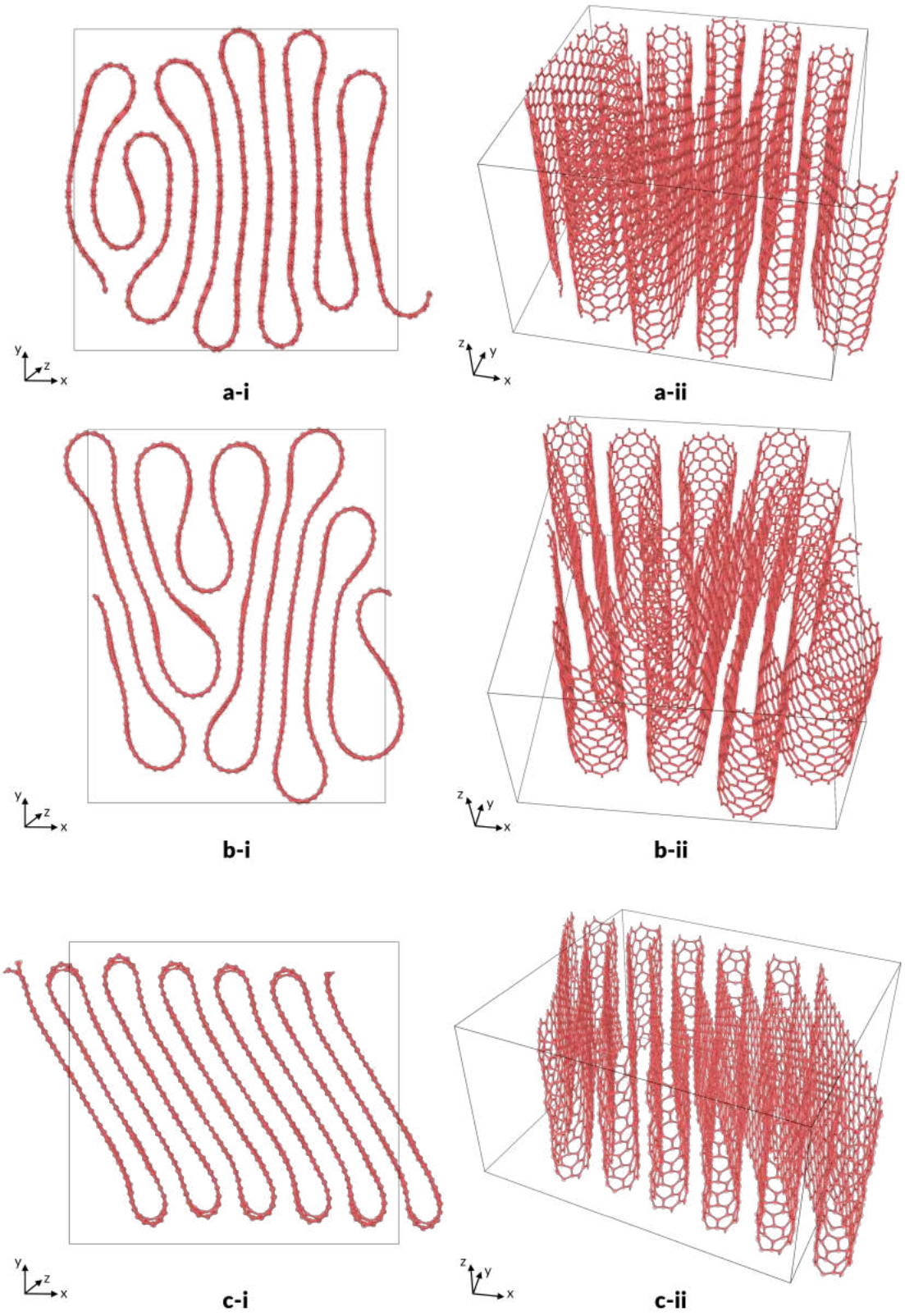

Figure 4.6: Snapshots from different perspectives of **(a)** pristine, folded armchair, **(b)** pristine, folded zigzag, and **(c)** defective, folded zigzag graphene upon completion of the equilibration stage.

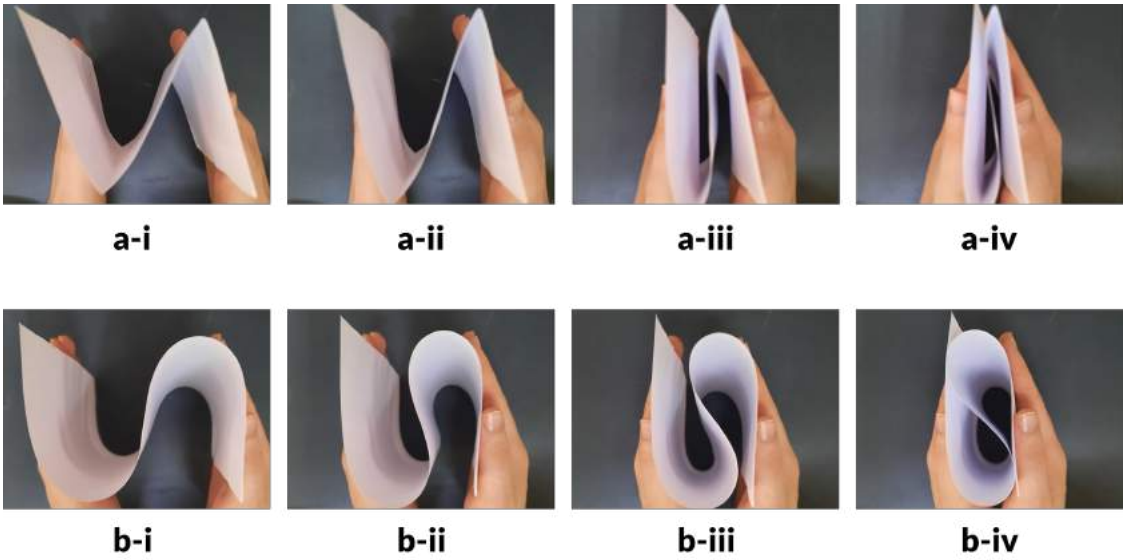

Figure 4.7: A macroscale folded paper model to explain the different folding regime of the pristine and defective folded graphene systems modelled in this work. **a** Folding of a pre-creased sheet of paper, in an analogy to the folded graphene system with patterned defect lines. **b** Folding of a normal sheet of paper, in an analogy to the pristine folded graphene systems.

This macroscale analogy with a folded paper is also useful to explain another phenomenon, namely that in the case of the defective system, the folds always correspond to the defect lines whilst in the non-defective systems, the folds are more mobile. This effect can be very easily demonstrated at the macroscale by comparing the behaviour of an uncreased and a pre-creased paper as they are compressed in a similar way to that shown in Figure 4.7. This hypothesis was proven at the nanoscale through the simulations which suggest that in the case of the defective systems, the folds were **always** restricted to the line of defects with the result that the system can be considered to be constrained to a specific "quasi periodic" highly ordered morphology. In contrast, the folds in the non-defective systems seem more mobile with the result that their locations within the system is less predictable and the folds are not all alike, as illustrated in Figure 4.6. This difference stems from the fact that in the non-defective systems, if one had to ignore the stabilisation that is derived from the graphite-like $\pi - \pi$ interactions, the energy that is required for the fold to form is the same irrespective of where the fold forms. On the other hand, in the case of the defective system, the folds

are more prone to form at the location of the V_1(5-9) defects due to Euclidean geometry constraints imposed by presence of pentagonal and hexagonal rings which force the system to adopt a non-planar conformation. This key difference between defective and non-defective systems also seems to be the fundamental cause of the different stress-strain properties, as discussed below.

The replication of the nanoscale phenomenon at the macroscale has another important implication, namely, that what is being reported here is an effect of structure and not of chemical composition. This suggests that the behaviour being manifested here is likely to occur irrespective and independently of the cause of the fold (which, in this case, are the V_1(5-9) defects) and only based on whether a fold line is present. Thus, for instance, a similar effect would be expected to occur if single-side hydrogenation was used to create the imperfections leading to the fold line (Ho *et al.*, 2020).

An important difference between the macroscale paper model and nanoscale is that whilst at the nanoscale there is a drive to bring closer together portions of graphene sheet due to the attractive nature of $\pi - \pi$ interactions, there is no natural driving force to fold a paper. Thus, even in the absence of folding lines, a randomly formed fold may still occur in graphene in an attempt to maximise the non-bonding interactions while limiting the stresses at the folding region by a larger radius of curvature.

An interesting observation which can be made at this point is that, throughout the equilibration period, the random folds within the pristine graphene systems, once they formed, retained their conformation to a remarkable degree. A possible explanation to this is the difference in stability gained once a particular folded conformation is adopted by the system, which acts as a barrier towards an even lower minimum. Therefore, one could expect that at a higher operating temperature, the system could be less prone to getting "stuck" into a single conformation and be able to transition to ones of lower energy content.

To discuss this aspect further from a quantitative perspective, one may look into the studies on single-walled carbon nanotubes. It is well known that such

carbon nanotubes may exist in a wide range of diamteters, but there seems to be a physical limitation on how narrow such tubes can exist in. Present knowledge suggests that the thinnest free-standing nanotubes have diameters of *c.* 4.3 Å (Torres-Dias *et al.*, 2017), which nanotubes are thought to be either $(5,1)$ or $(4,2)$ tubes (Hayashi *et al.*, 2003). This dimension is very similar to the diameter of the curved folding region of the defective systems studied here, as illustrated in Figure 4.8. Note that, apart from the free-standing nanotubes, other small tubes are also known to exist inside other tubes, all of which have *c.* 4 Å diameter, as discussed by Zhao *et al.* (2004) who used aberration-corrected high-resolution transmission electron microscopy to study these systems. This lower practical limit on the dimensions of the curved regions may explain the non-perfectly circular shape of the curved region, as well as the actual separation between the layers: an attempt to accomodate the optimal diameter of the nanotube-like curved region (which should ideally exceed 4 Å, the minimum diameter of stable nanotubes) with the optimal separation of the graphite-like flat surface (graphite separation being typically 3.35 Å(Torres-Dias *et al.*, 2017)).

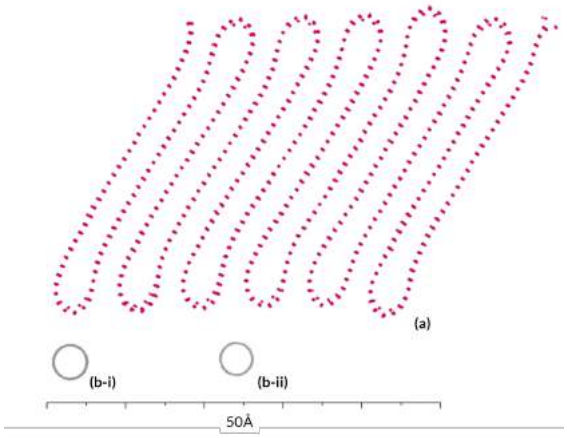

Figure 4.8: A visual comparison between the profile of **(a)** the folded zigzag graphene conformation with V_1(5-9) line defects, and those of **(b-i)** (5,1) CNT and **(b-ii)** (4,2) CNT.

4.3.2 | The stretching behaviour and the stress-strain properties

The stress-strain properties of the three systems modelled are reported through animations (see Appendix D) and through the plots and images shown in Figures 4.9, 4.10, and 4.11. From these results, two important findings can be inferred:

- Folded graphenes can sustain very large strains while the in-plane thickness remained almost constant, i.e. $\nu_{xz} \approx 0$, or a zero in-plane Poisson's ratio;
- There were various instances where the stress vs. strain graph had a negative gradient, indicating instances of an instantaneous negative tangent modulus.

Focusing on the manner of deformation of the three systems studied,[4] starting with the **folded pristine armchair** system, it should be noted that two dominant patterns of unfolding were identified. The first consisted in the re-adjustment of neighbouring folded regions by sliding against each other, whilst the second necessitated the opening of a fold. This served to partially release the stress accumulated as a direct result of the stretching action.

An important observation that should be made is that, if one were to analyse the plot of the **energy** vs. strain in Figure 4.9 (which is also proportional to simulation time), it would swiftly be apparent that each time a fold opened up and "snapped", it sent ripples across the whole system and caused an abrupt decrease in the total potential energy. Regarding the latter point, the potential energy that was gained by the system during the stretching process was partly released at each fold opening ("snap"), and in some cases, there was even a release of additional pre-stored energy within the molecule i.e. instances when

[4]To facilitate the discussion and interpretation of the outcomes from the unfolding processes, reference is made to particular conformations by the "Conformation number" as denoted in Figures 4.9, 4.10, and 4.11

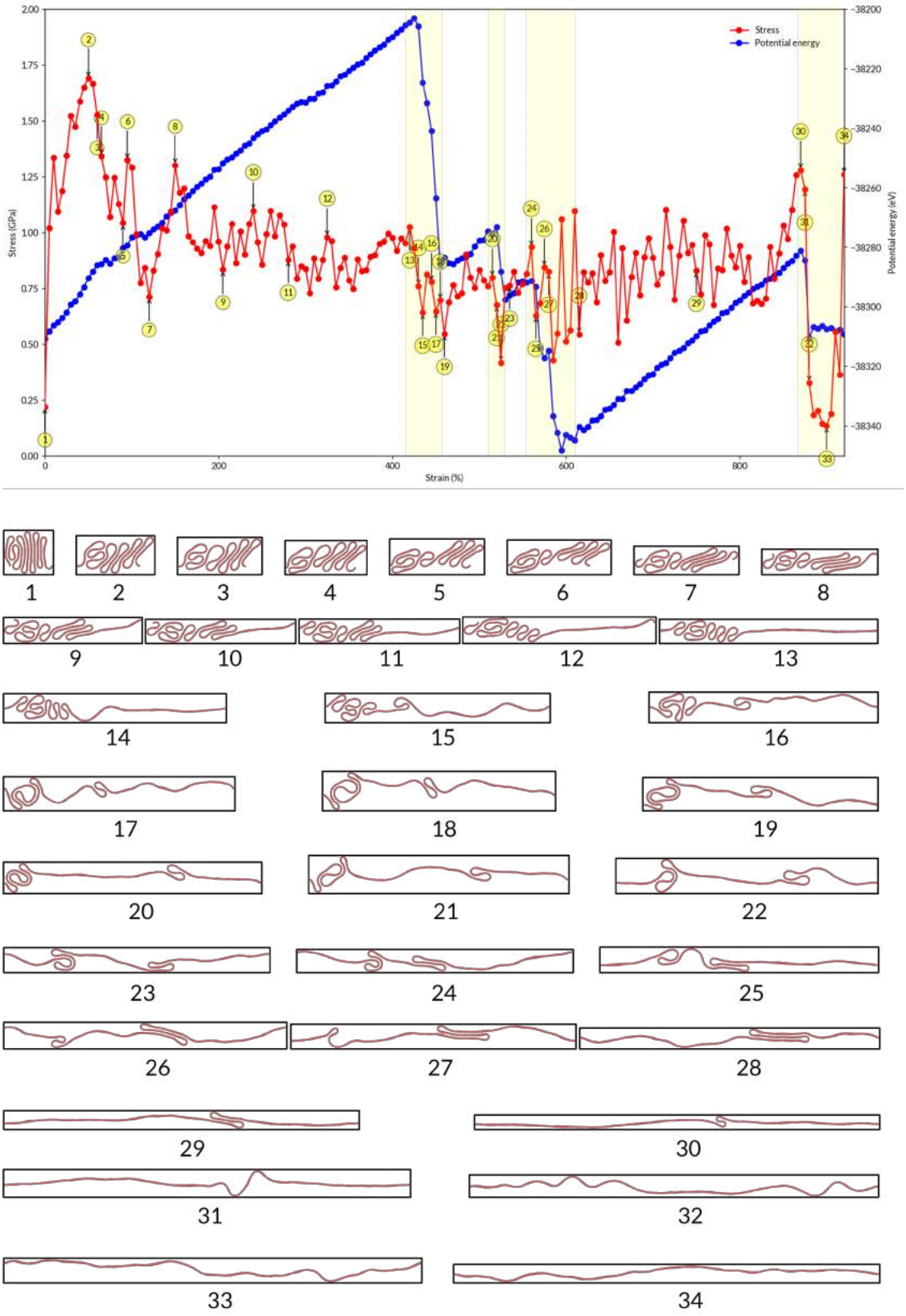

Figure 4.9: Variation of stress (GPa) and potential energy (eV) with strain (%) during the unfolding process of folded, pristine armchair graphene, highlighting key conformations. Yellow-shaded regions mark the periods when fold openings occurred.

the total potential energy at a particular strain value was lower than the starting potential energy. This effect was mirrored to a lesser extent in the magnitude of the **stress** component in the x-direction σ_{xx}; while a "snap" did lower the stress component, the difference was similar to those induced by the sliding action of the graphene layers. Nevertheless, one should note that there were several instances during the stretching simulation where the system had a **negative tangent modulus**, as indicated by the gradient of the stress vs. strain plot which was negative multiple times. In practical terms, this meant that the material, as it was being pulled open from both sides, had instances of **"push back" behaviour**. Moreover, from the same stress-strain plot in Figure 4.9, it is also evident that the system had a low modulus, almost two orders of magnitude lower than that typically quoted for standard graphene. An explanation for this is that the presence of folds obviously offered a much easier pathway for the system to deform as, in an analogy to a macroscale folded paper model, it is much easier to unfold a folded paper than to actually stretch paper. In fact, had there not been the attractive $\pi - \pi$ interactions, the decrease in modulus could have been even more pronounced. In other words, the folds offer pathways for the system to alleviate stress gained through uniaxial stretching. If it were not for them, σ_{xx} would have increased linearly to approximately 90 GPa and cause the systems to rapture, as observed in standard graphene.

Looking more closely into the deformation itself, the initial (and highest) peak of 1.7 GPa for σ_{xx}, marked as Conformation 2 in Figure 4.9, may be attributed to resistance manifested by the system in trying to retain its graphene layers as close together as possible. Interestingly, this was accompanied by tilting which raised the value of the stress component to then be partly relieved from Conformation 2 to 5 through sliding action. Such a cyclic exchange persisted until Conformation 14 when the first fold opening occurred, at a corresponding strain of 420%. This was closely followed by three other fold openings, from Conformations 15 to 17. Fold openings were often preceded by a re-orientation of the folds such that the plane of the bilayer region became orthogonal to the stretching direction; this was

clearly the case in regard to the structural changes observed from Conformation 20 and 21 which led to a fold opening at Conformation 22. Conformation 26 marks the first time when the potential energy of the system dipped below the value recorded for the initial structure. A possible explanation to this occurrence may be the formation of a trilayer structural domain within the system. From then onwards, sliding action due to the increasing strain led to a shortening of this trilayer (and a consequent increase in energy due to the decreasing contribution of Coulomb forces). When σ_{xx} reached 1.3 GPa at Conformation 30, the last remaining folds in the system opened up, causing a major drop in σ_{xx}.

Focusing now on the **folded pristine zigzag** system, similar observations can be made in respect of the energy and stress profiles even if there are some very recognisable differences in the actual deformation profile. It is beyond the scope of this work to fully compare and contrast the two deformation profiles since such an analysis is not trivial and should preferably be made after analysing a number of repeats of these simulations as well as additional simulations where the honeycomb systems are studied as a purely mechanical structure (e.g. using finite element analysis, the standard simulation technique for structures).

From Figure 4.10, it may be observed that the first fold opening at Conformation 7 occurred at a significantly earlier strain value (*c.* 130%) than that in the folded armchair graphene. This was closely followed by two other fold openings at Conformations 9 and 10 which, viewed together, seem to permit better layering of the graphene folds. By Conformation 12, this essentially led to a multi-layered, graphite-like structure, which happened to correspond to the lowest point in potential energy, even lower than the starting structure. From then onwards until the fourth fold opening at Conformation 15, folds began to move apart whilst σ_{xx} stayed relatively constant at an average value of 0.92 $\pm$ 0.08 GPa. This trend, however, was reversed throughout the remainder of the unfolding process, as evidenced by the approaching of the folded domains from Conformations 17 to 19 which facilitated further fold openings.

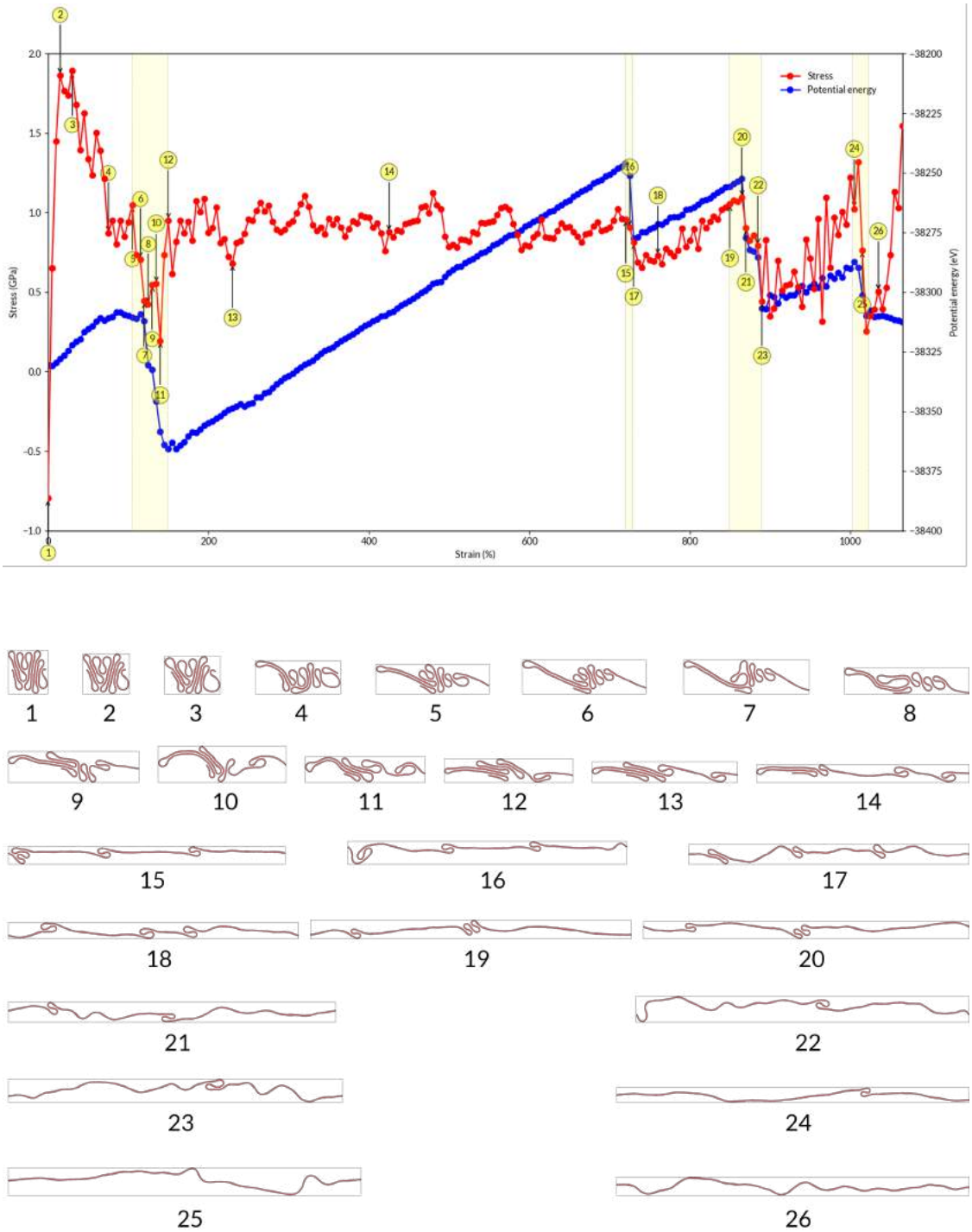

Figure 4.10: Variation of stress (GPa) and potential energy (eV) with strain (%) during the unfolding process of folded, pristine zigzag graphene, highlighting key conformations. Yellow-shaded regions mark the periods when fold openings occurred.

Finally, looking at the **folded defective zigzag** system, the regions of negative tangent modulus (instantaneous "pull-back" action) which correspond to instances of a fold opening are more pronounced than in the pristine folded graphene systems. This is probably due to the much better packing and attractive interactions which is geometrically favoured through the presence of the defects.

The deformation itself contrasts in some aspects from that of the pristine systems and may be casually described as involving a clearly demarked sequential unfolding whereby the folds unfold separately, one by one. This is not the case for the non-defective systems, where the folds seem to move around the system with increasing strain. In other words, the deformation is a sequence of repeatable events where folds "unfold" and "snap". Thus, the properties may be inferred just by focusing on one such event, illustrated in Figure 4.11, which while representing only a section of the process, manages to capture the entirety of it and can therefore be used to describe the behaviour that was noticed. For the sake of completeness, a more extensive set of images is also reported (Figure 4.12), which follows the deformation from 0% strain to *circa* 1000%. A similar pattern emerged in the σ_{xx} and potential energy plots. Thus, Figure 4.11(b), while representing only a section of the process, can be assumed to capture the entirety of the simulation.

Analysing this single event, similar to what was observed in the other two systems, the initial build-up of σ_{xx} can be attributed to the reluctance of the graphite-like portions to separate from each other. This event led to the situation in which the v-shaped segment (preferring that form because of the defect line), was straightened, at which point, one of the fold decoupled from its neighbour and began to slide, ultimately forming a 'hook', which subsequently 'snapped' under additional strain. Interestingly, the 'hook' itself also resisted further opening, resulting into a second (albeit much lower) maximum σ_{xx} prior to its opening. It is worth noting that σ_{xx} was reduced through the sliding action of its graphite-like portions and fold openings, with the latter being always preceded

by the former. On average, fold openings resulted in a more pronounced decrease in σ_{xx} than the sliding movements (approximately 30%).

It is worth noting that the base structure comprised of a smaller-sized 1,6-system like the one described here has been studied by Gauci (2018) through a series of minimisations using the PCFF force-field with the scope of identifying novel, stable conformations (all of which contained folded domains). With this work in mind, the first observation that should be made is that the present simulation results do not contradict the finding of this earlier preliminary study performed using the PCFF force-field. In particular, transient folded structures observed during the simulated unfolding of this system in the present study were analogous to those reported by Gauci (2018) (see Figure 4.13)(a). For example, Gauci (2018) notes that the principal result from this study was that, as the system unwinds and assumes a less dense, v-shaped conformation, the potential energy increases due to the loss of the stabilising graphite-like portions. This was indeed the case in the present study, however, the difference in energy between the two conformations was less pronounced. This agreement is extremely important, particularly in view of the fact that the previous study was performed using a different force-field from the AIREBO used here as it confirms that the results being obtained are not likely to be a mere artefact of the force-field used.

An interesting observation made during post-processing with Ovito was that the total number of bonds in the system decreased. Bonds were created by the program at a uniform cut-off radius of 2Å. This decrease can be interpreted as bond breaking at the defect sites which transitioned from V_1(5-9) to V_1(12), as illustrated in Figure 4.14. It should be noted that during the final stage of the deformation, when the structure was fully opened but not yet fully stretched, the remainder of the V_1(5-9) defects transitioned to ones of the V_1(12) type. This kind of nanostructural damage will need to be researched further in order to establish how it affects the mechanical robustness of the system, and also properly assess to which extent the system may be subjected to cyclic loading.

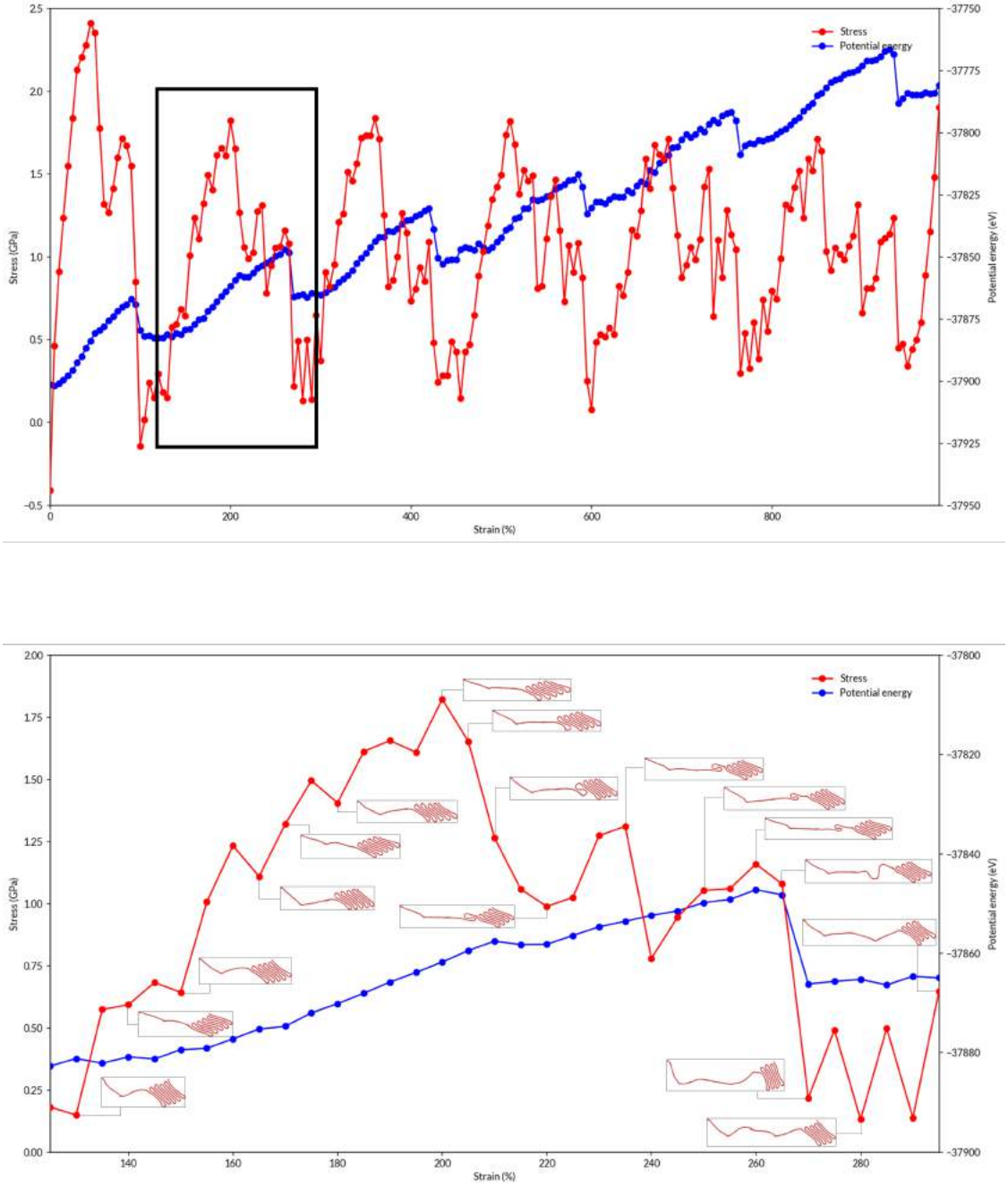

Figure 4.11: *Top*: The unfolding process of folded zigzag graphene with V_1(5-9) line defects in terms of the variation of stress (GPa) and potential energy (eV) with strain (%). *Bottom*: An enlarged portion of the top plot (enclosed in a black rectangle), highlighting some key conformations.

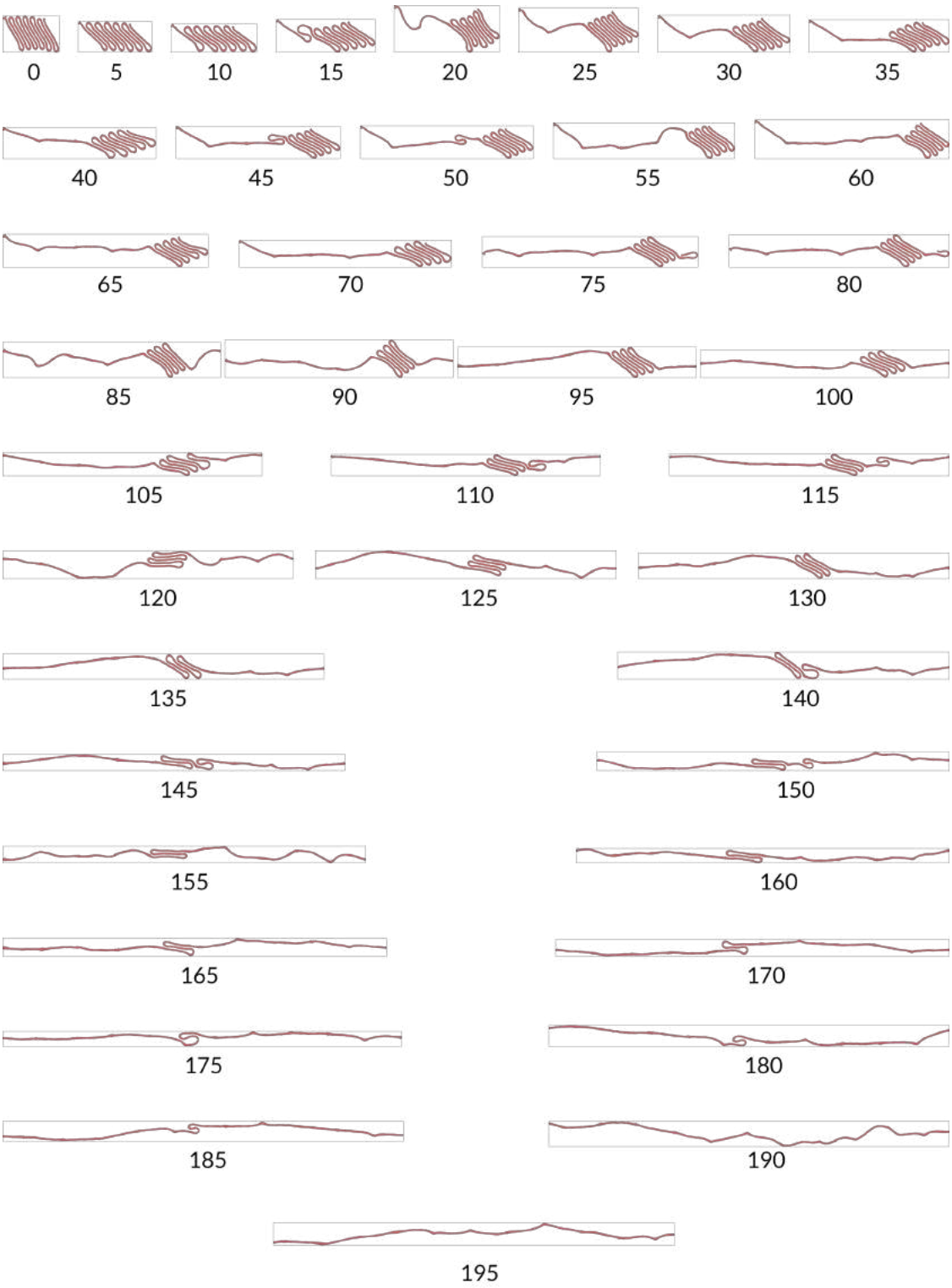

Figure 4.12: Snapshots from the uniaxial tensile simulation of defective zigzag graphene taken every 10 ps $\times$ 5 = 50 ps.

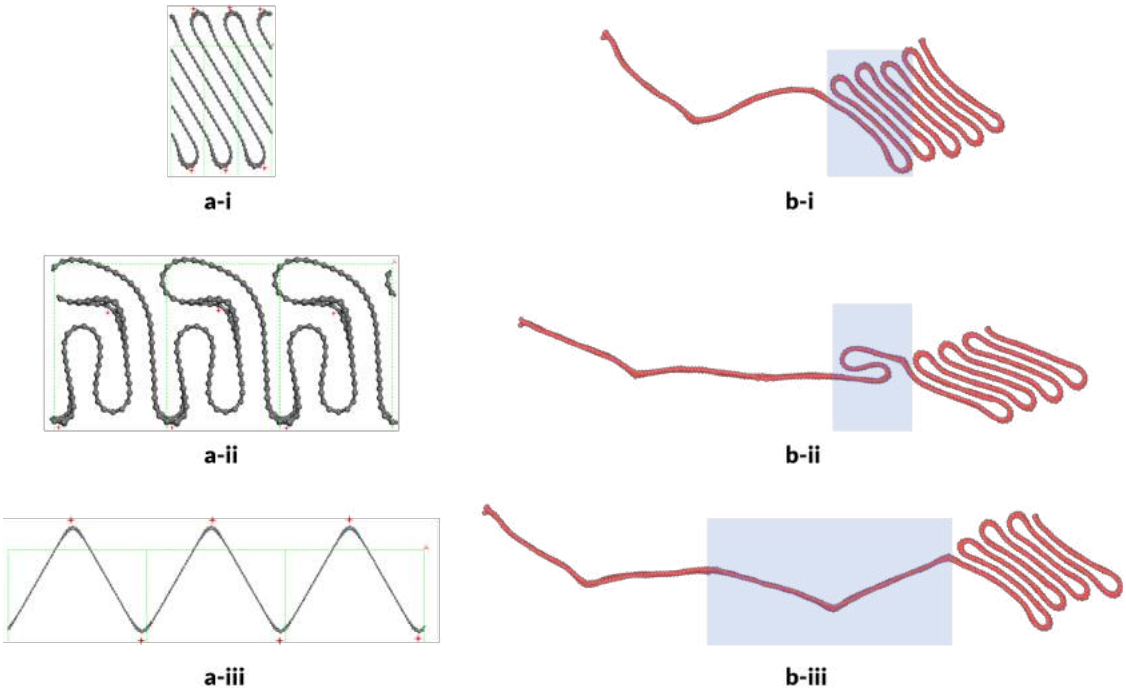

Figure 4.13: Ball-and-stick representations of folded graphene conformations presented as $1 \times 3 \times 1$ superlattices. **(a)** Transient structural domains (highlighted in blue) observed during the unfolding process of the folded zigzag graphene system with patterned V_1(5-9) defects. **(b)** Matching folded graphene systems which were identified by Gauci (2018) using a static approach comprised of a series of energy minimisations. The location of each defect site is marked in red.

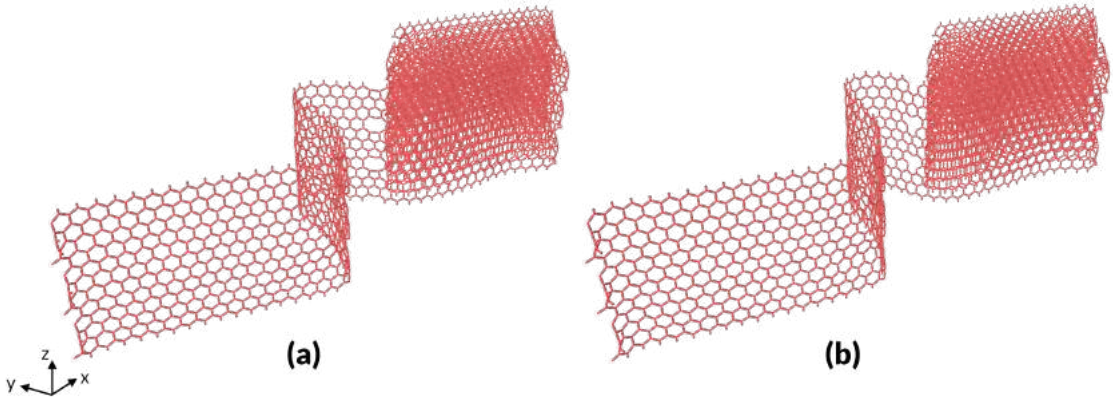

Figure 4.14: Snapshots of the defective folded zigzag graphene with two visible defect sites. **(a)** Two vacancy defects of the V_1(5-9) type at 180% strain. **(b)** Two V_1(12) defects which appeared when the system was strained to 190%.

4.3.3 | Strengths and limitations

Before concluding, it is important to highlight some of the strengths and limitations of this work. The first strength which ought to be highlighted is that, through modelling, it was possible to explore the structure and properties of folded conformations of graphene which were previously not studied, and predict some very interesting and anomalous properties, including negative tangent modulus and a zero Poisson's ratio (Figure 4.15).

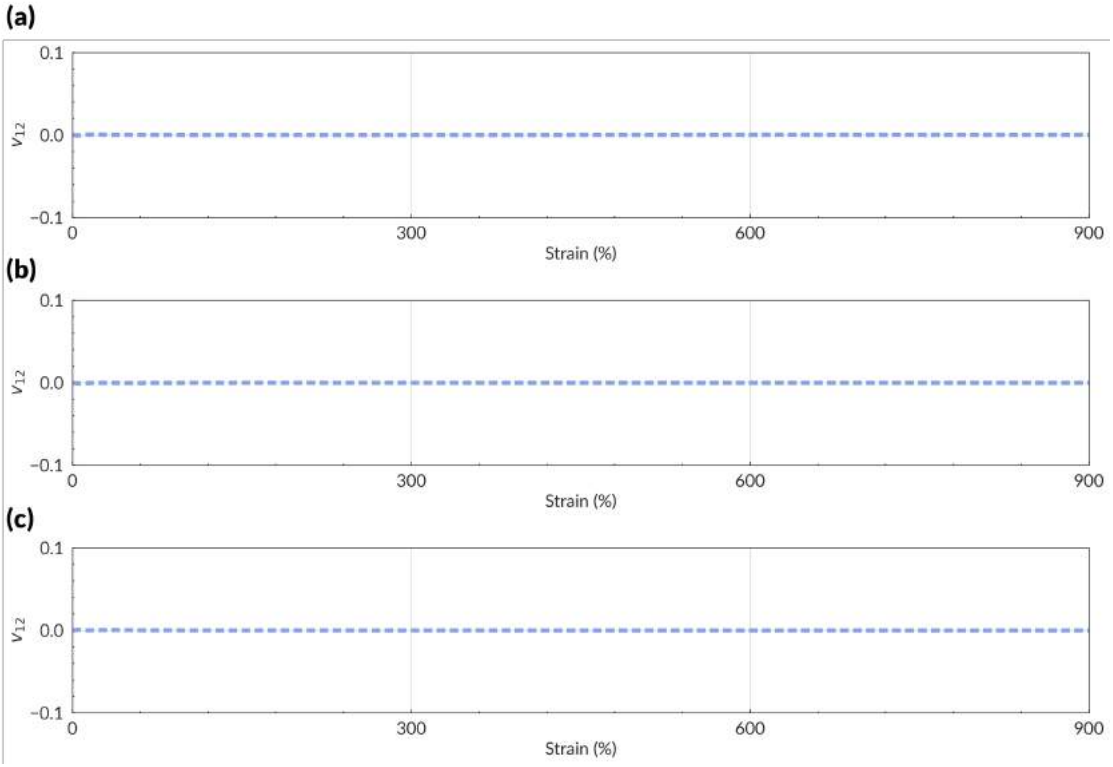

Figure 4.15: Variation in the on-axis Poisson's ratio with strain (%) during the unfolding process of **(a)** the pristine folded armchair graphene, **(b)** the pristine folded zigzag graphene, and **(c)** the defective folded zigzag graphene.

The software used was open-source and available to the scientific community at zero cost. Thus, the results-to-cost ratio of this work was very high, and forms the basis for additional studies to expand what was identified here. More specifically, for the first time, it was shown how graphene can be made even more versatile and exhibit anomalous stiffness properties through the use of folds. The

concept that a polymeric system can attain properties through the manner how the macromolecule folds on itself is not something new to graphene. Suffice to mention how the chemistry and properties of proteins is heavily dependent on the tertiary structure of the polymer, where the tertiary structure is dictated by the presence of entities which may interact via non-bonded interactions, particularly hydrogen bonding. In this case, the "tertiary structure" of graphene is imparted by the $\pi - \pi$ interactions which, like H-bonding, are non-bonded interactions of a substantial magnitude. Moreover, a distinction between folded forms of graphene and standard, planar graphene is not normally made since the presence of folds in graphene does not constitute a formal and distinct allotrope of carbon from the non-folded conformations.

Nevertheless, the fact that the work was entirely based on modelling had its own inherent limitations. For instance, no direct experimental proof has been obtained which definitely confirms the properties being reported here. In this respect, it is reassuring that the results obtained here were not dissimilar or contradictory to earlier, more preliminary results obtained using the commercially available software Materials Studio with the PCFF force-field (Gauci, 2018).

A further limitation is that the study was limited to stretching uniaxially perpendicularly to the fold lines. Ideally, additional simulations ought to be carried out to fully characterise these materials by simulating off-axis moduli and Poisson's ratio as well as the shear moduli. Comparing the system to earlier work on corrugated sheets exhibiting negative Poisson's ratio off-axis Grima *et al.* (2018), it could well be that even the present systems are auxetic for loading off-axis. Unfortunately, such a conclusion cannot be reached from the present study without performing additional simulations.

Another limitation which should be mentioned concerns the estimation of margins of confidence in the reported values. As with any other work where measurements are being reported, care must be taken to recognise that there is always some level of uncertainly in any result. In this regard, one should note that, for instance, according to the 10-ps-averaged data samples for the

unfolding process of the defective zigzag system, instances when σ_{xx} turned slightly negative could well fall within such margin of error. This is somewhat confirmed by plots whose inputs originated from the same data source but processed using a different sampling average each time. (Figure 4.16). Had the occurrence of negative σ_{xx} been a real phenomenon, this would have indicated an appreciable reluctance by the system to being further deformed by the applied strain. Nevertheless, it is more likely that this was merely an artefact of the simulation protocol used, or maybe due to the relative small size of the system. In view of this, it is worthwhile for such an aspect to be investigated further.

Apart from the aforementioned issue related to 'negative stress', the methodology itself was also characterised by a number of assumptions which could have had significant influence on the results obtained. For example, it is a standard practice in graphene-related modelling studies to approximate the thickness of graphene to the empirical value for the layer separation of graphite i.e. 3.35 nm. It was perfectly justified, therefore, to adopt this assumption throughout the validation study presented in Chapter 2, but to a lesser extent when folded graphenes were involved. Given the fact that the size of the y dimension was shrink-wrapped, that is, continuously adjusted to the exact size occupied by the modelled system in that specific dimension, it would have been possible, through a slight modification of the LAMMPS input script, to dynamically update the size of the y dimension throughout the course of the simulation in order to be included in the stress calculations, rather than assuming that it was constant. Nonetheless, it is reassuring to note that the inclusion of a similar operation would not have interfered with the trends that emerged from the stress plots discussed previously (Figure 4.17).

Another important limitation of this study is that simulations were performed on what could be considered as medium-sized systems with the assumption made that these represent the bulk behaviour of a quasi-infinately large sample. Ideally, the simulations would be repeated several times using progressively

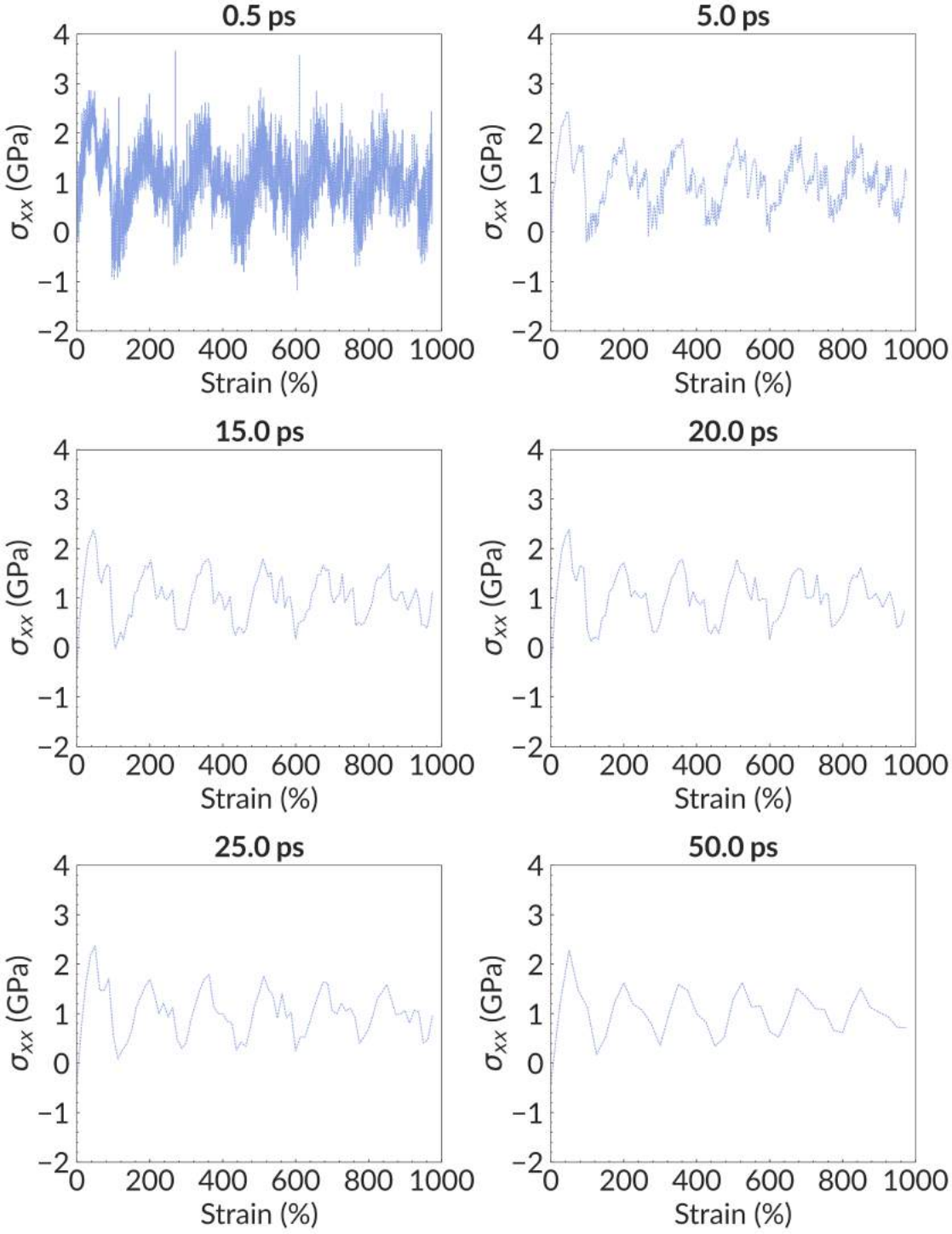

Figure 4.16: Variation in σ_{xx} (GPa) with strain (%) during the unfolding process of the defective zigzag graphene at different sampling averages. Although the data points of every single plot shown here originated from the same LAMMPS-generated output, there are key differences, with the most notable being less fluctuation on moving to progressively larger sampling intervals.

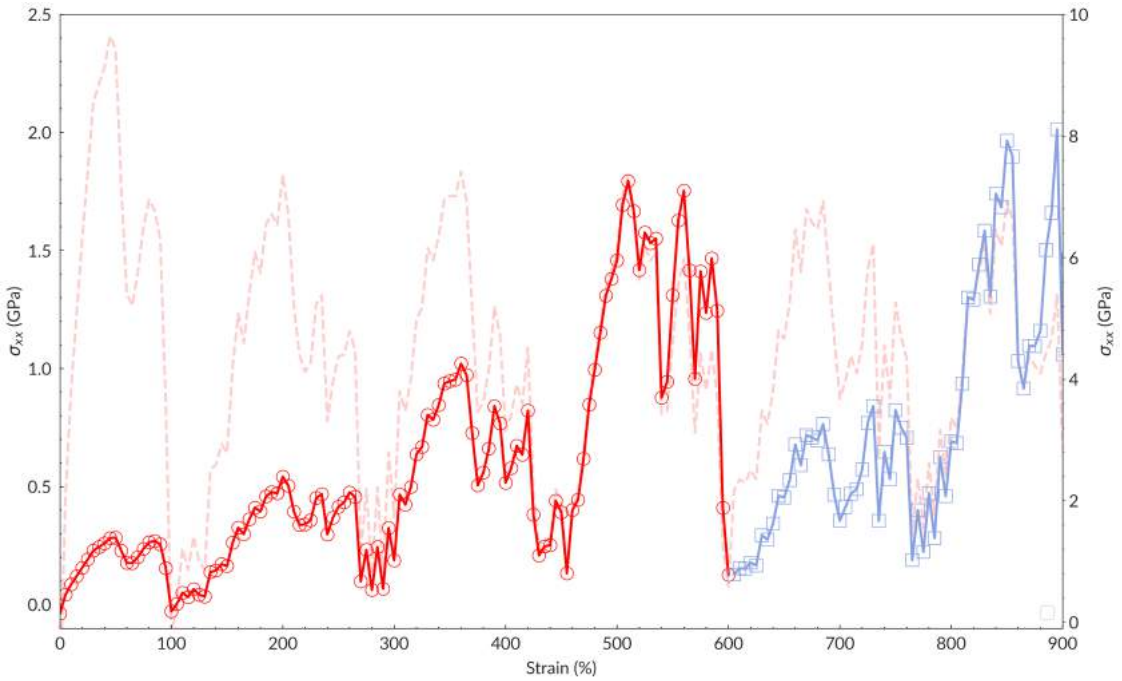

Figure 4.17: How a different treatment of system thickness influences the variation of σ_{xx} throughout the unfolding process of the defective zigzag graphene system. The solid plot lines are derived from a dynamic y dimension, whereas the dotted plot line is derived from stress data which was calculated using a constant graphene thickness of 3.35 Å.

larger units until convergence is guaranteed. Such simulations, however, are not trivial to perform in view of the limited hardware resources, etc.

Probably, an even bigger limitation is that the system was guided in the process of fold formation. Whilst this might not have a major impact in the case of the defective systems since the fold lines are indeed expected to correspond to the defect lines, the same cannot be said with regards to the pristine systems. In the latter systems, it would be appropriate if additional simulations are performed, ideally in a manner where there is minimal user interference to how folds are formed. Such simulations should also be repeated on larger samples since, as evident from Figure 4.6, the "tertiary structure" of the folded pristine graphenes are not "regular". This also highlights another important limitation of this study which is the constraints imposed through the use of periodic boundary conditions. For example, the simulations on the defective system suggest that within a unit cell, folds tend to unfold sequentially (Figure 4.18). This could suggest that, had

a larger system been used with a larger number of folds, the same effect would have been observed. However, due to the fact that periodic boundary conditions are imposed what is truly being simulated here is that a fold per unit cell length is unfolding.

Figure 4.18: The sequential unfolding of defective zigzag graphene through a visualisation of multiple periodic images of the unit cell in the x-direction.

Another limitation related to the previous one concerns a claim made earlier with regard to the pristine graphene systems where it was argued that at higher temperatures than 300 K i.e. the simulation temperature, structural changes would occur more easily and thus, the systems could in theory achieve conformations that exist at lower energy minima. Therefore, it would be worthwhile to substantiate this claim by repeating the same simulation at different temperatures.

Lastly, this study was limited by the use of cut-offs which had to applied to curtail the simulations from taking an excessive amount of time to complete. In practice, it would have been ideal to repeat the simulations with larger cut-offs so as to ensure that the cut-off distance and neighbour skin distance used did not preclude any important interactions. Unfortunately, due to hardware and time limitations, such a verification study could not be performed. Nonetheless, it is reassuring that related studies have applied similar cut-offs when conducting MD simulations on graphene-type systems.

4.4 | Conclusion

This chapter examined the structural and tensile properties of three folded graphene systems which had not been studied before. It was shown that graphene, when folded, tends to adopt conformations where, in analogy to what is observed at the macroscale when folding a sheet of paper, forms a bulge in the

proximity of the fold which to some extent replicates the curved structure of a nanotube. It was also shown that the location of the fold can be controlled through the presence of defects, thus permitting the graphene to fold more sharply and densely. These folded systems were also shown to exhibit a number of anomalous properties upon stretching which include a zero Poisson's ratio and a negative tangent modulus, properties which were adequately explained from the deformation profile.

5

Conclusion and Further Work

Graphene, often hailed as the "wonder material" of the 21st century, is gradually finding its way into a wide variety of commercial applications, including energy storage, structural reinforcement, biomedicine, and optoelectronic devices. Despite all this, there are various features and properties of graphene which merit further investigation, particularly, as this work attests, novel characteristics and aspects which emanate from structural modifications to this nanomaterial.

The present dissertation has focused on the mechanical behaviour of multiply folded graphenes and forms part of a wider study undertaken on graphene-type materials exhibiting anomalous mechanical properties. This began in 2015 with a published study which revealed that, through a random placement of V_1(5-9) defects, it was possible to fine-tune the morphology of graphene by forcing it to 'wrinkle' more extensively to resemble crumpled paper, and manifest negative Poisson's ratio as a direct result (Grima *et al.*, 2015). More recent work involving deterministically placed defects led to the discovery of energetically stable graphene conformations which resembled corrugated sheets, and the realisation that folded regions impart auxetic character, analogous to a 'corrugated' sheet of material that is pulled flat off-axis and re-flattened (Grima *et al.*, 2018). This work focused on a more pronounced form of corrugation where each of the modelled graphene systems resembled a pleated folded sheet, appropriately referred to as 'folded graphene'.

In the first part of the dissertation, an *ad hoc* protocol was developed, executable within the LAMMPS environment, for simulating the uniaxial stretching of graphene-type materials. Since the quality of any modelling study is contingent upon the simulation setup and the assumptions made, it was

crucial that prior to being using, the protocol was subject to an adequate validation. Such a validation was performed successfully against pristine graphene for stretching along its two principal directions, namely the armchair and zigzag direction. Pristine graphene was chosen in view of the limited literature pertaining to the subject of folded graphenes and their mechanical properties and the fact that the folded graphenes as modelled in this work were never studied before. The validation results were accompanied by a discussion on key parameters defined within the simulation protocol itself, highlighting their respective role towards ensuring that the experimentally determined mechanical properties of graphene were replicated satisfactorily.

Once it was ascertained that the methodology expressed by the simulation protocol was appropriately developed, the protocol was applied to three novel forms of graphene conformations having folded, pleated-like domains. Comparison between these folded graphenes was made on the basis of *(i)* the stretching direction, and *(ii)* the presence or absence of patterned V_1(5-9) defects within their structure, to examine the influence that such features had on the fold characteristics and the deformation profile. It was shown that the defect fold lines, while non-essential for the stability of the folded regions at 300 K and 0 Pa, whenever present, constrained the modelled system to fold sharply and controllably into a high-density, graphite-like material. Conversely, in the pristine folded systems, the folded regions were more fluid and formed a bulge-like contour. These structural differences were explained, for the first time, via a macroscale model based on the mechanics of paper folding (creased vs. not creased). This shows, once again, the usefulness of likening graphene sheets to 'simple' sheets of paper when studying the mechanical properties of folded graphenes.

Through this work, it was also possible to demonstrate for the first time how graphene could be made even more versatile by exhibiting *(i)* anomalous Poisson's ratios, namely zero for loading on axis (proved through simulation) and possibly negative off-axis (extrapolated), and *(ii)* anomalous stiffness

properties, including a negative tangent modulus. It shall be fair to ascribe these fold-induced characteristics to the 'tertiary structure' of graphene; this term, borrowed from protein chemistry, hereby refers to the three-dimensional shape of the graphenic system which is ultimately conditioned by the non-bonded interactions of the molecular entities present within it, similar to a polypeptide.

To conclude, it is important to recognise that this study is simply a singular and minute contribution to the field of graphene research and should ideally be supplemented by further work for an even better insight into the properties of such a fascinating material and its folded conformations in particular. The previous chapter has identified a number of aspects which stemmed from the strengths and limitations of the present work that warrant further investigation. Apart from this, additional work may also focus on the applications' perspective, or aspects which due to time and resource limitations were not included in the present study.

A compelling avenue for future research into folded graphenes concerns whether other types of lattice point defects, such as the V_1(5-8-5) double-vacancy, produce graphene systems with fold characteristics and a deformation profile that are similar or different to what was observed in this study with regard to the defective folded graphene system having V_1(5-9) defects. Furthermore, due consideration shall be warranted to other possible methodologies besides lattice defect insertion which can also induce the formation of such pleated-like folds, namely patterned hydrogenation (Ho *et al.*, 2020) and nano-indentation (Wei *et al.*, 2020).

Another aspect that deserves further attention probes into the suitability of the folding cavities present within multiply folded graphene as potential intercalation sites for lithium-ions. Graphene has long been researched for improving the storage capacity and cyclic stability of the anode materials (Lee *et al.*, 2010; Liu *et al.*, 2016; Xu *et al.*, 2018), so there are clear benefits to explore this in more detail.

An interesting mechanical characteristic that was unfortunately overlooked by the present work is the load-unload cycle of the folded graphenes under

consideration. Work presented by Wang and Liu (2018) seems to indicate that carefully placed defects may guide the spontaneous folding of the material, and therefore, it would be meaningful to examine this aspect in terms of the folding line separation. Furthermore, it might also be possible that at different stages during the unfolding process, pristine folded graphenes could revert to their original, fully folded state once the applied strain is lifted.

Finally, on account of the novel aspects advanced by this research, further work, preferably based on physical experimentation, is required to fully confirm and validate the findings reported herein, namely the theoretical performance of novel folded graphenic systems under uniaxial deformation. Such an endeavour could also examine in greater detail how such systems may be applied in practical situations. Owing to the combined superior and anomalous electronic and mechanical properties of folded graphenes, these applications could include nano-electromechanical systems (NEMS) and smart grips, which respond anomalously to mechanical forces.

A

List of Publications

The work presented in this dissertation has been disseminated through the following conference papers:

(1) M. Gauci and J. N. Grima, "Modelling of the stress-strain properties of graphene through molecular dynamics". Paper presented at the 17th Conference on Functional and Nanostructured Materials, Paralia Katerinis, Greece, September 2021 (ABS15).

(2) M. Gauci and J. N. Grima, "On the structural properties of folded graphene systems: A molecular modelling study". Paper presented at the 17th Conference on Functional and Nanostructured Materials, Paralia Katerinis, Greece, September 2021 (ABS16).

(3) M. Gauci and J. N. Grima, "Simulation of stretching and unfolding of "folded graphene"". Paper presented at the 17th Conference on Functional and Nanostructured Materials, Paralia Katerinis, Greece, September 2021 (ABS17).

(4) M. Gauci and J. N. Grima, "Preliminary results on the anomalous stiffness properties obtained upon uniaxially stretching folded graphene with vacancy-type defects". Paper presented at the 17th Conference on Functional and Nanostructured Materials, Paralia Katerinis, Greece, September 2021 (ABS18).

B

LAMMPS Input Scripts

LAMMPS is an open-source software written in C++ with support for a wide range of MD simulation setups, depending on the inclusion of specific packages during its installation process. In order to execute the simulations documented in this dissertation, it was necessary for LAMMPS to be built with the `MANYBODY` package which defined a variety of bond-order and many-body pair style commands, including that for the AIREBO potential.

Another important aspect of LAMMPS is that it offers a number of performance-related packages which, if configured correctly, should lead to noticeable improvements in simulation performance. Therefore, prior to the execution of the validation study, a series of benchmark tests were performed using the problem sets that were provided in the `bench` directory of the LAMMPS distribution (October 2020 release) to identify the correct invocation of the LAMMPS binary for optimal performance. It was determined that, based on the available hardware, the AIREBO-based simulations ran the fastest at twelve MPI tasks with two threads per task and the inclusion of the acceleration features implemented in the `OPENMP` package:

```
mpirun -np 12 --oversubscribe /path/to/lammps/binary -sf omp -pk
↪  omp 2 -in /path/to/lammps/input/script
```

In view of the fact that LAMMPS is a command-line interface (CLI) software, input commands need to be text-based and are often supplied to the program in the form of a code file. From an academic standpoint, this is advantageous because it ensures that simulation protocols written for use within LAMMPS are easily shared among researchers to be reviewed or reproduced. Overall, the input scripts that were written for the validation study described in Chapter 3) were indistinguishable from each other except for the different input structure

and output file names used; the same was true for the input scripts that were written for the folded graphene simulations reported in Chapter 4. The only major difference between these two sets of scripts was the duration of the uniaxial stretching, which in the case of the folded graphene set was 2.5 ns – a 50-fold increase in simulation time compared to the validation set. Below is reproduced The full contents of the input script which enabled the simulation of the tensile behaviour of zigzag graphene during the validation study is reproduced below:

```
# ----------------------- OUTPUT DESTINATION -----------------------
variable log_name string zigzag
variable folder_name string VALIDATION_ZIGZAG
variable trial_run string 005
shell mkdir ${folder_name}-${trial_run}
log log.${log_name}-${trial_run}
# ------------------------ GENRAL SETTINGS --------------------------
units   metal
newton  on
neighbor     0.1 bin
neigh_modify delay 0 every 1 check yes
variable temperature equal 300.0
timestep ${timestep}
# ------------------------ SIMULATION BOX ---------------------------
dimension 3
boundary p   m   p
# -------------------------- BOND TYPE ------------------------------
atom_style atomic
# ------------------------ STRUCTURE FILE ---------------------------
read_data vld_zigzag.data
# -------------------------- FORCE FIELD ------------------------------
pair_style airebo 3.0  1  1
pair_coeff * * CH.airebo-rcmin C
# -------------------------- COMPUTES ------------------------------
compute peratomstress all stress/atom NULL
compute peratomstress_scalar all reduce sum c_peratomstress[1]
↪  c_peratomstress[3]
```

```
compute pe all pe
compute peratompe all pe/atom
compute ke all ke
compute peratomke all ke/atom
compute 1 all reduce ave c_peratomke
compute 2 all reduce avesq c_peratomke
variable ke_variance equal (c_2-(c_1)^2)
# ------------------------ OUTPUT SETTINGS -------------------------
shell cd ${folder_name}-${trial_run}
variable nevery equal 1
variable nrepeat equal 100
variable nfreq equal ${nevery}*${nrepeat}
thermo 100
thermo_style custom step temp press fmax fnorm pxx pyy pzz pe ke lx ly lz vol
↪  v_ke_variance
# ------------------------------ FIXES -------------------------------
fix avtemp all ave/time  ${nevery} ${nrepeat} ${nfreq} c_thermo_temp
variable avtemp equal f_avtemp
fix avtemp10k all ave/time 1 10000 10000 c_thermo_temp
variable avtemp10k equal f_avtemp10k
variable toteng equal c_ke+c_pe
fix toteng all ave/time ${nevery} ${nrepeat} ${nfreq} v_toteng
variable avtoteng equal f_toteng
fix toteng10k all ave/time 1 10000 10000 v_toteng
variable avtoteng10k equal f_toteng10k
fix pe all ave/time ${nevery} ${nrepeat} ${nfreq} c_thermo_pe
variable avpe equal f_pe
fix avpress10k all ave/time 1 10000 10000 c_thermo_press mode vector
variable avpxx10k equal f_avpress10k[1]
variable avpzz10k equal f_avpress10k[3]
# ------------------------ STRESS CALCULATIONS ----------------------
fix avstress all ave/time ${nevery} ${nrepeat} ${nfreq}
↪  c_peratomstress_scalar[1] c_peratomstress_scalar[2]
variable len_x equal lx
variable len_y equal ly
variable len_z equal lz
```

```
variable volume equal vol
fix avdim all ave/time ${nevery} ${nrepeat} ${nfreq} v_len_x v_len_y v_len_z v_volume
variable avx equal f_avdim[1]
variable avy equal f_avdim[2]
variable avz equal f_avdim[3]
variable avvol equal f_avdim[4]
variable bar_to_GPa equal 1.0e-4
variable sheet_thickness equal 3.35
variable adjusted_volume equal (v_sheet_thickness/v_avy)*v_avvol
variable sigma_xx equal f_avstress[1]/v_adjusted_volume*${bar_to_GPa}
variable sigma_zz equal f_avstress[2]/v_adjusted_volume*${bar_to_GPa}
run 10000
# -------------------------- MINIMISATION -------------------------
min_style cg
min_modify dmax 0.1 line forcezero
minimize 1.0e-10 1.0e-10 100000 1000000
variable remainder_to_next_10000 equal ceil(step/10000)*10000-step
run ${remainder_to_next_10000}
# ------------------------ NVT EQUILIBRATION ----------------------
shell mkdir EQUILIBRATED-NVT
shell cd EQUILIBRATED-NVT
variable output_type string equilibrated_nvt
variable step equal step
fix data_output all print ${nfreq} "${step} ${avtemp} ${avpe} ${avtoteng} ${avx} ${avz} ${sigma_xx} ${sigma_zz}" title "Step Temperature Potential_energy Total_energy Length_in_x Length_in_z Stress_in_x Stress_in_z" append ${output_type}.txt screen no
dump 1 all custom 1000 equil_nvt-*.lammpstrj id type xu yu zu vx vy vz c_peratompe c_peratomstress[1] c_peratomstress[2] c_peratomstress[3]
dump_modify 1 element C
velocity all create ${temperature} 10248676 dist gaussian mom yes rot yes
run 0
velocity all scale ${temperature}
fix 1 all nvt temp ${temperature} ${temperature} $(100.0*dt)
variable etol equal 1e-4
```

```
variable temptol equal 1e-3
variable nvtloop loop 100
label nvt_equilibration
 variable etot0 equal ${avtoteng10k}
 variable t0 equal ${avtemp10k}
 run 10000
 if "${t0} == 0" then "jump SELF nvt_equilibration"
 variable etotdiff equal sqrt((${avtoteng10k}-${etot0})/${etot0})^2)
 variable tempdiff equal sqrt((${avtemp10k}-${t0})/${t0})^2)
 print "NVT equilibration: ${step} ${avtemp10k} ${avpxx10k} ${avpzz10k}
 ↪  ${etotdiff} ${tempdiff}" append energy_monitoring.txt
 if "(${etotdiff} < ${etol}) && (${tempdiff} < ${temptol}) && (${avtemp10k} <
 ↪  302) && (${avtemp10k} > 298)" then "jump SELF break_nvt"
next nvtloop
jump SELF nvt_equilibration
label break_nvt
unfix 1
unfix data_output
undump 1
write_restart restart.${output_type}-${trial_run}
shell cd ..
# ------------------------- NPT EQUILIBRATION -----------------------
shell mkdir EQUILIBRATED-NPT
shell cd EQUILIBRATED-NPT
variable output_type string equilibrated_npt
fix data_output all print ${nfreq} "${step} ${avtemp} ${avpe} ${avtoteng} ${avx}
↪  ${avz} ${sigma_xx} ${sigma_zz}" title "Step Temperature Potential_energy
↪  Total_energy Length_in_x Length_in_z Stress_in_x Stress_in_z" append
↪  ${output_type}.txt screen no
dump 1 all custom 1000 equil_npt-*.lammpstrj id type xu yu zu vx vy vz
↪  c_peratompe c_peratomstress[1] c_peratomstress[2] c_peratomstress[3]
dump_modify 1 element C
fix 1 all npt temp ${temperature} ${temperature} $(100*dt) x 0 0 $(1000*dt) z 0
↪  0 $(1000*dt)
variable pxxtol equal 1e-2
variable pzztol equal 1e-2
```

```
variable nptloop loop 100
label npt_equilibration
 variable etot0 equal ${avtoteng10k}
 variable pxx0 equal ${avpxx10k}
 variable pzz0 equal ${avpzz10k}
 run 10000
 variable etotdiff equal sqrt(((${avtoteng10k}-${etot0})/${etot0})^2)
 if "(${pxx0} == 0) || (${pzz0} == 0)" then "jump SELF npt_equilibration"
 variable pxxdiff equal sqrt(((${avpxx10k}-${pxx0})/${pxx0})^2)
 variable pzzdiff equal sqrt(((${avpzz10k}-${pzz0})/${pzz0})^2)
 print "NPT equilibration: ${step} ${avtemp10k} ${avpxx10k} ${avpzz10k}
 ↪  ${etotdiff} ${pxxdiff} ${pzzdiff}" append energy_monitoring.txt
 if "(${etotdiff} < ${etol}) && (${pxxdiff} < ${pxxtol}) && (${pzzdiff} <
 ↪  ${pzztol})" then "jump SELF break_npt"
next nptloop
jump SELF npt_equilibration
label break_npt
unfix 1
unfix data_output
undump 1
write_restart restart.${output_type}-${trial_run}
shell cd ..
# ---------------------------- DEFORMATION -------------------------
shell mkdir DEFORMED
shell cd DEFORMED
variable output_type string deformed
variable pre_deformation_steps equal ${step}
variable erate equal 0.005
variable strain_per_timestep equal ${erate}*${timestep}
variable current_strain equal
↪  ${strain_per_timestep}*(step-${pre_deformation_steps})
fix data_output all print ${nfreq} "${step} ${avtemp} ${avpe} ${avtoteng} ${avx}
↪  ${avz} ${current_strain} ${sigma_xx} ${sigma_zz}" title "Step Temperature
↪  Potential_energy Total_energy Length_in_x Length_in_z Strain_in_x
↪  Stress_in_x Stress_in_z" append ${output_type}.txt screen no
```

```
dump 1 all custom 1000 deformed-*.lammpstrj id type xu yu zu vx vy vz
↪ c_peratompe c_peratomstress[1] c_peratomstress[2] c_peratomstress[3]
dump_modify 1 element C
fix 1 all npt temp ${temperature} ${temperature} $(100*dt) z 0 0 $(1000*dt)
↪ nreset 1
fix optimize all balance 250 1 shift x 10 1
fix 2 all deform 1 x erate ${erate} units box remap x
run 100000
unfix 1
unfix 2
unfix data_output
undump 1
write_restart restart.${output_type}-${trial_run}
shell cd ..
shell cd ..
```

Copies of the structure data files for the graphene systems used during the validation study (*vld_zigzag.data* and *vld_armchair.data*) and the three folded graphenes whose unfolding behaviour was examined in this dissertation (*folded_armchair.data*, *folded_zigzag.data*, and *folded_zigzag_with_defects.data*) have been included in the Supplementary Information.

C

Post-processing Scripts

I. Python script for averaging the data within a LAMMPS simulation dump file over different time intervals

```
1  import pandas as pd
2  import numpy as np
3  import itertools
4  import glob
5  import os
6
7  class TimeAveragedResults(object):
8      '''Uses the fix output dump file of a LAMMPS simulation to produce a MS
       ↪  Excel workbook having multiple sheets that present the data at different
       ↪  time-averaging intervals'''
9      TIMESTEP = 0.0005
10     FIX_SAMPLE_SIZE = 100  # fixes generate means every 100 samples
11     SAMPLE_SIZES = [10,100,200,300,400,500,1000] # sampling averages at 0.5-,
       ↪  5-, 10-, 15-, 20-, and 25-ps intervals
12     INPUT_FILE = 'deformed.txt'
13     OUTPUT_FILE = 'deformed_folded_armchair_pristine_sampling.xlsx'
14
15     def create_excel_sheet(self, n):
16         '''Produces time-averaged data and appends it to an open Excel workbook
           ↪  as a new sheet'''
17         zero_record = self.df.iloc[0].to_list()  # initial system information
18         df_without_zero_record = self.df.drop([0]).reset_index(drop=True)
19         label_series = pd.Series(
20             itertools.chain.from_iterable(itertools.repeat(x, n) for x in
               ↪  df_without_zero_record.index)
21         )
```

```
22          averaged_data = df_without_zero_record.groupby(label_series).mean()  #
            ↪ exclude last row if total number of rows is indivisible by n
23          averaged_data.loc[-1] = zero_record
24          averaged_data.index = averaged_data.index + 1
25          averaged_data.sort_index(inplace=True)
26          sample_time = n * TimeAveragedResults.FIX_SAMPLE_SIZE *
            ↪ TimeAveragedResults.TIMESTEP
27          averaged_data.to_excel(self.writer, sheet_name='{}
            ↪ ps'.format(sample_time), index=False, header=True)
28          return
29
30      def import_data(self):
31          '''Converts the fix data dump into a dataframe'''
32          df = pd.read_csv(TimeAveragedResults.INPUT_FILE, delimiter='\s+')
33          df = df.drop_duplicates(keep='first').reset_index(drop=True)  # removes
            ↪ any duplicate rows
34          return df
35
36      def main(self):
37          self.df = self.import_data()
38          self.writer = pd.ExcelWriter(TimeAveragedResults.OUTPUT_FILE,
            ↪ engine='xlsxwriter')
39          for n in TimeAveragedResults.SAMPLE_SIZES:
40              self.create_excel_sheet(n)
41          self.writer.save()
42          return
43
44  if __name__ == '__main__':
45      TimeAveragedResults().main()
```

II. Python script for the extraction of periodic images from the LAMMPS simulation dump files

```
from ovito.io import import_file
import ovito
from ovito.modifiers import CreateBondsModifier
from ovito.vis import Viewport, ParticlesVis, BondsVis, OpenGLRenderer
from ovito import dataset

SOURCE_FILE_PATTERN = 'ARMCHAIR/DEFORMED/deformed-*.lammpstrj'
DESTINATION_FOLDER = 'animations/armchair_snapshots/'

DUMP_INTERVAL = 1000
TIME_INTERVAL = 10      # in picoseconds
TIMESTEP = 0.0005       # in picoseconds

def camera_setup():
    vp = Viewport()
    vp.type = Viewport.Type.Ortho
    vp.camera_pos = (22.4213, 47.4411, 14.6247)
    vp.camera_dir = (0,0,-1)
    vp.fov = 130
    return vp

pipeline = import_file(SOURCE_FILE_PATTERN)
pipeline.add_to_scene()

pipeline.compute().particles.vis.shape = ParticlesVis.Shape.Sphere
pipeline.compute().particles.vis.radius = 0.8

def create_bonds(cutoff=2, width=0.4):
    modifier = CreateBondsModifier(cutoff=cutoff)
    modifier.vis.shading = BondsVis.Shading.Normal
    modifier.vis.width = width
    return modifier
```

```
pipeline.modifiers.append(create_bonds())
pipeline.source.data.cell.vis.render_cell = False
vp = camera_setup()
desired_markers = list(range(1,199))

for marker in desired_markers:
    frame = ((marker - 1) * (TIME_INTERVAL / TIMESTEP)) / DUMP_INTERVAL
    vp.render_image(
        size=(1920,1080),
        frame=frame,
        filename=f'{DESTINATION_FOLDER}{marker}.png',
        alpha=True,
        crop=True,
        renderer=OpenGLRenderer()
    )
```

III. Python script for the generation of animated plots showing the variation in stress and potential energy observed during the uniaxial tensile simulations of the folded graphenes

```
import matplotlib.pyplot as plt
from matplotlib.animation import FuncAnimation, FFMpegWriter,
↪ ImageMagickFileWriter
import pandas as pd

class AnimatedPlots(object):
    INPUT_FILE = 'deformed_armchair_10ps.csv'
    OUTPUT_FILE = 'deformed_armchair_10ps.mp4'
    PLOT_TITLE = 'Uniaxial stretching of folded pristine armchair graphene along
    ↪ the x direction'
    PRIMARY_AXIS_MIN_OFFSET = 0
```

```
10      PRIMARY_AXIS_MAX_OFFSET = 0.5
11      SECONDARY_AXIS_MIN_OFFSET = 0
12      SECONDARY_AXIS_MAX_OFFSET = 100
13
14      def update_frame(self, frame):
15          self.x_data.append(frame[2])
16          self.y1_data.append(frame[3])
17          self.y2_data.append(frame[1])
18          self.stress_plot.set_data(self.x_data, self.y1_data)
19          self.energy_plot.set_data(self.x_data, self.y2_data)
20          self.step_text.set_text('Step:  {}'.format(str(frame[0])))
21          return tuple([self.stress_plot]) + tuple([self.energy_plot]) +
            ↪  tuple([self.step_text])
22
23      def round_limit(self, x, base, limit_type):
24          if limit_type == 'min':
25              return base * int(x / base) if x > 0 else base * (int(x / base) - (x
                ↪  % base > 0))
26          elif limit_type == 'max':
27              return base * (int(x / base) + (x % base > 0)) if x > 0 else base *
                ↪  int(x / base)
28          else:
29              raise ValueError(
30                  "Failed to return an axis limit because the limit_type argument
                    ↪  was not set to 'min' or 'max'"
31              )
32
33      def init(self):
34          self.ax.set_xlim(self.df['Strain_in_x'].min(),
            ↪  self.df['Strain_in_x'].max())
35          self.ax.set_ylim(
36              self.round_limit(self.df['Stress_in_x'].min(), 0.5, 'min') +
                ↪  AnimatedPlots.PRIMARY_AXIS_MIN_OFFSET,
37              self.round_limit(self.df['Stress_in_x'].max(), 0.5, 'max') +
                ↪  AnimatedPlots.PRIMARY_AXIS_MAX_OFFSET
38          )
```

```
39          self.ax.set_xlabel('Strain (%)')
40          self.ax.set_ylabel('Stress (GPa)')
41          self.second_axes.set_ylim(
42              self.round_limit(self.df['Total_energy'].min(), 50, 'min') +
                ↪ AnimatedPlots.SECONDARY_AXIS_MIN_OFFSET,
43              self.round_limit(self.df['Total_energy'].max(), 50, 'max') +
                ↪ AnimatedPlots.SECONDARY_AXIS_MAX_OFFSET
44          )
45          self.second_axes.set_ylabel('Total energy (eV)', labelpad=8)
46          return self.stress_plot,
47
48      def create_animation(self):
49          anim = FuncAnimation(self.fig, init_func=self.init, frames=self.data,
            ↪ func=self.update_frame, blit=True)
50          if AnimatedPlots.OUTPUT_FILE.endswith('.gif'):
51              gif_writer = ImageMagickFileWriter(fps=30)
52              anim.save(AnimatedPlots.OUTPUT_FILE, writer=gif_writer)
53          else:
54              video_writer = FFMpegWriter(
55                  fps=2.5,
56                  bitrate=1000000,
57                  codec="libx264",
58                  extra_args=["-s", "1920x1080", "-preset",
                    ↪ "ultrafast","-crf","17", "-pix_fmt", "yuv444p"]
59              )
60              anim.save(AnimatedPlots.OUTPUT_FILE,
                ↪ savefig_kwargs={'facecolor':'white'}, writer=video_writer)
61
62      def import_data(self):
63          self.df = pd.read_csv(
64              AnimatedPlots.INPUT_FILE,
65              usecols=['Step', 'Total_energy', 'Strain_in_x', 'Stress_in_x'],
66              delimiter=','
67          )
68          self.df['Strain_in_x'] = self.df['Strain_in_x'] * 100
69          records = self.df.to_records(index=False)
```

```
70          return list(records)
71
72      def plot_builder(self):
73          plt.rcParams.update(
74              {'font.family':'sans-serif','font.sans-serif':['Lato']}
75          )  # changes default font to Lato
76          self.fig, self.ax = plt.subplots(figsize=(16,9))
77          self.stress_plot, = plt.plot([], [], 'ro', linestyle='-',
            ↪  label='Stress')
78          self.second_axes = self.ax.twinx()  # creates a second axes object with
            ↪  a shared x-axis
79          self.energy_plot, = self.second_axes.plot([], [], 'bo', linestyle='-',
            ↪  label='Total energy')
80          self.step_text = self.ax.text(0.02, 0.95, '',
            ↪  transform=self.ax.transAxes)  # creates a text object
81          arr_image = plt.imread('colour_gradient_updated.png', format='png')
82          axin = self.ax.inset_axes([0.008, 0.75, 0.1,
            ↪  0.1],transform=self.ax.transAxes)  # creates a static inset
83          axin.imshow(arr_image)
84          axin.axis('off')
85          plt.title(AnimatedPlots.PLOT_TITLE, fontdict={'fontsize': 16}, pad=20)
86          self.fig.legend(loc='upper right', bbox_to_anchor=(0.98,0.98),
            ↪  frameon=False, bbox_transform=self.ax.transAxes)
87
88      def main(self):
89          self.plot_builder()
90          self.data = self.import_data()
91          self.x_data, self.y1_data, self.y2_data = [], [], []
92          self.create_animation()
93
94  if __name__ == '__main__':
95      AnimatedPlots().main()
```

IV. Python script for evaluating the variation in the C–C bond length of pristine graphene while subjected to uniaxial stretching

```
from ovito.io import import_file, export_file
from ovito.modifiers import CalculateDisplacementsModifier,
↪  ExpressionSelectionModifier, ComputePropertyModifier, CreateBondsModifier
import pandas as pd
import numpy as np

SOURCE_FILE_PATTERN = 'VALIDATION_ZIGZAG/DEFORMED/deformed-*.lammpstrj'
OUTPUT_FILE = 'bond_analysis.txt'

pipeline = import_file(SOURCE_FILE_PATTERN)
pipeline.modifiers.append(CreateBondsModifier(cutoff = 1.9999999999999991))

def CCBondLength(frame, data):
    bond_lengths = data.bonds['Bond_length']
    mean_bond_length = np.average(bond_lengths)
    var_bond_length = np.var(bond_lengths)
    data.attributes['Bond_length_mean'] = mean_bond_length
    data.attributes['Bond_length_var'] = var_bond_length

pipeline.modifiers.append(ComputePropertyModifier(
    operate_on = 'bonds',
    expressions = ('BondLength',),
    output_property='Bond_length')
)

pipeline.modifiers.append(
    CCBondLength
)

def DisplacementInY(frame, data):
```

```
30      displacement_magnitudes = data.particles['Displacement Magnitude']
31      absolute_values = np.absolute(displacement_magnitudes)
32      mean_displacement = np.average(absolute_values)
33      var_displacement = np.var(absolute_values)
34      data.attributes['oop_displacement_mean'] = mean_displacement
35      data.attributes['oop_displacement_var'] = var_displacement
36
37  pipeline.modifiers.append(ComputePropertyModifier(
38      expressions = ('\nPosition.Y',),
39      output_property = 'Displacement Magnitude',
40      cutoff_radius = 3.9999999999999996))
41
42  pipeline.modifiers.append(
43      DisplacementInY
44  )
45
46  export_file(
47      pipeline,
48      OUTPUT_FILE,
49      format='txt/attr',
50      columns = ['Timestep', 'Bond_length_mean', 'Bond_length_var',
        ↪  'oop_displacement_mean', 'oop_displacement_var'],
51      multiple_frames=True
52  )
```

D

Simulation Video Content

In order to highlight the rippled effect of the pristine graphene systems modelled in Chapter 3 and to better represent the structural stability of the three folded graphenic systems modelled in Chapter 4, animations were generated for the final 100 ps of NPT equilibration stage specific to each system oriented in the xz-plane and made available in the Supplementary Information:

- *npt_vld_armchair.mp4*
- *npt_vld_zigzag.mp4*
- *npt_folded_armchair.mp4*
- *npt_folded_zigzag.mp4*
- *npt_folded_zigzag_with_defects.mp4*

Moreover, also included in the Supplementary Information, is a second set of animations showing the structural changes that occurred in these systems when they were subjected to uniaxial stretching in the x-direction, accompanied by the real-time variation in the stress (GPa) and potential energy (eV) mean values over a 10 ps interval:

- *folded_armchair_unfolding.mp4*
- *folded_zigzag_unfolding.mp4*
- *folded_zigzag_with_defects_unfolding.mp4*

References

Anand, A.; Unnikrishnan, B.; Mao, J.-Y.; Lin, H.-J.; and Huang, C.-C. Graphene-based nanofiltration membranes for improving salt rejection, water flux and antifouling–A review. *Desalination* **2018**, *429*, 119–133.

Bae, S.; Kim, H.; Lee, Y.; Xu, X.; Park, J.-S.; Zheng, Y.; Balakrishnan, J.; Lei, T.; Kim, H. R.; Song, Y. I. *et al.* Roll-to-roll production of 30-inch graphene films for transparent electrodes. *Nature nanotechnology* **2010**, *5* (8), 574.

Bai, K.-K.; Zhou, Y.; Zheng, H.; Meng, L.; Peng, H.; Liu, Z.; Nie, J.-C.; and He, L. Creating one-dimensional nanoscale periodic ripples in a continuous mosaic graphene monolayer. *Physical review letters* **2014**, *113* (8), 086102.

Baimova, J. A.; Liu, B.; Dmitriev, S. V.; and Zhou, K. Mechanical properties of crumpled graphene under hydrostatic and uniaxial compression. *Journal of Physics D: Applied Physics* **2015**, *48* (9), 095302.

Balandin, A. A.; Ghosh, S.; Bao, W.; Calizo, I.; Teweldebrhan, D.; Miao, F.; and Lau, C. N. Superior thermal conductivity of single-layer graphene. *Nano letters* **2008**, *8* (3), 902–907.

Bangert, U.; Gass, M.; Bleloch, A.; Nair, R.; and Geim, A. Manifestation of ripples in free-standing graphene in lattice images obtained in an aberration-corrected scanning transmission electron microscope **2009**.

Barnard, A. S. and Snook, I. K. Ripple induced changes in the wavefunction of graphene: an example of a fundamental symmetry breaking. *Nanoscale* **2012**, *4* (4), 1167–1170.

Becton, M. and Wang, X. Tailoring patterns of graphene wrinkles by circular torsion. *Applied Surface Science* **2016**, *363*, 13–20.

Becton, M.; Zhang, L.; and Wang, X. Mechanics of graphyne crumpling. *Physical Chemistry Chemical Physics* **2014**, *16* (34), 18233–18240.

Becton, M.; Zhang, L.; and Wang, X. On the crumpling of polycrystalline graphene by molecular dynamics simulation. *Physical Chemistry Chemical Physics* **2015**, *17* (9), 6297–6304.

Bianco, A.; Cheng, H.-M.; Enoki, T.; Gogotsi, Y.; Hurt, R. H.; Koratkar, N.; Kyotani, T.; Monthioux, M.; Park, C. R.; Tascon, J. M. *et al.* All in the graphene family–a recommended nomenclature for two-dimensional carbon materials. **2013**, .

Bistritzer, R. and MacDonald, A. H. Moiré bands in twisted double-layer graphene. *Proceedings of the National Academy of Sciences* **2011**, *108* (30), 12233–12237.

Boehm, H.; Setton, R.; and Stumpp, E. Nomenclature and terminology of graphite intercalation compounds. *Carbon* **1986**, *24* (2), 241–245.

Bonaccorso, F.; Sun, Z.; Hasan, T.; and Ferrari, A. Graphene photonics and optoelectronics. *Nature photonics* **2010**, *4* (9), 611.

Borca, B.; Calleja, F.; Hinarejos, J.; de Parga, A. V.; and Miranda, R. Reactivity of periodically rippled graphene grown on Ru (0001). *Journal of Physics: Condensed Matter* **2009**, *21* (13), 134002.

Brenner, D. W. Empirical potential for hydrocarbons for use in simulating the chemical vapor deposition of diamond films. *Physical review B* **1990**, *42* (15), 9458.

Cai, K.; Yang, Y.; Shi, J.; Zhong, Z.; and Qin, Q.-H. Thermal stability of a nanoporous graphene membrane candidate from an orthogonal-diagonal nanotexture: A molecular dynamics test. *Applied Surface Science* **2021**, , 149955.

Cao, Y.; Fatemi, V.; Demir, A.; Fang, S.; Tomarken, S. L.; Luo, J. Y.; Sanchez-Yamagishi, J. D.; Watanabe, K.; Taniguchi, T.; Kaxiras, E. *et al.* Correlated

insulator behaviour at half-filling in magic-angle graphene superlattices. *Nature* **2018**a, *556* (7699), 80–84.

Cao, Y.; Fatemi, V.; Fang, S.; Watanabe, K.; Taniguchi, T.; Kaxiras, E.; and Jarillo-Herrero, P. Unconventional superconductivity in magic-angle graphene superlattices. *Nature* **2018**b, *556* (7699), 43–50.

Chain, E.; Florey, H.; Gardner, A.; Heatley, N.; Jennings, M.; Orr-Ewing, J.; and Sanders, A. Pencillin as a chemotherapeutic agent. *The Lancet* **1940**, *236* (6104), 226–228.

Chang, C.; Song, Z.; Lin, J.; and Xu, Z. How graphene crumples are stabilized? *RSC Advances* **2013**, *3* (8), 2720–2726.

Chen, H.; Zhang, X.-L.; Zhang, Y.-Y.; Wang, D.; Bao, D.-L.; Que, Y.; Xiao, W.; Du, S.; Ouyang, M.; Pantelides, S. T. *et al.* Atomically precise, custom-design origami graphene nanostructures. *Science* **2019**, *365* (6457), 1036–1040.

Choi, J. S.; Kim, J.-S.; Byun, I.-S.; Lee, D. H.; Hwang, I. R.; Park, B. H.; Choi, T.; Park, J. Y.; and Salmeron, M. Facile characterization of ripple domains on exfoliated graphene. *Review of Scientific Instruments* **2012**, *83* (7), 073905.

Clark, K. W.; Zhang, X.-G.; Vlassiouk, I. V.; He, G.; Feenstra, R. M.; and Li, A.-P. Spatially resolved mapping of electrical conductivity across individual domain (grain) boundaries in graphene. *ACS nano* **2013**, *7* (9), 7956–7966.

Dean, C. R.; Young, A. F.; Meric, I.; Lee, C.; Wang, L.; Sorgenfrei, S.; Watanabe, K.; Taniguchi, T.; Kim, P.; Shepard, K. L. *et al.* Boron nitride substrates for high-quality graphene electronics. *Nature nanotechnology* **2010**, *5* (10), 722–726.

Deng, S.; Gao, E.; Wang, Y.; Sen, S.; Sreenivasan, S. T.; Behura, S.; Kral, P.; Xu, Z.; and Berry, V. Confined, oriented, and electrically anisotropic graphene wrinkles on bacteria. *ACS nano* **2016**, *10* (9), 8403–8412.

Dimov, D.; Amit, I.; Gorrie, O.; Barnes, M. D.; Townsend, N. J.; Neves, A. I.; Withers, F.; Russo, S.; and Craciun, M. F. Ultrahigh performance nanoengineered graphene–concrete composites for multifunctional applications. *Advanced functional materials* **2018**, *28* (23), 1705183.

Dresselhaus, M. and Dresselhaus, G. Intercalation compounds of graphite. *Advances in Physics* **1981**, *30* (2), 139–326.

Fang, L.; Muhlstein, C. L.; Collins, J. G.; Romasco, A. L.; and Friedman, L. H. Continuous electrical in situ contact area measurement during instrumented indentation. *Journal of Materials Research* **2008**, *23* (9), 2480–2485.

Fasolino, A.; Los, J.; and Katsnelson, M. I. Intrinsic ripples in graphene. *Nature materials* **2007**, *6* (11), 858–861.

Fleming, A. On the antibacterial action of cultures of a penicillium, with special reference to their use in the isolation of B. influenzae. *British journal of experimental pathology* **1929**, *10* (3), 226.

Frank, O.; Tsoukleri, G.; Parthenios, J.; Papagelis, K.; Riaz, I.; Jalil, R.; Novoselov, K. S.; and Galiotis, C. Compression behavior of single-layer graphenes. *ACS nano* **2010**, *4* (6), 3131–3138.

Frank, O.; Tsoukleri, G.; Riaz, I.; Papagelis, K.; Parthenios, J.; Ferrari, A. C.; Geim, A. K.; Novoselov, K. S.; and Galiotis, C. Development of a universal stress sensor for graphene and carbon fibres. *Nature Communications* **2011**, *2* (1), 1–7.

Friedman, J. S.; Girdhar, A.; Gelfand, R. M.; Memik, G.; Mohseni, H.; Taflove, A.; Wessels, B. W.; Leburton, J.-P.; and Sahakian, A. V. Cascaded spintronic logic with low-dimensional carbon. *Nature communications* **2017**, *8* (1), 1–7.

Fujisawa, N.; Ruffell, S.; Bradby, J.; Williams, J.; Haberl, B.; and Warren, O. Understanding pressure-induced phase-transformation behavior in silicon through in situ electrical probing under cyclic loading conditions **2009**.

Gannett, W. J. *Electronic Transport in Novel Graphene Nanostructures* Ph.D. thesis, UC Berkeley, **2012**.

Gass, M. H.; Bangert, U.; Bleloch, A. L.; Wang, P.; Nair, R. R.; and Geim, A. Free-standing graphene at atomic resolution. *Nature nanotechnology* **2008**, *3* (11), 676–681.

Gauci, M. On folded graphene and its properties: A preliminary study **2018**.

Gayk, F.; Ehrens, J.; Heitmann, T.; Vorndamme, P.; Mrugalla, A.; and Schnack, J. Young's moduli of carbon materials investigated by various classical molecular dynamics schemes. *Physica E: Low-dimensional Systems and Nanostructures* **2018**, *99*, 215–219.

Geim, A. K. and Novoselov, K. S. The rise of graphene *Nanoscience and technology: a collection of reviews from nature journals* World Scientific, **2010** 11–19.

Goodenough, J. B. Evolution of strategies for modern rechargeable batteries. *Accounts of chemical research* **2013**, *46* (5), 1053–1061.

Greenwood, N. N. and Earnshaw, A. *Chemistry of the Elements* Elsevier, **2012**.

Grima, J. N.; Grech, M. C.; Grima-Cornish, J. N.; Gatt, R.; and Attard, D. Giant auxetic behaviour in engineered graphene. *Annalen der Physik* **2018**, *530* (6), 1700330.

Grima, J. N.; Winczewski, S.; Mizzi, L.; Grech, M. C.; Cauchi, R.; Gatt, R.; Attard, D.; Wojciechowski, K. W.; and Rybicki, J. Tailoring graphene to achieve negative Poisson's ratio properties. *Advanced materials* **2015**, *27* (8), 1455–1459.

Guinea, F.; Horovitz, B.; and Le Doussal, P. Gauge fields, ripples and wrinkles in graphene layers. *Solid State Communications* **2009**, *149* (27-28), 1140–1143.

Guinea, F.; Katsnelson, M.; and Vozmediano, M. Midgap states and charge inhomogeneities in corrugated graphene. *Physical Review B* **2008**, *77* (7), 075422.

Guisinger, N. P. and Arnold, M. S. Beyond silicon: carbon-based nanotechnology. *MRS bulletin* **2010**, *35* (4), 273–279.

Hallam, T.; Shakouri, A.; Poliani, E.; Rooney, A. P.; Ivanov, I.; Potie, A.; Taylor, H. K.; Bonn, M.; Turchinovich, D.; Haigh, S. J. *et al.* Controlled folding of graphene: GraFold printing. *Nano letters* **2015**, *15* (2), 857–863.

Hayashi, T.; Kim, Y. A.; Matoba, T.; Esaka, M.; Nishimura, K.; Tsukada, T.; Endo, M.; and Dresselhaus, M. S. Smallest freestanding single-walled carbon nanotube. *Nano letters* **2003**, *3* (7), 887–889.

Hernandez, E.; Goze, C.; Bernier, P.; and Rubio, A. Elastic properties of C and B x C y N z composite nanotubes. *Physical Review Letters* **1998**, *80* (20), 4502.

Ho, D. T.; Ho, V. H.; Babar, V.; Kim, S. Y.; and Schwingenschlögl, U. Complex three-dimensional graphene structures driven by surface functionalization. *Nanoscale* **2020**, *12* (18), 10172–10179.

Hofer, C.; Kramberger, C.; Monazam, M. R. A.; Mangler, C.; Mittelberger, A.; Argentero, G.; Kotakoski, J.; and Meyer, J. C. Revealing the 3D structure of graphene defects. *2D Materials* **2018**, *5* (4), 045029.

Horiuchi, S.; Gotou, T.; Fujiwara, M.; Asaka, T.; Yokosawa, T.; and Matsui, Y. Single graphene sheet detected in a carbon nanofilm. *Applied physics letters* **2004**, *84* (13), 2403–2405.

Huang, P.; Li, Y.; Yang, G.; Li, Z.-X.; Li, Y.-Q.; Hu, N.; Fu, S.-Y.; and Novoselov, K. S. Graphene film for thermal management: A review. *Nano Materials Science* **2020**, .

Hui, Z. and Chang, Y. Phonon heat transport properties of graphene based on molecular dynamics simulations and lattice dynamics. *International Journal of Modern Physics B* **2019**, *33* (05), 1950020.

Humphrey, W.; Dalke, A.; and Schulten, K. VMD – Visual Molecular Dynamics. *Journal of Molecular Graphics* **1996**, *14*, 33–38.

Hunter, C. A. Arene—arene interactions: electrostatic or charge transfer? *Angewandte Chemie International Edition in English* **1993**, *32* (11), 1584–1586.

Iijima, S. Helical microtubules of graphitic carbon. *nature* **1991**, *354* (6348), 56–58.

Jiang, D.-e.; Sumpter, B. G.; and Dai, S. Unique chemical reactivity of a graphene nanoribbon's zigzag edge. *The Journal of chemical physics* **2007**, *126* (13), 134701.

Kalosakas, G.; Lathiotakis, N.; Galiotis, C.; and Papagelis, K. In-plane force fields and elastic properties of graphene. *Journal of Applied Physics* **2013**, *113* (13), 134307.

Kang, P.; Kim, K.-H.; Park, H.-G.; and Nam, S. Mechanically reconfigurable architectured graphene for tunable plasmonic resonances. *Light: Science & Applications* **2018**, *7* (1), 1–9.

Katsnelson, M. and Geim, A. Electron scattering on microscopic corrugations in graphene. *Philosophical Transactions of the Royal Society A: Mathematical, Physical and Engineering Sciences* **2008**, *366* (1863), 195–204.

Khalaj, Z.; Monajjemi, M.; and Diudea, M. V. Main Allotropes of Carbon: A Brief Review. *Sustainable Nanosystems Development, Properties, and Applications* **2017**, , 185–213.

Kim, K.; Lee, Z.; Malone, B. D.; Chan, K. T.; Alemán, B.; Regan, W.; Gannett, W.; Crommie, M.; Cohen, M. L.; and Zettl, A. Multiply folded graphene. *Physical Review B* **2011**, *83* (24), 245433.

Kohlmeyer, A. TopoTools: Release 1.7 **2016**.

Kroto, H. W.; Heath, J. R.; O'Brien, S. C.; Curl, R. F.; and Smalley, R. E. C 60: buckminsterfullerene. *nature* **1985**, *318* (6042), 162–163.

Kudin, K. N.; Scuseria, G. E.; and Yakobson, B. I. C 2 F, BN, and C nanoshell elasticity from ab initio computations. *Physical Review B* **2001**, *64* (23), 235406.

Lakes, R. Extreme damping in composite materials with a negative stiffness phase. *Physical review letters* **2001**, *86* (13), 2897.

Landau, L. Zur Theorie der phasenumwandlungen II. *Phys. Z. Sowjetunion* **1936**, *11*, 26–35.

Lanza, M.; Wang, Y.; Bayerl, A.; Gao, T.; Porti, M.; Nafria, M.; Liang, H.; Jing, G.; Liu, Z.; Zhang, Y. *et al.* Tuning graphene morphology by substrate towards wrinkle-free devices: Experiment and simulation. *Journal of Applied Physics* **2013**, *113* (10), 104301.

Lee, C.; Wei, X.; Kysar, J. W.; and Hone, J. Measurement of the elastic properties and intrinsic strength of monolayer graphene. *science* **2008**, *321* (5887), 385–388.

Lee, J. K.; Smith, K. B.; Hayner, C. M.; and Kung, H. H. Silicon nanoparticles–graphene paper composites for Li ion battery anodes. *Chemical communications* **2010**, *46* (12), 2025–2027.

Lee, J.-K.; Yamazaki, S.; Yun, H.; Park, J.; Kennedy, G. P.; Kim, G.-T.; Pietzsch, O.; Wiesendanger, R.; Lee, S.; Hong, S. *et al.* Modification of electrical properties of graphene by substrate-induced nanomodulation. *Nano letters* **2013**, *13* (8), 3494–3500.

Lin, F.; Xiang, Y.; and Shen, H.-S. Tunable Positive/Negative Young's Modulus in Graphene-Based Metamaterials. *Advanced Theory and Simulations* **2021**, *4* (2), 2000130.

Lin, Y.-C.; Jin, C.; Lee, J.-C.; Jen, S.-F.; Suenaga, K.; and Chiu, P.-W. Clean transfer of graphene for isolation and suspension. *ACS nano* **2011**, *5* (3), 2362–2368.

Lindsay, L.; Broido, D.; and Mingo, N. Flexural phonons and thermal transport in multilayer graphene and graphite. *Physical Review B* **2011**, *83* (23), 235428.

Liu, F.; Ming, P.; and Li, J. Ab initio calculation of ideal strength and phonon instability of graphene under tension. *Physical Review B* **2007**, *76* (6), 064120.

Liu, J.; Zheng, Q.; Goodman, M. D.; Zhu, H.; Kim, J.; Krueger, N. A.; Ning, H.; Huang, X.; Liu, J.; Terrones, M. *et al.* Graphene sandwiched mesostructured Li-ion battery electrodes. *Advanced Materials* **2016**, *28* (35), 7696–7702.

Lu, Q.; Arroyo, M.; and Huang, R. Elastic bending modulus of monolayer graphene. *Journal of Physics D: Applied Physics* **2009**, *42* (10), 102002.

Lui, C. H.; Liu, L.; Mak, K. F.; Flynn, G. W.; and Heinz, T. F. Ultraflat graphene. *Nature* **2009**, *462* (7271), 339–341.

Ma, R.-S.; Ma, J.; Yan, J.; Wu, L.; Guo, W.; Wang, S.; Huan, Q.; Bao, L.; Pantelides, S. T.; and Gao, H.-J. Wrinkle-induced highly conductive channels in graphene on SiO 2/Si substrates. *Nanoscale* **2020**, *12* (22), 12038–12045.

Martyna, G. J.; Tobias, D. J.; and Klein, M. L. Constant pressure molecular dynamics algorithms. *The Journal of chemical physics* **1994**, *101* (5), 4177–4189.

Mermin, N. D. Crystalline order in two dimensions. *Physical Review* **1968**, *176* (1), 250.

Meyer, J. C.; Geim, A. K.; Katsnelson, M. I.; Novoselov, K. S.; Booth, T. J.; and Roth, S. The structure of suspended graphene sheets. *Nature* **2007**, *446* (7131), 60–63.

Molyneux, W. Supports for vibration isolation. **1957**, .

Morozov, S.; Novoselov, K.; Katsnelson, M.; Schedin, F.; Elias, D.; Jaszczak, J. A.; and Geim, A. Giant intrinsic carrier mobilities in graphene and its bilayer. *Physical review letters* **2008**, *100* (1), 016602.

Nakada, K.; Fujita, M.; Dresselhaus, G.; and Dresselhaus, M. S. Edge state in graphene ribbons: Nanometer size effect and edge shape dependence. *Physical Review B* **1996**, *54* (24), 17954.

Nakada, K. and Ishii, A. Migration of adatom adsorption on graphene using DFT calculation. *Solid State Communications* **2011**, *151* (1), 13–16.

Ni, G.-X.; Zheng, Y.; Bae, S.; Kim, H. R.; Pachoud, A.; Kim, Y. S.; Tan, C.-L.; Im, D.; Ahn, J.-H.; Hong, B. H. *et al.* Quasi-periodic nanoripples in graphene grown by chemical vapor deposition and its impact on charge transport. *ACS nano* **2012**, *6* (2), 1158–1164.

Ni, Z.; Bu, H.; Zou, M.; Yi, H.; Bi, K.; and Chen, Y. Anisotropic mechanical properties of graphene sheets from molecular dynamics. *Physica B: Condensed Matter* **2010**, *405* (5), 1301–1306.

Nicolaou, Z. G. and Motter, A. E. Mechanical metamaterials with negative compressibility transitions. *Nature materials* **2012**, *11* (7), 608–613.

Nika, D. L. and Balandin, A. A. Two-dimensional phonon transport in graphene. *Journal of Physics: Condensed Matter* **2012**, *24* (23), 233203.

Ning, W.; Chen, Y.; Cai, K.; Zhang, Y.; Pei, Q.; Zheng, J.-C.; Mai, Y.-W.; and Zhao, J. Unusual thermal properties of graphene origami crease: A molecular dynamics study. *Green Energy & Environment* **2020**, .

Nosé, S. A unified formulation of the constant temperature molecular dynamics methods. *The Journal of chemical physics* **1984**, *81* (1), 511–519.

Novoselov, K. S.; Geim, A. K.; Morozov, S. V.; Jiang, D.; Katsnelson, M. I.; and Grigorieva Two-dimensional gas of massless Dirac fermions in graphene. *nature* **2005**, *438* (7065), 197–200.

Novoselov, K. S.; Geim, A. K.; Morozov, S. V.; Jiang, D.; Zhang, Y.; Dubonos, S. V.; Grigorieva, I. V.; and Firsov, A. A. Electric field effect in atomically thin carbon films. *science* **2004**, *306* (5696), 666–669.

Olabi, A.; Abdelkareem, M. A.; Wilberforce, T.; and Sayed, E. T. Application of graphene in energy storage device–A review. *Renewable and Sustainable Energy Reviews* **2021**, *135*, 110026.

Oostinga, J. B.; Heersche, H. B.; Liu, X.; Morpurgo, A. F.; and Vandersypen, L. M. Gate-induced insulating state in bilayer graphene devices. *Nature materials* **2008**, *7* (2), 151–157.

Ouyang, T.; Chen, Y.; Xie, Y.; Stocks, G. M.; and Zhong, J. Thermal conductance modulator based on folded graphene nanoribbons. *Applied Physics Letters* **2011**, *99* (23), 233101.

Park, B.-J.; Choi, J.-S.; Eom, J.-H.; Ha, H.; Kim, H. Y.; Lee, S.; Shin, H.; and Yoon, S.-G. Defect-free graphene synthesized directly at 150 C via chemical vapor deposition with no transfer. *ACS nano* **2018**, *12* (2), 2008–2016.

Paronyan, T. M.; Pigos, E. M.; Chen, G.; and Harutyunyan, A. R. Formation of ripples in graphene as a result of interfacial instabilities. *ACS nano* **2011**, *5* (12), 9619–9627.

Parrinello, M. and Rahman, A. Polymorphic transitions in single crystals: A new molecular dynamics method. *Journal of Applied physics* **1981**, *52* (12), 7182–7190.

Peierls, R. Quelques propriétés typiques des corps solides *Annales de l'institut Henri Poincaré*, volume 5 177–222.

Peng, W. and Sun, K. Effects of Cu/graphene interface on the mechanical properties of multilayer Cu/graphene composites. *Mechanics of Materials* **2020**, *141*, 103270.

Pereira, V. M. and Neto, A. C. Strain engineering of graphene's electronic structure. *Physical review letters* **2009**, *103* (4), 046801.

Plimpton, S. Fast parallel algorithms for short-range molecular dynamics. *Journal of computational physics* **1995**, *117* (1), 1–19.

Plimpton, S.; Thompson, A.; Moore, S.; Kohlmeyer, A.; and Berger, R. LAMMPS Documentation **2021** [Online] https://lammps.sandia.gov/doc/Manual.pdf (accessed May 20, 2021).

Qin, H.; Sun, J.; Liang, S.; Li, X.; Yang, X.; He, Z.; Yu, C.; and Feng, Z. Room-temperature, low-impedance and high-sensitivity terahertz direct detector based on bilayer graphene field-effect transistor. *Carbon* **2017**, *116*, 760–765.

Radamson, H. H. *Graphene* Springer International Publishing, **2017** 1–1.

Radchenko, T.; Tatarenko, V.; Sagalianov, I. Y.; and Prylutskyy, Y. I. Effects of nitrogen-doping configurations with vacancies on conductivity in graphene. *Physics Letters A* **2014**, *378* (30-31), 2270–2274.

Rajkamal, A. and Thapa, R. Carbon allotropes as anode material for lithium-ion batteries. *Advanced Materials Technologies* **2019**, *4* (10), 1900307.

Ren, S.; Rong, P.; and Yu, Q. Preparations, properties and applications of graphene in functional devices: A concise review. *Ceramics International* **2018**, *44* (11), 11940–11955.

Ruffell, S.; Sears, K.; Knights, A. P.; Bradby, J.; and Williams, J. Experimental evidence for semiconducting behavior of Si-XII. *Physical Review B* **2011**, *83* (7), 075316.

Sakhaee-Pour, A. Elastic properties of single-layered graphene sheet. *Solid State Communications* **2009**, *149* (1-2), 91–95.

Schneider, T. and Stoll, E. Molecular-dynamics study of a three-dimensional one-component model for distortive phase transitions. *Physical Review B* **1978**, *17* (3), 1302.

Sevinçli, H. and Cuniberti, G. Enhanced thermoelectric figure of merit in edge-disordered zigzag graphene nanoribbons. *Physical Review B* **2010**, *81* (11), 113401.

Shenderova, O.; Brenner, D.; Omeltchenko, A.; Su, X.; and Yang, L. Atomistic modeling of the fracture of polycrystalline diamond. *Physical Review B* **2000**, *61* (6), 3877.

Shewchuk, J. R. *et al.* An introduction to the conjugate gradient method without the agonizing pain **1994**.

Shinoda, W.; Shiga, M.; and Mikami, M. Rapid estimation of elastic constants by molecular dynamics simulation under constant stress. *Physical Review B* **2004**, *69* (13), 134103.

Shioyama, H. Cleavage of graphite to graphene. *Journal of materials science letters* **2001**, *20* (6), 499–500.

Slonczewski, J. and Weiss, P. Band structure of graphite. *Physical Review* **1958**, *109* (2), 272.

Song, J. C.; Shytov, A. V.; and Levitov, L. S. Electron interactions and gap opening in graphene superlattices. *Physical review letters* **2013**, *111* (26), 266801.

Stuart, S. J.; Tutein, A. B.; and Harrison, J. A. A reactive potential for hydrocarbons with intermolecular interactions. *The Journal of chemical physics* **2000**, *112* (14), 6472–6486.

Su, N.; Liu, M.; and Liu, F. Chemical versus thermal folding of graphene edges. *Nano Research* **2011**, *4* (12), 1242–1247.

Tersoff, J. New empirical approach for the structure and energy of covalent systems. *Physical review B* **1988**, *37* (12), 6991.

Torres-Dias, A. C.; Cerqueira, T. F.; Cui, W.; Marques, M. A.; Botti, S.; Machon, D.; Hartmann, M. A.; Sun, Y.; Dunstan, D. J.; and San-Miguel, A. From mesoscale to nanoscale mechanics in single-wall carbon nanotubes. *Carbon* **2017**, *123*, 145–150.

Tsai, J.-L. and Tu, J.-F. Characterizing mechanical properties of graphite using molecular dynamics simulation. *Materials & Design* **2010**, *31* (1), 194–199.

Tsoukleri, G.; Parthenios, J.; Papagelis, K.; Jalil, R.; Ferrari, A. C.; Geim, A. K.; Novoselov, K. S.; and Galiotis, C. Subjecting a graphene monolayer to tension and compression. *small* **2009**, *5* (21), 2397–2402.

Uryu, S. and Ando, T. Electronic intertube transfer in double-wall carbon nanotubes. *Physical Review B* **2005**, *72* (24), 245403.

Van Lier, G.; Van Alsenoy, C.; Van Doren, V.; and Geerlings, P. Ab initio study of the elastic properties of single-walled carbon nanotubes and graphene. *Chemical Physics Letters* **2000**, *326* (1-2), 181–185.

Varchon, F.; Mallet, P.; Veuillen, J.-Y.; and Magaud, L. Ripples in epitaxial graphene on the Si-terminated SiC (0001) surface. *Physical Review B* **2008**, *77* (23), 235412.

Viculis, L. M.; Mack, J. J.; and Kaner, R. B. A chemical route to carbon nanoscrolls.(Brevia). *Science* **2003**, *299* (5611), 1361–1362.

Wagner, P.; Ewels, C. P.; Ivanovskaya, V. V.; Briddon, P. R.; Pateau, A.; and Humbert, B. Ripple edge engineering of graphene nanoribbons. *Physical Review B* **2011**, *84* (13), 134110.

Wakafuji, Y.; Moriya, R.; Masubuchi, S.; Watanabe, K.; Taniguchi, T.; and Machida, T. 3D manipulation of 2D materials using microdome polymer. *Nano letters* **2020**, *20* (4), 2486–2492.

Wallace, P. R. The band theory of graphite. *Physical review* **1947**, *71* (9), 622.

Wang, Y. and Liu, Z. Spontaneous rolling-up and assembly of graphene designed by using defects. *Nanoscale* **2018**, *10* (14), 6487–6495.

Wei, D.; Song, Y.; and Wang, F. A simple molecular mechanics potential for μm scale graphene simulations from the adaptive force matching method. *The Journal of chemical physics* **2011**, *134* (18), 184704.

Wei, N.; Chen, Y.; Zhang, Y.; Zheng, J.-C.; Zhao, J.; and Mai, Y.-W. Crease-induced targeted cutting and folding of graphene origami. *Carbon* **2020**, *165*, 259–266.

Willke, P.; Möhle, C.; Sinterhauf, A.; Kotzott, T.; Yu, H. K.; Wodtke, A.; and Wenderoth, M. Local transport measurements in graphene on SiO2 using Kelvin probe force microscopy. *Carbon* **2016**, *102*, 470–476.

Xie, Y.; Chen, Y.; Wei, X. L.; and Zhong, J. Electron transport in folded graphene junctions. *Physical Review B* **2012**, *86* (19), 195426.

Xu, P.; Neek-Amal, M.; Barber, S.; Schoelz, J.; Ackerman, M.; Thibado, P.; Sadeghi, A.; and Peeters, F. Unusual ultra-low-frequency fluctuations in freestanding graphene. *Nature communications* **2014**a, *5* (1), 1–7.

Xu, Q.; Sun, J.-K.; Yu, Z.-L.; Yin, Y.-X.; Xin, S.; Yu, S.-H.; and Guo, Y.-G. SiOx encapsulated in graphene bubble film: an ultrastable Li-ion battery anode. *Advanced Materials* **2018**, *30* (25), 1707430.

Xu, X.; Lin, C.; Fu, R.; Wang, S.; Pan, R.; Chen, G.; Shen, Q.; Liu, C.; Guo, X.; Wang, Y. *et al.* A simple method to tune graphene growth between monolayer and bilayer. *AIP Advances* **2016**, *6* (2), 025026.

Xu, X.; Pereira, L. F.; Wang, Y.; Wu, J.; Zhang, K.; Zhao, X.; Bae, S.; Bui, C. T.; Xie, R.; Thong, J. T. *et al.* Length-dependent thermal conductivity in suspended single-layer graphene. *Nature communications* **2014**b, *5* (1), 1–6.

Yang, N.; Ni, X.; Jiang, J.-W.; and Li, B. How does folding modulate thermal conductivity of graphene? *Applied Physics Letters* **2012**, *100* (9), 093107.

Yi, C.; Zhang, L.; Chen, X.; Wang, X.; and Ke, C. Nanomechanical unfolding of self-folded graphene on flat substrate. *Experimental Mechanics* **2019**, *59* (3), 381–386.

Yi, L.; Zhang, Y.; Wang, C.; and Chang, T. Temperature-induced unfolding of scrolled graphene and folded graphene. *Journal of Applied Physics* **2014**, *115* (20), 204307.

Zakharchenko, K.; Katsnelson, M.; and Fasolino, A. Finite temperature lattice properties of graphene beyond the quasiharmonic approximation. *Physical review letters* **2009**, *102* (4), 046808.

Zhang, D.; Jin, Z.; Shi, J.; Ma, P.; Peng, S.; Liu, X.; and Ye, T. The anistropy of field effect mobility of CVD graphene grown on copper foil. *Small* **2014**a, *10* (9), 1761–1764.

Zhang, J.; Xiao, J.; Meng, X.; Monroe, C.; Huang, Y.; and Zuo, J.-M. Free folding of suspended graphene sheets by random mechanical stimulation. *Physical review letters* **2010**, *104* (16), 166805.

Zhang, R.-S. and Jiang, J.-W. The art of designing carbon allotropes. *Frontiers of Physics* **2019**, *14* (1), 1–17.

Zhang, T.; Li, X.; and Gao, H. Designing graphene structures with controlled distributions of topological defects: A case study of toughness enhancement in graphene ruga. *Extreme Mechanics Letters* **2014**b, *1*, 3–8.

Zhang, T.; Li, X.; Kadkhodaei, S.; and Gao, H. Flaw insensitive fracture in nanocrystalline graphene. *Nano letters* **2012**, *12* (9), 4605–4610.

Zhang, Y.; Gao, T.; Gao, Y.; Xie, S.; Ji, Q.; Yan, K.; Peng, H.; and Liu, Z. Defect-like structures of graphene on copper foils for strain relief investigated by high-resolution scanning tunneling microscopy. *ACS nano* **2011**, *5* (5), 4014–4022.

Zhang, Y.; Tang, T.-T.; Girit, C.; Hao, Z.; Martin, M. C.; Zettl, A.; Crommie, M. F.; Shen, Y. R.; and Wang, F. Direct observation of a widely tunable bandgap in bilayer graphene. *Nature* **2009**, *459* (7248), 820–823.

Zhao, H.; Min, K.; and Aluru, N. R. Size and chirality dependent elastic properties of graphene nanoribbons under uniaxial tension. *Nano letters* **2009**, *9* (8), 3012–3015.

Zhao, S.; Zhao, Z.; Yang, Z.; Ke, L.; Kitipornchai, S.; and Yang, J. Functionally graded graphene reinforced composite structures: A review. *Engineering Structures* **2020**, *210*, 110339.

Zhao, W.; Shi, K.; and Lu, Z. Greatly enhanced ultrabroadband light absorption by monolayer graphene. *Optics letters* **2013**, *38* (21), 4342–4345.

Zhao, X.; Liu, Y.; Inoue, S.; Suzuki, T.; Jones, R.; and Ando, Y. Smallest carbon nanotube is 3 Å in diameter. *Physical review letters* **2004**, *92* (12), 125502.

Zheng, Y.; Wei, N.; Fan, Z.; Xu, L.; and Huang, Z. Mechanical properties of grafold: a demonstration of strengthened graphene. *Nanotechnology* **2011**, *22* (40), 405701.

Zhu, S. and Li, T. Hydrogenation-assisted graphene origami and its application in programmable molecular mass uptake, storage, and release. *ACS nano* **2014**, *8* (3), 2864–2872.

Zhu, W.; Low, T.; Perebeinos, V.; Bol, A. A.; Zhu, Y.; Yan, H.; Tersoff, J.; and Avouris, P. Structure and electronic transport in graphene wrinkles. *Nano letters* **2012**, *12* (7), 3431–3436.